

ABSTRACT

Direct Rheological Characterization of Polymer and Polymer Composite Filament Used in Fused Filament Fabrication Additive Manufacturing

Jingdong Chen, M.S.M.E.

Mentor: Douglas E. Smith, Ph.D.

Understanding the behavior of polymer melt flows is important for predicting final part quality and improve processing performance, particularly in Fused Filament Fabrication (FFF) Additive Manufacturing (AM). There are limited resources available to the consumer for characterizing both new and existing print materials used in FFF printers. This research seeks to address this issue by constructing a low-cost ‘filament rheometer’ device capable of measuring important melt flow properties of polymers and polymer composites directly from FFF filament. In this approach, the power law index and consistency index of the Power Law generalized Newtonian fluid model are calculated from measured pressure drop and volumetric flow rate data. A Filament Flow Index (FFI) is also proposed to quickly assess extrusion characteristics for FFF filament. The applicability of the filament rheometer is demonstrated with six commercially available FFF filaments where power law model parameters compare favorably with those obtained with a commercial rotary rheometer.

Direct Rheological Characterization of Polymer and Polymer Composite Filament Used in Fused
Filament Fabrication Additive Manufacturing

by

Jingdong Chen, B.S.

A Thesis

Approved by the Department of Mechanical Engineering

Paul I. Ro, Ph.D., Chairperson

Submitted to the Graduate Faculty of
Baylor University in Partial Fulfillment of the
Requirements for the Degree
of
Master of Science in Mechanical Engineering

Approved by the Thesis Committee

Douglas E. Smith, Ph.D., Chairperson

David A. Jack, Ph.D.

Seung Kim, Ph.D.

Accepted by the Graduate School
December 2018

J. Larry Lyon, Ph.D., Dean

Copyright © 2018 by Jingdong Chen

All rights reserved

TABLE OF CONTENTS

Chapter One	1
Introduction and Motivation	1
1.1 Statement of Problem	3
1.2 Organization of Thesis	5
Chapter Two.....	7
Literature Review	7
2.1 Fused Filament Fabrication (FFF)	8
2.1.1 Additive Manufacturing (AM).....	8
2.1.2 Melt Extrusion Based AM – FFF.....	10
2.1.3 Fluid Mechanics of Polymer Melts in FFF	13
2.1.4 Pressure Drop in FFF.....	15
2.2 Fundamental Rheology of Polymeric Melt.....	18
2.2.1 Polymer Melts Viscosity.....	18
2.2.2 Generalized Newtonian Fluids (GNF).....	22
2.3 Rheometry.....	23
2.3.1 Capillary Rheometer	24
2.3.2 Rotational Rheometer	25
2.3.3 Dynamic Rheology and the Cox-Merz Rule.....	28
Chapter Three.....	33
Device Overview	33
3.1 Measuring Protocol.....	33
3.2 Experimental Setup.....	36
3.2.1 Filament Feeding Mechanism.....	38
3.2.2 Liquefier I. Cooling System.....	44
3.2.3 Liquefier II. Heating System.....	46
3.2.4 Force Transducer	50
3.2.5 Control System.....	53
3.3 Temperature Performance.....	54
3.3.1 NTC Thermistor.....	54
3.3.2 Thermocouple	64

3.3.3 Comparison of Temperature Sensors.....	66
3.4 Temperature Control.....	67
3.5 Force Signal Processing.....	72
3.5.1 Fourier Analysis – Fast Fourier Transform	72
3.5.2 Filters in Arduino.....	78
3.6 Summary.....	80
Chapter Four.....	82
Experimental Methods.....	82
4.1 Thermal Properties of the Materials	83
4.1.1 Thermal Decomposition.....	83
4.1.2 Glass Transition and Melting Temperature	87
4.2 Force Measurements.....	91
4.3 Rheological Property Measurement.....	100
4.3.1 Measurements Conducted by Filament Rheometer	100
4.3.2 Measurements Conducted by HAAKE MARS 40.....	105
Chapter Five.....	115
Math Model.....	115
5.1 Viscosity and Flow Functions in the Nozzle	115
5.1.1 Nozzle Geometry and Assumptions.....	115
5.1.2 Pressure Drop due to Shear Flow.....	117
5.2 Simple Analysis of the Melting Zone in the FFF Liquifier	125
5.3 Nonlinear Least-Squares Regression	130
5.4 Comparison of Viscosity Curves	134
Chapter Six.....	144
Conclusions and Future Work	144
6.1 Conclusions.....	144
6.2 Future Work.....	146
BIBLIOGRAPHY.....	148

LIST OF FIGURES

Figure 2-1	Illustration of a Typical FFF process [13].....	11
Figure 2-2	The geometry of the liquefier used in the FDM process [36].....	17
Figure 2-3	Simulative shear thinning behavior of polymeric melts	20
Figure 2-4	Pressure distribution in a general capillary rheometer [47]	25
Figure 2-5	Relation between rate of deformation, test methods, and processing techniques [52].....	27
Figure 2-6	Schematic of typical tool geometries for the rotational rheometer: (a) concentric cylinder, (b) parallel plate, (c) cone and plate.....	27
Figure 3-1	The measuring schematic of the device	35
Figure 3-2	Free-body diagram of the system supported by load cell	36
Figure 3-3	Conceptual Prototyping built by SOLIDWORKS	36
Figure 3-4	Actual Prototyping	38
Figure 3-5	Different types of driver gears and idler pulleys.....	39
Figure 3-6	Comparison of different extruder frames	40
Figure 3-7	Adjustment of spring tightness.....	41
Figure 3-8	Effect of spring compression on force measurement of filament extrusion .	41
Figure 3-9	The torque-speed curve of a stepper motor [66]	42
Figure 3-10	TB6600 stepper motor driver	43
Figure 3-11	Derivation of calculating time interval of each digital pulse	43
Figure 3-12	Heat creeping (red color marks the melted filament; blue color marks the solid filament). (a) Desired melt region of filament; (b) Melting region is expanded upward; (c) Melting region passes over the inlet of heat barrier which can cause clogging.	45

Figure 3-13 Comparison of thermal dissipation (taken from Annet [68]): (a) Temperature map for liquefier without out cooling fan applied; (b) Temperature map for liquefier with cooling fan attached.	45
Figure 3-14 Comparison of thickness of two heater blocks	47
Figure 3-15 Transistor working principle	47
Figure 3-16 Configuration of two sensors in heater block with equal space to nozzle screw	49
Figure 3-17 Comparison of different nozzles by examining their inside geometries.....	50
Figure 3-18 Strain-gauge-based Beam Load Cell.....	51
Figure 3-19 Configuration of the liquefier holder	52
Figure 3-20 Bending tests: (a) 100 g weight; (b) 8226 g steel plates	52
Figure 3-21 Comparison of most widely used temperature sensors [76]	54
Figure 3-22 Resistance versus Temperature for a 10K NTC thermistor [78].....	55
Figure 3-23 Voltage Divider.....	56
Figure 3-24 Derivation of the resistance calculation for a thermistor	56
Figure 3-25 Ratiometric method of measuring thermistor's resistance.....	57
Figure 3-26 Thermistor calibration.....	61
Figure 3-27 Temperature versus resistance curves of four thermistors that labeled with the same value of β	63
Figure 3-28 Performance of Steinhart-Hart equation on Arduino Uno and Arduino Due	63
Figure 3-29 Comparison of temperature calculation using Steinhart-Hart and Beta equation.....	64
Figure 3-30 Configuration of thermocouple	65
Figure 3-31 (a) MAX31855; (b) K-type thermocouple with 3mm diameter and 15mm length.....	66
Figure 3-32 Temperature feedback control loop	68

Figure 3-33 Pulse Width Modulation signal [94]	70
Figure 3-34: Typical temperature fluctuation during temperature control experiment showing values within $\pm 0.3^{\circ}\text{C}$	71
Figure 3-35 Response speeds of thermistor and thermocouple	71
Figure 3-36: Original load cell data of ABS under 210°C & 1RPM	72
Figure 3-37 (a) Original sampling rate is not a constant; (b) The sampling rate is controlled to be constant	76
Figure 3-38 Two-sided frequency spectrum of force signal (ABS at 210°C & 1RPM)...	77
Figure 3-39 One-sided frequency spectrum of the force signal (ABS at 210°C & 1 RPM)	77
Figure 3-40 Comparison of performance of Low-pass Filter, Simple Running Average filter, and Median Filter	80
Figure 4-1 TGA curves of ABS (Two-group tests with three different sample size).....	84
Figure 4-2 Percent weight versus temperature of 5mg samples at varying heating rates	85
Figure 4-3 Derivative weight with temperature of 5mg samples at varying heat rates ..	85
Figure 4-4 TGA weight-temperature curves of six materials	86
Figure 4-5 TGA Derivative weight with temperature curves of six materials	87
Figure 4-6 DSC results of the 10mg sample heated/cooled by $10^{\circ}\text{C}/\text{min}$ (ABS).....	89
Figure 4-7 Glass transition temperature – comparison experiments (second heating cycle; ABS).....	89
Figure 4-8 The second heating cycle of DSC curves of the materials generated by using heat/cool/heat method (ABS).....	90
Figure 4-9 The second heating cycle of DSC curves of the six materials	91
Figure 4-10 Comparison of the performance of ten different rollers.....	94
Figure 4-11 Load cell reading under 100g static load	95
Figure 4-12 Hotend adjustment for friction force measurement	96

Figure 4-13 Friction force measurement under 0.5RPM, 1RPM, and 2RPM	96
Figure 4-14 Three extrusion force measurements for 3DXTECH ABS.....	98
Figure 4-15 Three extrusion force measurements for 3DXTECH CFR-ABS.....	98
Figure 4-16 Three extrusion force measurements for TRIPTECH ABS	98
Figure 4-17 Three extrusion force measurements for TRIPTECH Amphora.....	99
Figure 4-18 Three extrusion force measurements for MatterHackers CFR-PLA.....	99
Figure 4-19 Three extrusion force measurements for TRIPTECH PLA	99
Figure 4-20: Filament used for density evaluation (a) Samples for density measurement, (b) Bundles of the extrudate.....	102
Figure 4-21 Comparison of velocity measurement between two different methods of flow rate measurement	103
Figure 4-22 Pressure drop versus filament feed velocity for six materials.....	104
Figure 4-23 Pressure drop changes with temperature for CFR-ABS	104
Figure 4-24 (a) HAAKE MARS 40 rotational rheometer; (b) cone-and-plate measuring geometry	106
Figure 4-25 Sample Preparation for MARS 40	106
Figure 4-26 Comparison of different experiment mode (TRIPTECH ABS at 210°C)...	107
Figure 4-27 Oscillation amplitude sweep measurements	109
Figure 4-28 Stress sweep used to find the linear viscoelastic region	109
Figure 4-29 Comparison of two frequency sweep measuring modes.....	110
Figure 4-30 Discrepancy of the viscosity curves for the same material under same experimental condition in MARS 40 (3DXTECH CFR-ABS at 210°C)....	111
Figure 4-31 Viscosity curves for six materials at lower processing temperatures	112
Figure 4-32 Viscosity curves for six materials at higher processing temperatures	112
Figure 5-1 Inside dimensions of nozzle	117

Figure 5-2	Cylindrical coordinate.....	119
Figure 5-3	Control volume (CV) of the flow.....	120
Figure 5-4	Approximation approach of flow in a conical tube.....	122
Figure 5-5	Inside dimensions of the nozzle used on Filament Rheometer measured by the 3D measurement system	127
Figure 5-6	Hot end during processing (a) Schematic of melting line moves upward during processing; (b) Observed heat creeping for PLA at 215 °C; (c) Observed heat creeping for neat ABS at 230 °C.....	127
Figure 5-7	Effects of melting zone on prediction of pressure drop	128
Figure 5-8	Changing of melting zone has negligible effect on prediction of Power Law index.....	129
Figure 5-9	Effects of melting zone on prediction of the Consistency index	129
Figure 5-10	Curve fitting for the pressure drop versus volume flow rate data set of 3DXTECH ABS at 210 °C.....	135
Figure 5-11	Viscosity as a function of strain rate using the Cox-Merz rule for 3DXTECH ABS. Comparison of data obtained from the MARS 40 and the FFF filament rheometer.	137
Figure 5-12	Viscosity as a function of strain rate using the Cox-Merz rule for TRIPTECH ABS. Comparison of data obtained from the MARS 40 and the FFF filament rheometer.	138
Figure 5-13	Viscosity as a function of strain rate using the Cox-Merz rule for TRIPTECH Amphora. Comparison of data obtained from the MARS 40 and the FFF filament rheometer	138
Figure 5-14	Viscosity as a function of strain rate using the Cox-Merz rule for TRIPTECH PLA. Comparison of data obtained from the MARS 40 and the FFF filament rheometer.	139
Figure 5-15	Viscosity as a function of strain rate using the Cox-Merz rule for 3DXTECH CFR-ABS. Comparison of data obtained from the MARS 40 and the FFF filament rheometer	139
Figure 5-16	Viscosity as a function of strain rate using the Cox-Merz rule for MatterHackers CFR- PLA. Comparison of data obtained from the MARS 40 and the FFF filament rheometer.....	140

LIST OF TABLES

Table 3-1 The cost of prototyping	37
Table 3-2 Tests of examining the influence of arm of force on load cell measurement...	53
Table 3-3 Lookup table for the four NTC thermistors used in the project	62
Table 3-4 Temperature readings from thermistor and thermocouple	67
Table 3-5 Average values of the original and filtered force signal data	80
Table 3-6 Specification of the device	81
Table 4-1 Filaments of polymer and polymer composite used in this project.....	82
Table 4-2 Thermal decomposition & Carbon fiber content.....	87
Table 4-3 Glass transition temperature & melting point	91
Table 4-4 Comparison of thermistor and thermocouple	92
Table 4-5 Feeding velocities on MakerBot Replicator	97
Table 4-6 Filament Flow Index - Extrusion force for six materials under the normal processing condition	100
Table 4-7 Parameters of Power Law GNF model curve-fitted in PolyFlow from the data by MARS 40 rotational rheometer.....	113
Table 4-8 Parameters of Carreau-Yasuda GNF model curve-fitted in PolyFlow from the data by MARS 40 rotational rheometer.	114
Table 5-1 Inside dimensions of the nozzle (see e.g., <i>Figure 5-1</i>).....	127
Table 5-2 Pressure drop and volume flow rate measurements for 3DTECH ABS at 210°C at five stepper motor speed.	136
Table 5-3 Power Law GNF Curve-fitting results using Gauss Newton least-squares approach for all six materials at two different temperatures.....	137
Table 5-4 Effects of choosing shear rate interval for Power-law model	142

Table 5-5 Comparison of the predicted power-law index (n) between the low-cost device to the MARS 40 rotational rheometer..... 143

Table 5-6 Comparison of the predicted power-law consistency index ($k \text{ Pa} \cdot \text{s}^n$) between the low-cost device to the rotational rheometer 143

ACKNOWLEDGMENTS

First of all, I would like to thank my advisor Dr. Douglas Smith for his support and encourage through my study life. I feel grateful that he always has confidence in me and the work I've done even when I doubt myself. His huge encouragement inspired me to finish up this project. I also thank Dr. David Jack for his guidance on Arduino and rheometer. Especially, I would like to thank for his encourage whenever I feel frustrated and the verse about against worry. I wish to thank Dr. Kim for generously offering his time and support.

I wish to thank Baylor University for funding me through my Master's study.

I sincerely thank the electronic technician Mr. Steve Scully for his help and guidance on building and debugging the device. This project cannot go smoothly without his help.

A special thank goes to my colleague, Zhaogui Wang, for his kind help on building the FEA model which has been a helpful supplement for analyzing the results in this project.

I would like to thank my wife for her sacrificial support when I decided to study abroad, for loving me, and for encouraging me.

Finally, I would like to thank my parents for giving me life, for raising me, and for teaching me to be grateful for every people I met and everything I experienced.

DEDICATION

*To my beloved wife
who continued love and support me throughout the work for this thesis.*

CHAPTER ONE

Introduction and Motivation

Additive Manufacturing (AM) is a new emerging set of technologies that build products by adding the material layer-by-layer from digital data. To date, several AM technologies have emerged which are used for prototyping, tooling and fixturing, and end-use products in various fields in the industry. Correspondingly, the materials that are appropriate for AM techniques continue to grow and include metals, thermoplastics, ceramics, food, and even bio-materials. From the perspective of automotive, aerospace, and energy industries, thermoplastics play an increasingly significant role due to their very favorable strength-to-weight ratio. Some major AM technologies that process thermoplastics are stereo-lithography (SLA), selective laser sintering (SLS), multi-jet fusion (MJF), and fused filament fabrication (FFF).

Fused Filament Fabrication shows the enormous potential to benefit human life in education, industry, and research, and also provides a means for making artwork and mechanical assemblies at home. Home-based, individual use of FFF is due in part to it being a cost-effective technique as compared to other AM techniques which process thermoplastics utilizing the costly layer technique (e.g., SLA, SLS, and MJF). FFF is also supported by a large open source community. FFF is an AM technique where filament material is fed into a heated liquefier where it is melted and then is extruded to build the object layer-by-layer. Though FFF has been widely used in industry and research, various

issues limit its application as a technique that can mass produce products that require high mechanical properties.

Many studies have been conducted to improve the performance of FFF products by optimizing the process and incorporating high-performance materials. Process optimization studies have included the determination of the appropriate die geometry, processing temperature, layer thickness, and tool path. One approach to achieve higher mechanical properties is by adding fillers in the materials such as short-rigid fibers and long-flexible fibers mixed with neat polymeric materials are of extreme interest. This has led to various studies on the effects of orientation, aspect ratio, and concentration of fibers on the mechanical properties of printed parts.

The processing of polymeric materials in FFF are carried out in a molten state. Gaining a thorough understanding of polymer and polymer composite melt behavior in FFF will lay a solid foundation for improving the FFF AM technique. The flow of polymer melts in FFF is described as the pressure-driven flow. However, measuring the pressure of the flow in the FFF nozzle has practical difficulties, because the nozzle is small, making impractical to attach a pressure gauge inside. Therefore, indirect pressure measurement methods offer promise and will be investigated in this thesis for this purpose.

Rheological properties of polymer melts, such as the shear-thinning and viscoelasticity govern the flow behavior during processing. Therefore, the rheology of FFF polymers and polymer composites is of crucial importance when considering the design of the processing device and the operating conditions. Furthermore, the rheological data is helpful for people to characterize polymers and predict their molecular

structure further. However, lab scale rheometers are expensive, particular for those who simply want to characterize a filament or measure the fundamental rheological properties (e.g., the shear rate dependent viscosity) of a polymer being considered for FFF. Currently, there is no method or apparatus available to directly characterize the rheological properties of polymer and/or polymer composite filaments used in the FFF process. Therefore, a method will be developed to characterize the filament and assess the corresponding fundamental rheology using the FFF-based device directly in this thesis.

1.1 Statement of Problem

The primary goal of this thesis is to obtain relevant rheological properties for polymer and polymer composite FFF filament directly using a low-cost benchtop device. This device, denoted here as a ‘filament rheometer,’ is developed with the capability of measuring the force (or pressure drop) required to extrude the molten filament through the nozzle in FFF. The secondary objective is to use the measured pressure drop to evaluate specific rheological properties (i.e., shear rate dependent viscosity) of the polymer and/or polymer composite specifically used in FFF directly from the filament feedstock. The materials used in this thesis are all selected from commercially available, commonly used materials for desktop FFF-based 3D printers, and are given in *Table 4-1* with the corresponding manufacturer and specifications.

The main components on an FFF-based machine are used for building the new device. The stepper motor, rollers, and the spring on the FFF extruder are all improved to provide a smooth movement of the filament feeding. To verify our assumption that the processing is in isothermal condition, two thermistors are carefully calibrated and located

at different locations near the nozzle for monitoring the real-time processing temperature. A beam-type force transducer is added between the extruder and the liquefier. By changing the speed of the stepper motor and the processing temperature, a set of force data is obtained for each material. Assuming there is no slippage between the polymer melts and the wall of the inside nozzle, the measured force can be converted to pressure drop through the nozzle by simply multiplying the area of the nozzle entrance.

A mathematical model is developed using the conservation of momentum and a generalized Newtonian fluid power-law model for the three regions (upper cylinder, conical die, and the capillary die) in the nozzle separately. The total pressure drop is equal to the summation of the pressure drop in each section. The model assumes that pressure loss is due to the shear of the polymer melt flow, and the extensional stress is ignored. The interior nozzle geometry parameters are measured using a 3D scanner from cross-sections of commercially available nozzles used in our flow studies. Once pressure drop and volume flow rate are measured using our constructed low-cost device, two unknowns power-law parameters are computed using a custom curve-fitting in MATLAB (MathWorks, Inc., Natick, MA) developed here for this purpose.

In addition to the experiments conducted using the low-cost device, a large number of oscillatory tests are performed in a lab-scale traditional rotational rheometer. Three properties are measured in the rotational rheometer which includes the complex viscosity, storage modulus, and loss modulus. The Cox-Merz rule is applied in this study to convert the complex viscosity versus angular frequency to shear viscosity versus shear rate. Then the complex viscosity that falls into the power-law region is used to verify the accuracy of the predicted filament rheometer power-law parameters. A discussion on the

performance of the pressure drop math model without considering the extensional stress is also included with regards to the curves of storage and loss modulus.

1.2 Organization of Thesis

To present the current work efficiently, this thesis is divided into six chapters. Overall, the body of the thesis consists of three main sections, the literature review, the detailed introduction of current work, and the conclusions.

Chapter Two reviews the literature relevant to the study. Firstly, the background and the development of fused filament fabrication is covered. The current status of FFF among a variety of the additive manufacturing techniques and the research studies required to improve FFF such as the measurement and prediction of the pressure drop through a nozzle is included. Secondly, the necessary information of polymer melt rheology used to analyze the flow behavior and build the analytical math model for predicting pressure drop in this thesis is studied. In the end, the current studies of the theories of rheometers, especially the applicability of Cox-Merz rule, are explored.

Chapter Three to Chapter Five covers each stage of the current work. In Chapter Three, the conceptual and final design of the low-cost filament rheometer device is introduced which includes the components selection, the efforts made for minimizing the measurement error, and the force signal processing. Chapter Four presents the experimental methods performed with the low-cost filament rheometer device and the commercial laboratory rheometers. Chapter Five presents the analytical model of pressure drop and the nonlinear Least-squares curve-fitting method used to estimate rheology model parameters from the measured data. The discussion of the comparison of shear rate dependent viscosity using the filament rheometer and the commercial lab-scale

rheometer as well as the discrepancies in computed pressure drop are presented with central importance in this chapter.

Chapter Six concludes the current study and provides a list of potential studies with of the low-cost filament rheometer device in the future.

CHAPTER TWO

Literature Review

Fused Filament Fabrication (FFF) continues to receive attention in the research literature in areas from process simulation to the rheology analysis of material due to its unique mechanism for processing polymers. Since the flow of a polymer melt is a pressure-driven flow in FFF, the experimental and computational determination of pressure drop is of central importance to the exploration of the flow behavior of polymer melts. Literature that focuses on modeling the pressure drop in the FFF process will be reviewed in this section. In addition to an appropriate math model, the data from a commercial lab-scale rheometer are required to assess the functionality and validation of the measured pressure drop using the low-cost device. Commonly used research grade rheometers, specifically the rotational cone and plate rheometer, will be discussed with a special focus on how to utilize the dynamic rheological measurement by a rotational rheometer (the rheometer which is accessible for the study in this thesis) to analyze the pressure drop and rheological properties of polymers in FFF. The Cox-Merz rule, an empirical rule to convert the oscillatory dynamic data to the data measured under quasi-steady-state conditions, has seen wide application for polymers commonly used in industry and research. Its applicability to the materials used in this thesis is carefully reviewed through the evaluation of prior research.

2.1 Fused Filament Fabrication (FFF)

Fused Filament Fabrication (FFF) has become one of the most widely used additive manufacturing techniques for polymeric materials with application in industrial and educational design prototyping [1,2]. Understanding how polymer melt flow behaves is of primary importance to FFF for improving the die and process design and for realizing the successful build of FFF products. Starting with the background of additive manufacturing, this section will introduce the fundamental of FFF process and the flow properties of polymer melts in this technique, especially the pressure drop over the nozzle.

2.1.1 Additive Manufacturing (AM)

Manufacturing converts raw materials into the functional products resulting in changing in either their physical or chemical properties. Up to now, manufacturing processes are developing and expanding continuously and are broadly divided into the conventional and unconventional methods. Additive Manufacturing (AM) methods, often considered to be among the unconventional manufacturing techniques, was first presented in the 1980s by Charles W. Hull [3,4]. Additive manufacturing, also known as three-dimensional (3D) printing, rapid prototyping, solid freedom fabrication, or layered based manufacturing is a process to fabricate objects by adding layers of new material as defined by digital data.

The design and build process for AM typically consists of four steps: Firstly, objects are modeled with a Computer-Aided Design (CAD) software or obtained by scanning. Secondly, the solid model of the part to be manufactured is converted into a StereoLithography (STL) file. Data in the STL file approximates the curved surfaces of

the model with finite polygons. The model is analyzed and “sliced” into cross sections (layers) by a software program specifically designed to deliver data for 3D printing. The sliced data is defined specifically for deposition of feedstock (liquids or powders) with even thickness of layers that will form the detailed geometry of the part. Finally, the digital data is submitted to an AM machine and manufactured to be the desired product.

The substantial increase in AM industries can be seen in both the development of the techniques and the marketplace. The number of AM techniques have grown to now have a group of more than twenty techniques [5]. According to ASTM F2792-12a, these techniques were classified into seven groups: (1) binder jetting, (2) directed energy deposition, (3) material extrusion, (4) material jetting, (5) powder bed fusion, (6) sheet lamination, and (7) vat photo-polymerization [6]. Representative AM technologies among the seven categories include Indirect inkjet printing, Electronic Beam Welding (EBM), Fused Filament Fabrication (FFF), Inkjet Printing, Selective Laser Melting (SLM), Laminated Object Manufacturing (LOM), and Stereolithography (SLA), respectively [6]. Though ASTM F2792-12a was withdrawn in 2015, it is still the common criteria for classifying the ever-increasing AM techniques. According to the 2014 report by Wohlers, the AM industry had gained \$3.07 billion in worldwide revenues in 2013 which grew by 33% over the previous year [7]. The market size of the industry is expected to increase to more than \$20 billion in 2020 [6,7].

The fact that the AM industry continues to experience rapid growth is due in part to its numerous benefits over the traditional ‘subtractive’ manufacturing. AM provides a more efficient option for producing products with high complexity in geometries. It is often said that ‘AM provides added complexity at no cost.’ It gains the potential to reduce

the overall time from concept design to prototyping, and finally to quantity production. Furthermore, building products layer by layer contributes to significant energy and material savings. More information about the advantages can be referenced as cited in [8,9,10].

2.1.2 Melt Extrusion Based AM – FFF

Fused filament fabrication, also known as Fused Deposition Modeling (FDM[®]) or Melt Extrusion Manufacturing (MEM) [1], is an extrusion-based deposition AM process. As its name indicates, FFF fabricates products by melting and extruding a filament of material which is typically a polymer or in some rare circumstances a polymer composite. In the FFF process, as shown in *Figure 2-1*, the polymer or polymer composite filament feedstock is supplied continuously into a heated liquefier where the filament is melted and extruded onto the platform below. The gantry system moves the extruder, or in some designs, the build surface to build the product layer-by-layer. The Big Area Additive Manufacturing (BAAM) [11] is similar in concept to FFF, even though feedstock is polymer pellets rather than filament. As such, BAAM machines employ a screw-type extruder to melt and deliver the polymeric material to the deposition platform. To avoid confusion, FFF, from the context of this thesis, is restricted to the application small-scale (or desktop scale) filament-based machines.

A typical FFF 3D printer consists of the material delivery system, heating block and nozzle, and the gantry system. A pinch roller is the most common material feed system in FFF, where the filament is compressed and pushed into the heated nozzle. The liquefier melts the filament and consists of the heater and nozzle. The heater is often equipped with temperature sensors to provide feedback for sufficient and stable heat flux

to melt the continuously delivered filament. The geometry of the nozzle determines not only the pressure drop during filament extrusion but also the resolution of the printed bead. The build surface upon which the extruded material solidifies is the critical component determining the quality of products. As Wang, et al. [12] summarized, carefully defining roughness, levelness, and the temperature of the build surface can avoid the warping of the edge of the final product.

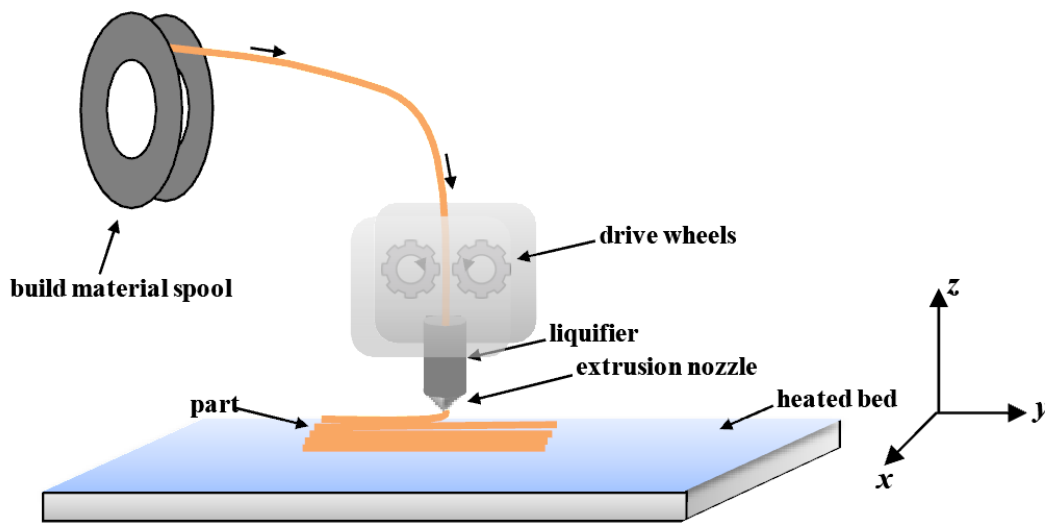


Figure 2-1 Illustration of a Typical FFF process [13]

The molten nature of the feedstock in the nozzle and the shear thinning behavior in extruded material make most of the polymers ideal feedstock for FFF. The most commonly used polymers in FFF are poly-lactic acid (PLA) and acrylonitrile butadiene styrene (ABS). PLA enjoys widespread application for prototyping in education and research. It is a low-cost linear polymer, being biodegradable and having a relatively low melting temperature. However, its brittleness and low glass transition temperature limit its application in the industry [14]. Compared to PLA, ABS has a higher flexural strength and elongation to failure which often makes it a better candidate material for the end-use

commercial applications. Engineering polymers such as linear polycarbonate (PC), acrylic, and nylon each have higher strength and high-temperature resistance can also be processed with FFF to increase the performance of the final products. In addition, polymers like Polyether Ether Ketone (PEEK) or polymer imide (PEI), which have the exceptionally high strength and stiffness, have been used in the aerospace and automotive industries. With the increase of stiffness and glass transition of those high-performance polymers, there is often an increase in cost and a substantial increase in the processing temperature [15,16,17].

Due to the limitation of the mechanical properties of low-performance pure polymers (i.e., PLA, ABS) and the higher cost for processing high-performance polymers (PEEK), adding short fibers such as carbon fibers into the polymer matrix has been investigated as an alternative method to improve the mechanical properties (tensile strength and Yong's modulus) of final products (see e.g., [18,19]). The work conducted by Duty, et al. [20] compared the stiffness and strength of the samples printed by the BAAM system at Oak Ridge National Lab (Oak Ridge, TN) in an injection molded tensile bar. Their results demonstrate the strength and stiffness of the printed beads highly depend on the deposition direction and will be increased with the fibers aligned with the deposition direction. Brenken, et al. [21] gave a thorough review of the published studies on analyzing the mechanical properties of printed parts in Fused Filament Fabrication with fiber-reinforced polymer composites. They summarized the tensile mechanical properties along the beads printed direction for both discontinuous and continuous fiber-filled materials. For the discontinuous fiber system, the mechanical properties are improved in the fiber alignment direction. For the continuous fiber reinforced materials,

the strength along bead direction can get as high as the aircraft-grade aluminum. Another study conducted by Hao, et al. also demonstrate the polymer composites with continuous carbon fibers provides higher mechanical properties comparing to the short carbon fiber filled polymer [22].

2.1.3 Fluid Mechanics of Polymer Melts in FFF

Though some polymers or polymer composites, such as ABS, CFR-ABS, do not have a specific melting point, these polymers are considered as fluid or semi-fluid in FFF processing [23]. As in other fluid flow systems, polymer melt flow in FFF is governed by the conservation of energy, conservation of mass, and conservation of momentum. A detailed explanation and derivation of these equation, in the book written by Brid, et al. [23], which introduces fluid mechanics from the perspective of those in the polymer fluid. Some assumptions and boundary conditions on the flow of polymer melts in a commercial 3D desktop printer nozzle appear in Chapter Five simplify the application of these equations.

Polymer melts are assumed to be incompressible, by which the density is considered constant in time and space and is independent of pressure and temperature. The constant density simplifies the calculation of the velocity profile and flow rate significantly. The accuracy of this assumption can be referred to the books by Dechant and Krevelen [24,25]. An approximate error of the pressure due to the incompressible flow assumption during profile extrusion processing for most polymers is given about 0.3% in [26]. It is safe to assume that polymer melts are incompressible in FFF due to the relatively low processing pressure as compared to the flow in injection modeling.

When applying conservation equations to the FFF process, a no-slip wall condition is commonly applied at the nozzle walls. The no-slip wall assumption states the velocity of polymer melts at the wall of nozzle is equal to zero, such that a velocity profile is developed with the maximum velocity at the center and zero velocity at the wall. However, the no-slip boundary condition has been shown that it does not apply to some polymer melts (e.g., linear low-density polyethylene (LLDPE) [27] and high-density polyethylene (HDPE) [28]) at high-stress level (screw-based extrusion). Navier (1823) proposed a wall slip condition (also known as Navier-slip boundary condition) [29] as being critical for capturing extrusion instabilities, like sharkskin and melt fracture. Though Agarwala, et al. [30] applied Navier-slip boundary condition on filament slippage and bead shrinking, respectively, the slippage of polymer flow in the nozzle for FFF has yet to be considered. Therefore, in this project, the FFF nozzle flow is assumed to have no slippage of polymer melts at the wall of the nozzle.

Simple shear flow and extensional flow are the two standard flows used to characterize a polymer melt flow in processing. In the study conducted by Cogswell [31], the deformation of polymer melt in a geometrically complex die (i.e., a nozzle consisting of a cylindrical and a conical zone) is assumed to be the superposition of simple shear with that of an extension flow.

Simple steady shear flow, also known as the pure-shear flow, considers the flow to be divided into infinite parallel laminar flows (streamlines are parallel) that slide with respect to each other such that the velocity varies in only one direction. For example, laminar simple shear flow in cylindrical coordinates may be written as

$$v_z = \dot{\gamma}r; \quad v_r = 0; \quad v_\theta = 0 \quad (2.1)$$

where v_z , v_r , and v_θ is the axial, radial, and azimuthal velocity, respectively.

Extensional flow is classified into three categories, uniaxial extensional flow, biaxial extensional flow, and planar extensional flow [25]. In FFF, the polymer melts flow through a conical die yielding a stretching in the axial direction due to flow acceleration. Normal stresses acting in the axial direction stretch the polymer melt, and the related flow is uniaxial extensional flow. The elongation (or extensional) viscosity is a material property used to represent the resistance of material to elongational deformation defined as

$$\eta_E = \frac{\sigma_{zz} - \sigma_{rr}}{\dot{\epsilon}} \quad (2.2)$$

where σ_{zz} and σ_{rr} are the normal stresses in cylindrical coordinate.

2.1.4 Pressure Drop in FFF

In typical FFF processing, the solid part of the filament acts as a piston with a constant force to push the molten filament flow through the liquefier. Hence, the pressure, especially the pressure loss, in such a pressure-driven flow is of extreme importance for describing and understanding the flow behavior. The pressure drop of a polymer melt through a round tube, or capillary die, is commonly measured experimentally using capillary rheometer. In this case, the pressure drop is measured in an instrument under carefully defined conditions such as a well-defined ratio of the length to diameter of the capillary die. It is often assumed that the flow in a sufficient long capillary die is fully developed. In reality, the die used in a FFF system is more complex than that of a simple capillary rheometer. Efforts have been made to predict the pressure drop in an FFF nozzle which includes a conical-cylindrical region that can exhibit a significant increase in shear rate [32].

Cogswell [31] developed an analytical model for predicting the pressure drop of converging flow in an extrusion die. He suggested the total pressure loss over the entire die is the summation of the pressure drop due to simple shear, simple extension, and an abrupt entrance effect from the conical reservoir into the capillary die. Boles [33] derived an expression for pressure drop of the converging flow in a conical die by solving the radial momentum equation in a spherical coordinate in conjunction with power-law model. The pressure drop of entrance flow was given by an empirically derived equation based on the experiments on oil and polyisobutylene. Kwon, et al. [34] derived an alternative formula for pressure drop in a converging die and evaluated the applicability of such a formula by conducting experiments for polystyrene (PS) and polypropylene (PP). They obtained a pressure drop equation by solving a θ -averaged force balance equation (see equation (A-9) in [34]) using power-law fluid model. More recently, a study conducted by Phan, et al. [35] derived a hybrid model by modifying the Cogswell model for predicting ΔP_E using Bole's model for calculating the entrance pressure drop. In addition to applying the power-law model to the simple shear flow, they assume the rate of elongation and the extension viscosity also obey the power-law relation. Rather than using a piecewise model of flow through infinitely thin cylinders, they use a generalized Bernoulli equation to solve the pressure loss function which contains the shear and elongation terms

Notice that all the expressions for pressure drop given above consider effects of extensional stress on the pressure drop. However, the performance of these models has not been tested experimentally in any FFF-based technique. Not all models for predicting pressure drop include extensional effects as mentioned above. For example, studies

conducted by Bellini [36] that assumed the flow in the FFF nozzle is simple shear flow and ignoring the entrance effect. He suggested the total pressure drop in the nozzle is divided into three parts corresponding to the nozzle geometry, as shown in *Figure 2-2*. In conjunction with the Arrhenius relation, the pressure drop model is given in *Equation 2.3* – 2.5.

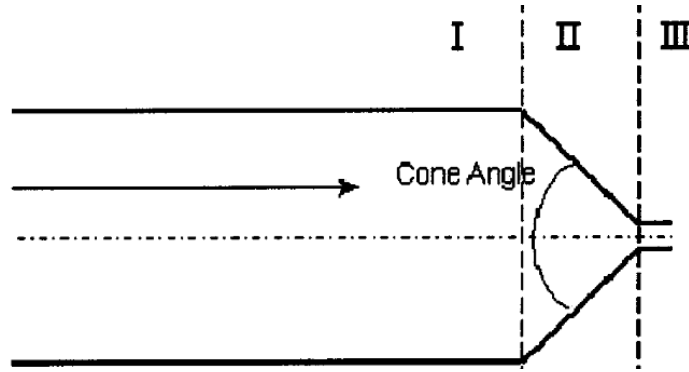


Figure 2-2 The geometry of the liquefier used in the FDM process [36]

$$\Delta P_I = 2L_1 \left(\frac{v}{\phi} \right)^{\frac{1}{m}} \left(\frac{m+3}{R_1^{m+1}} \right)^{\frac{1}{m}} \cdot e^{[\alpha(\frac{1}{T} - \frac{1}{T_\alpha})]} \quad (2.3)$$

$$\Delta P_{II} = \frac{2m}{3} \cot \frac{\beta}{2} \left(\frac{vR_1^2(m+3)}{\phi} \right)^{\frac{1}{m}} (R_2^{-\frac{3}{m}} - R_1^{-\frac{3}{m}}) \cdot e^{[\alpha(\frac{1}{T} - \frac{1}{T_\alpha})]} \quad (2.4)$$

$$\Delta P_{III} = 2L_3 \left(\frac{vR_1^2(m+3)}{\phi R_2^{m+3}} \right)^{\frac{1}{m}} \cdot e^{[\alpha(\frac{1}{T} - \frac{1}{T_\alpha})]} \quad (2.5)$$

In the above ΔP_I , ΔP_{II} , and ΔP_{III} are the pressure drop through the corresponding region in *Figure 2-2*, L_1 and R_1 are the length and radius of the liquefier (section I in *Figure 2-2*), L_2 and R_2 are length and radius of the capillary die (section III in *Figure 2-2*), β is the angle of the conical cylinder. The m and ϕ are material constant.

$$m = 1/n \quad (2.6)$$

$$\phi = k^{(-1/n)} \quad (2.7)$$

where n is the Power Law index, k is the consistency index. The velocity (v) is the average velocity of the polymer flow at the nozzle entrance. This model has been used in many studies on FFF such as the work conducted by Ramanath, et al. [37], Sukindar, et al. [38], Pandey, et al. [39], and Tlegenov, et al. [40].

To conclude, the ability of pressure drop models that include extensional flow effects to accurately predict the pressure drop in a conical die is still undermined and questioned. To simplify the model approach, the entrance flow and extensional flow effect are ignored in this study.

2.2 Fundamental Rheology of Polymeric Melt

Rheology is the study of deformation and flow. The polymers involve a large amount of deformation and flow when they are processed in molten state. Rheology plays a significant role for characterizing and simulating the non-Newtonian and viscoelastic nature of polymer melts in experimental and computational fields. In addition to characterization, the rheological properties of polymer are critical considering the design of processing, processing equipment, and selection of operating conditions [41]. Computational rheology develops the constitutive equations (models) to simulate and predict the measured rheological properties such as the generalized Newtonian fluids model, which will be introduced in this section.

2.2.1 Polymer Melts Viscosity

Viscosity is defined as the ratio of shear stress to shear rate. When the melt flows in an extrusion die, it is subjected to the shear deformation. Assuming the flow is in a

steady state, the shear force between two layers of the melts is proportional to the shear rate in the simplest case of a Newtonian fluid. And the constant coefficient of this proportion is called the dynamic shear viscosity. Though the polymer melts can exhibit the Newtonian fluids' behavior only in deformations that are sufficiently small and slow, the nonlinear viscosity is an important property of polymers under most of the processing techniques. Non-Newtonian fluid does not obey Newton's law of viscosity which means the viscosity has a nonlinear relationship to the shear rate. Viscosity is a property to distinguish the Newtonian and non-Newtonian fluids then.

The viscosity of polymeric fluids depends on shear rate, temperature, molecular weight, molecular weight distribution, and pressure [42]. Therefore, in the context of polymer or polymer composite melts, viscosity gains the most significance. Controlling the viscosity during processing is directly related to the energy required to extrude the melt. The shear rate dependence of viscosity of polymer melts brings it to be a critical factor in the design of extrusion dies and control of processing performance. Therefore, viscosity, as the most critical property of polymer rheology, is of central importance in FFF.

The phenomena of shear rate dependent polymer melts can be observed visually. One of the prominent characteristics of the polymeric melts is their shear thinning (pseudo-plastic) behavior. If the viscosity decreases with increasing shear rate in, it is said to be pseudo-plastic. The shear thinning phenomenon of polymer melts is due to disentanglement and alignment of polymer molecular chains during flow. The molecular chains of polymer are randomly oriented, and the long chains are always entangled when at rest. They start to align and disentangle when sheared, such that the viscosity is

decreasing. It needs to be emphasized that if the shear rate is sufficiently high, for a small group of polymers with sufficient short molecular chains will behave like a Newtonian liquid again, which is the same as when it under very low shear rate. The reasons leading to the same behavior are not the same. The viscosity of polymer melts at low shear rate does not change as the low shear stress to disentangle the long chains. Conversely, the long chains get fully aligned and disentangled at very high shear rate, such that the viscosity keeps unchanged again. The full shear thinning curve is shown in *Figure 2-3*, where η_0 is called zero shear viscosity and η_∞ is the infinite viscosity. Since the extremely high shear rate is difficult to reach in reality and might cause the polymer chains to break, the second Newtonian plateau is rarely observed. It should to be notated that that the zero shear viscosity is of proportional molecular weight dependence.

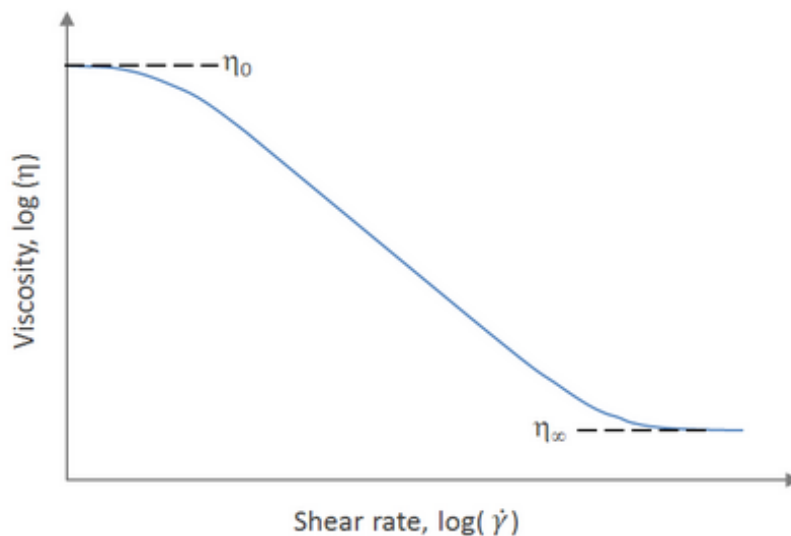


Figure 2-3 Simulative shear thinning behavior of polymeric melts

Another non-Newtonian phenomenon, shear thickening (dilatant), is rarely observed for polymer or polymer composite melts, that is, most polymer melts exhibit shear thinning. This distinct behavior is of extraordinary practical importance in the

processing and fabrication industry as the melts can smoothly flow through the dies or other process equipment under high shear rates. Some typical examples of the shear thickening (also known as dilatant) fluids are the polymeric binders for paints, blood, and clay [43].

In addition to shear rate dependence, the viscosity is expressed as a function of temperature as shown in the following equation [36].

$$\eta(T, \dot{\gamma}) = H(T)\eta(\dot{\gamma}) \quad (2.8)$$

In the above, $H(T)$ represents the temperature dependence. For polymers processed well above the glass transition (T_g), the Arrhenius law [44] is valid to determine temperature dependence as

$$H(T) = \exp\left[\frac{E_0}{R} \left(\frac{1}{T} - \frac{1}{T_0}\right)\right] \quad (2.9)$$

where T_0 is the reference temperature where the viscosity is known, T is the temperature of interest (usually is the processing temperature in research or industry), E_0 is the activation energy, and R is the gas constant.

Though in this thesis the assumption has been made the polymer melts are incompressible during processing, it is necessary to give a fundamental review of how pressure affects the viscosity here. Contrary to the temperature, increasing pressure usually causes increasing viscosity [45]. This is because of the increasing compression on the flow decreases the free volume and increase the shear stress. The Barus equation is used to describe the pressure dependence of viscosity [45],.

$$\ln(a_p(P)) = \beta(P - P_0) \quad (2.10)$$

where β is the pressure constant, $a_p (= \eta(P)/\eta(P_0))$ is the shift factor, and $\eta(P_0)$ is the viscosity at reference pressure P_0 .

2.2.2 Generalized Newtonian Fluids (GNF)

The Generalized Newtonian Fluids viscosity models are valid to predict the shear rate dependent viscosity. GNF models are only valid for predicting the behavior of simple steady shear flow, in other words, the normal stress is not described in this context. To date, a great variety of GNF models (are reviewed in [25] and [36]) have been proposed for predicting the observed shear thinning behavior, in particular, the shape of the viscosity curve. One of the most widely used is the Power Law model (also known as Ostwald-de Waele model)

$$\eta(\dot{\gamma}) = k\dot{\gamma}^{n-1} \quad (2.11)$$

where k is called consistency index, and n is the power-law index. Notice $n - 1$ represents the slope of viscosity curve in logarithm space, and $\log k$ is the intercept on the $\log \eta$ axis. For most of the polymer melts exhibiting shear thinning behavior n varies from 0 to 1. Power Law model has been widely used in polymer processing or even in rheometry in which the shear rate is high. The prediction of power-law has highly agreement to the high shear rate region, while it cannot describe the low-shear-rate viscosity (i.e., Newtonian plateau in viscosity curve), as shown in *Figure 2-3*.

A more complicated model, the Carreau-Yasuda model, with five parameters which can provide a better fit for materials under low shear rate.

$$\eta(\dot{\gamma}) = \eta_{\infty} + (\eta_0 - \eta_{\infty})[1 + (\dot{\gamma}\lambda)^a]^{\frac{n-1}{a}} \quad (2.12)$$

where a is an exponent factor, λ is a time constant, and n is the power-law index. The exponential index a determines the shape of the transition region where the transition from Newtonian plateau to the power-law region. Increasing a leads to the sharper

transition. The time constant λ determines when the transition occurs. Assuming η_∞ is equal to zero, *Equation 2.12* is simplified to be

$$\eta(\dot{\gamma}) = \eta_0 [1 + (\dot{\gamma}\lambda)^a]^{\frac{n-1}{a}} \quad (2.13)$$

In the above, the shear rate cannot analytically be expressed as the velocity profile or even the pressure drop since the equation is polynomial. Therefore, it is difficult to apply this the Carreau-Yasuda mode analytically to build a math model that can predict the shear rate versus pressure drop.

2.3 Rheometry

Rheometry refers to the experimental technique used to determine the rheological properties of materials, the instrument for this purpose is called the rheometer. A great variety of rheometers have been used to measure the rheological properties of polymers when polymer melts under shear deformation. These devices are capable of measuring viscosity, the first and second normal stress differences, the storage modulus (G') and loss modulus (G''). The choice of rheometers depends on the phenomenon and the processing technique of interest. Moreover, the achievable shear rate of the instrument is the critical factor for choosing rheometers. Proper characterization of rheological properties must be carried out at a shear rate that is relevant to the specific processing techniques. The laboratory rheometers can be broadly classified into two categories, rotational rheometers and capillary rheometers. More focus will be putted onto the rotational rheometers and the corresponding dynamic rheology in this section.

2.3.1 Capillary Rheometer

Capillary rheometers are efficient in measuring the rheological properties of materials at high shear stress, that is the achievable shear rate is up to 10^7 s^{-1} [46]. Generally, in a capillary rheometer, a plunger or a ram impose the pressure on the molten polymer drives it flow through the cylinder reservoir at a constant speed or a constant shear rate while passing the material through a capillary die. The net resulting pressure in the capillary is measured and modified between two points (l) in the capillary die, as shown in *Figure 2-4*. Then the shear stress at the wall (τ_w) can be calculated as

$$\tau_w = \frac{R\Delta P}{2l} \quad (2.14)$$

The apparent shear rate along the wall ($\dot{\gamma}_w$) is calculated as

$$\dot{\gamma}_w = -\frac{4Q}{\pi R^3}; \quad (Q = \pi R^2 v) \quad (2.15)$$

where R is the radius of reservoir, v is the constant velocity of plunger. The apparent shear viscosity is given as

$$\eta = \frac{\tau_w}{\dot{\gamma}_w} \quad (2.16)$$

In a general test, by cycling through several different ram speeds at controlled temperature one can explore how the viscosity changes with the varying shear rate or the shear stress. By controlling the temperature, capillary rheometers can measure materials' viscosity as a function of temperature and pressure. Generally, the result of the measurement is a viscosity curve as shown in *Figure 2-3*.

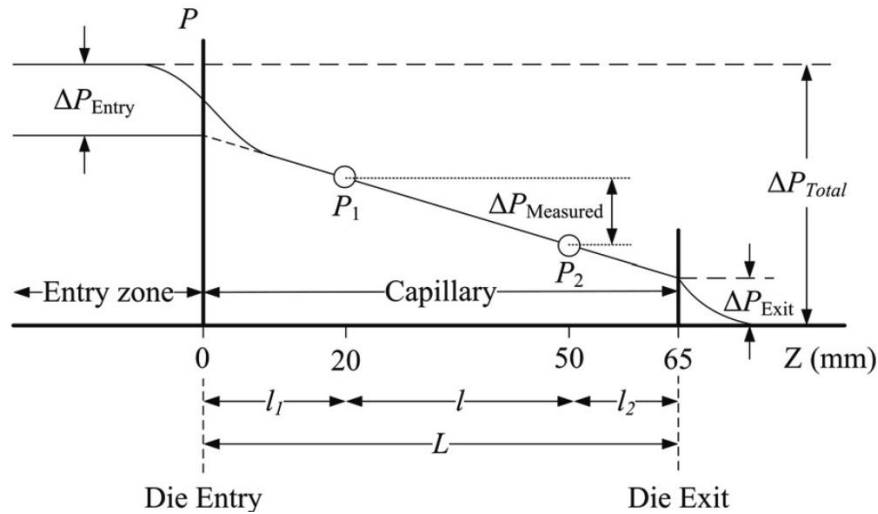


Figure 2-4 Pressure distribution in a general capillary rheometer [47]

The above-mentioned capillary rheometers are most commonly used in industry and research, and they are called the single-bore model. Another more advanced alternative is called twin bore capillary rheometer (e.g., RH2200 model by Malvern Panalytical (Malvern, Worcestershire, U.K.) [48]). The two dies have the same diameter but different length, thus two different shear stress values are generated at the same shear rate. By comparing the stress value, the twin-bore rheometers can automatically correct the pressure according to the Bagley correction [49] or the Cogswell correction [31].

2.3.2 Rotational Rheometer

The rotational rheometer is typically used for shear rates between 10^{-3} to 10^3 s^{-1} [50], as shown in *Figure 2-5*. In a rotational rheometer samples are loaded between two geometries and subjected to shear stress generated by the torque on one of the two surfaces, then the shear stress, the resulting defamtion, and shear rate are calculated from the measured torque, deflection angle, and the angular velocity of the rotation at different temperature. The movement of the geometries can rotate in one direction or

rotate back and forth corresponding to the rotational tests and oscillatory tests.

Comparing to the capillary rheometers, rotational rheometers (also known as torsion rheometers) are more appropriate for lower shear rate measurements. Rotational rheometer not only has the capability to perform some fundamental rheological tests but also allow for a comprehensive investigation of the viscoelastic properties by performing a wide variety of tests, such as stress, creep, relaxation, oscillation [51,52], this can be accomplished by conducting the tests in the oscillatory shear mode which can also be utilized to identify the linear viscoelastic region (LVER) [53], the consequential benefit of performing the tests in LVER is that the internal microstructure of a sample is not destroyed. Experiments performed in steady-rotation mode also allow for measuring the viscosity of some polymer solutions. However, the edge failures (breakage of the sample between the tool geometry and the plate) mostly resulted from the relatively high elasticity of polymers usually causes erroneous measurement results, as shown in *Figure 4-25*.

The functionality of rotational rheometers depends on the relative rotation tool geometries, and the typical geometries are concentric cylinders, parallel plate, and cone-and-plate (*Figure 2-6 (c)*). The cone-and-plate geometry is of interest in this work. It is used primarily for oscillatory tests. The key advantage of cone-and-plate viscometers is the near uniform shear rate for the entire material sample. In the oscillatory mode, the samples are stimulated continuously by either deformation or shear stress sinusoidally, the response of the sample will also show a sinusoidal shape. This range is the LVER mentioned above. Usually, the LVER can be determined under the oscillatory amplitude (controlled deformation or stress) sweep [51,54].

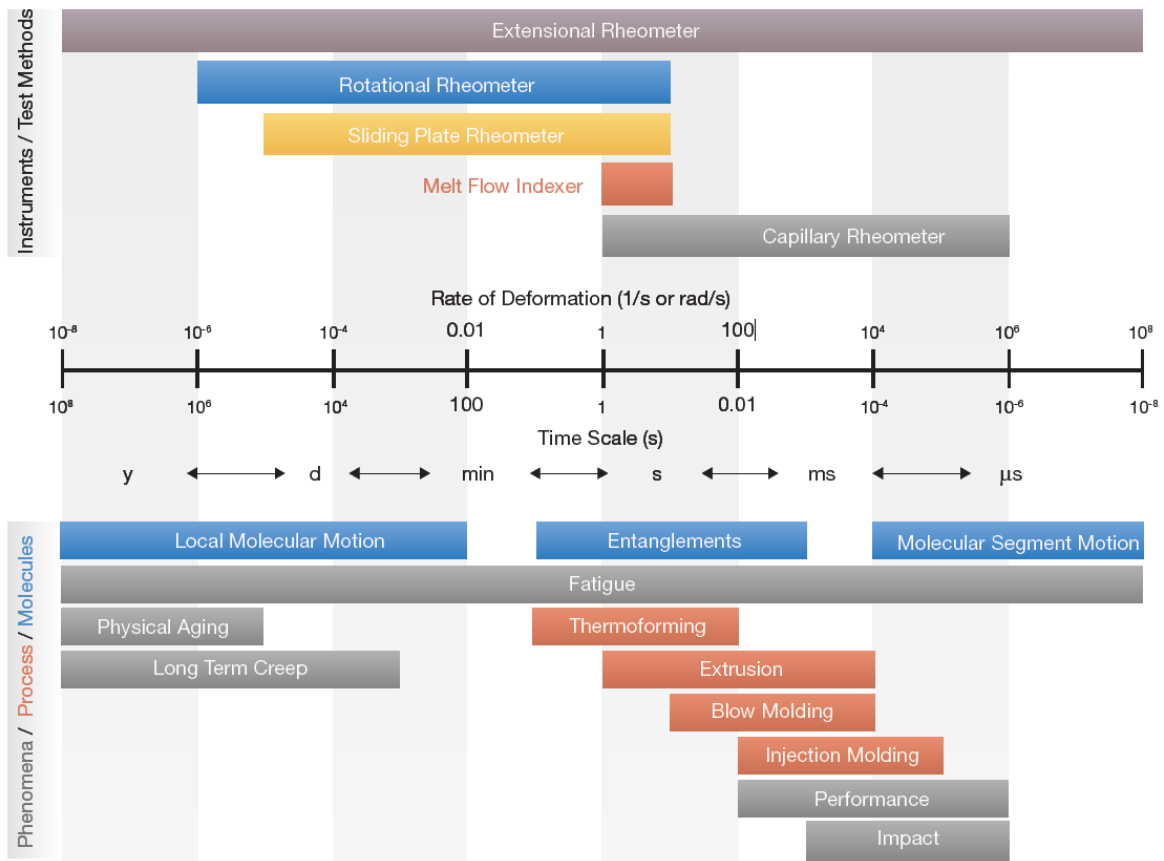


Figure 2-5 Relation between rate of deformation, test methods, and processing techniques [52]

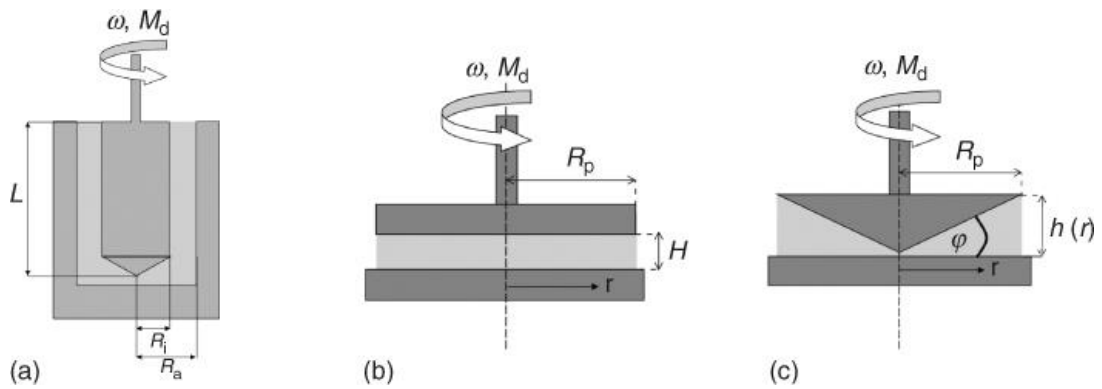


Figure 2-6 Schematic of typical tool geometries for the rotational rheometer: (a) concentric cylinder, (b) parallel plate, (c) cone and plate.

2.3.3 Dynamic Rheology and the Cox-Merz Rule

According to the parameters shown in *Figure 2-6 (c)*, the shear rate, shear stress, and shear viscosity in a steady-shear flow (e.g., under step-strain mode) is given respectively as [55]

$$\dot{\gamma} = \frac{\omega}{\varphi} \quad (2.17)$$

$$\tau = \frac{3M_d}{2\pi R_p^3} \quad (2.18)$$

$$\eta = \frac{3M_d\varphi}{2\omega\pi R_p^3} \quad (2.19)$$

where ω is the angular velocity of the cone, φ is the angle of cone (usually is very small, thus φ is also expressed as $\sin \varphi$), M_d is the applied torque. The limitation of measuring the rheological properties of materials under this mode is that the flow instabilities (e.g., edge fracture) occurs when the applied stress or strain is too high. Therefore, the oscillatory shear deformation is preferred for testing polymeric materials as the strains are kept quite small.

When sample is deformed driven by sinusoidal strain, the resulting stress also varies sinusoidally with the same frequency but will be out of phase due to viscoelastic damping with the strain. The phase lag is called the phase angle δ between the input and response as is expressed as [52]

$$\gamma = \gamma_0 \sin(\omega t) \quad (2.20)$$

$$\tau = \tau_0 \sin(\omega t + \delta) \quad (2.21)$$

where $\omega = 2\pi f$ represents the angular frequency, γ_0 and τ_0 are the amplitude of strain and stress, respectively. The phase angle, δ , is equal to 0° for a pure-elastic material, 90° for a pure-viscous material. Phase angel for polymers are falls between 0° and 90° .

Equation 2.21 can be expressed in terms of storage modulus (G') and loss modulus (G'') as

$$\tau = \gamma_0(G'(\omega) \sin \omega t + G''(\omega) \cos \omega t) \quad (2.22)$$

where

$$G' = \frac{\tau_0}{\gamma_0} \cos \delta(\omega); \quad G'' = \frac{\tau_0}{\gamma_0} \sin \delta(\omega) \quad (2.23)$$

The storage modulus G' is a measure for stored energy of deformation and represents the elastic character of material. G'' is a measure of the dissipated energy in deformation and represents the viscous nature of the material. When $G'(\omega)$ is higher than $G''(\omega)$, in other words, the phase lag δ is smaller than 45° , the dominant viscoelastic property of the material is elastic, and vice versa.

The complex viscosity $\eta^*(\omega)$ in oscillatory testing is given according to the constitutive equation [55] as

$$\eta^*(\omega) = \frac{G^*(\omega)}{j\omega} = \eta'(\omega) - j\eta''(\omega) \quad (2.24)$$

where $\eta'(\omega)$ is equal to G''/ω , called dynamic viscosity, j is the complex number ($j = \sqrt{-1}$), and $\eta''(\omega) = G'/\omega$, $G^*(\omega)$ is the complex shear modulus

$$G^*(\omega) = G'(\omega) + jG''(\omega) \quad (2.25)$$

In the end, the magnitude of complex viscosity can be calculated from

$$|\eta^*(\omega)| = \sqrt{\eta'(\omega)^2 + \eta''(\omega)^2} \quad (2.26)$$

When only the complex viscosity data is available, it is natural to relate the measured complex rheological properties of polymers to the measurements under steady state. Cox and Mertz (1958) found an empirical rule, which is known as Cox-Mertz rule,

to transform the angular frequency dependent complex viscosity to the shear rate dependent viscosity [56], which is shown as

$$|\eta^*(\omega)| = \eta(\dot{\gamma}); \quad \omega = \dot{\gamma} \quad (2.27)$$

The above equation is well-known as the “simple” Cox-Merz rule. Since it was provided as an empirical relationship only within the accuracy of the corresponding experiments, more efforts have been made to assess its applicability for most of the polymers. Then, a more general expression is modified and justified by Barnes, et al. [57], Macosko, et al. [58], and Milner [59], which is given as

$$\lim_{\omega \rightarrow 0} \eta'(\omega) = \lim_{\dot{\gamma} \rightarrow 0} \eta(\dot{\gamma}) \quad (2.28)$$

where the angular frequency and shear rate are in lower limits due to the requirements for continuum mechanics. The elastic term ($\eta''(\omega)$) in complex viscosity is eliminated due to small frequencies. Hence *Equation 2.28* can also be expressed as

$$\lim_{\omega \rightarrow 0} \eta^*(\omega) = \lim_{\dot{\gamma} \rightarrow 0} \eta(\dot{\gamma}) \quad (2.29)$$

Cox-Merz rule has been proven a useful approximation in predicting the viscosity for most polymer melts and solutions when only the dynamic instruments are available during the half-century, its applicability has been reviewed in [60] and [61]. Most recently, the applicability and the possible failures of Cox-Merz rule has been examined in the study conducted by Snijkers, et al. [62]. The most distinctive contribution of the work of Franck is that it was the first time to critically assess the validity of Cox-Merz rule for the objective polymers with well-defined molecular structure. Their approach allows more clear identification of applicability of Cox-Merz rule concerning the molecular architecture, which benefits the development and of the existing empirical rules for linking the rheological data collected in dynamic oscillatory test to those in

steady-state experiments in a context of molecular theories. The experimental results decently obey to the Cox-Merz rule for the well-defined polymers: linear and monodisperse polymers of polyisoprene (PI) and polystyrene (PS), linear and polydisperse polymers of PS, monodisperse and symmetric polymers of PI, branched polymers of PS, and the blends of linear polymers with similar chemical properties. Though the common but minor deviation ($\eta^*(\omega) > \eta(\dot{\gamma})$) and uncommon failure ($\eta^*(\omega) < \eta(\dot{\gamma})$) can be observed at the highest accessible shear rate for most of the polymers and at low or intermediate shear rate for the branched polymers, respectively, it can be seen that the general Cox-Merz rule is well accepted for most of the polymer melts.

All the studies mentioned above [61,62] lay solid support for safely assuming that the Cox-Merz rule is applicable for the neat ABS and PLA (a linear polymer) filaments used in this thesis. Especially, for ABS, the validation of Cox-Merz rule has been experimentally demonstrated in [63].

In addition to pure polymers, the material used for this thesis also includes the short-fiber filled polymer composites. Generally, the flow-induced fiber orientation and interaction have great effects on the rheological properties of polymer composites. The attention has to be carefully paid on the applicability of Cox-Merz rule on these materials. Few studies exist in the literature that deals with this assessment for fiber reinforced polymers. Among these studies, the work conducted by Guo, et al. [64] that reported the applicability of Cox-Merz rule for the glass fiber filled linear low-density polyethylene (LLDPE). The experiments in [64] were performed in both capillary rheometer and torque rheometer for LLDPE composites at equivalent temperatures, and

the results are presented by comparing the deviation between the dynamic and steady-state data with the increased fiber volume fraction (from 0% up to 35%) and different aspect ratios of fibers. The experimental results state that the deviation increases with an increasing fiber loading. Another interesting finding is that the complex viscosity is lower than the shear viscosity in steady-state when tests at low shear rate, but it is larger when tests at high shear rate. This suggests, at least, the Cox-Merz rule is inapplicable for short glass fiber reinforced linear polymer composites. In this study, to compare the results predicted using the device built in this project to the assessable rotational rheometer, we apply the Cox-Merz rule for the carbon fiber filled filaments first, then examine the applicability of Cox-Merz rule on these materials..

CHAPTER THREE

Device Overview

This chapter provides a detailed overview of the design of the experimental system developed in this research for the rheological evaluation of polymer and polymer composite FFF filament. The first section introduces the measuring protocol used to guide the design of the device. The second section presents the system design, selection of components, and total cost of the prototyping. The third and fourth sections discuss the control and accuracy of the temperature measurements. The following section considers the signal analysis and methods used to process the output of the load cell. To conclude, the summary detailed specifications of the current version of the device are provided. Functional parameters such as temperature and filament feeding speed are highlighted in this chapter, which are both crucial to the system design as they guarantee constant volumetric flow rate during the extrusion process.

3.1 Measuring Protocol

Shear rate and shear stress are the necessary parameters used to predict the rheological behavior of polymer melts. However, the accurate measurement of these parameters is challenging in the FFF process due to the size and geometric complexity of the FFF nozzle. In general, commercial FFF nozzles used on 3D printers contain a transition region that is usually manufactured to be conical or tapered in shape reducing the flow cross-section to attain maximum desired extrusion rate of filament melts under laminar flow conditions [31]. Assuming the melt flow in a tube is Newtonian and

subjected to Hagen-Poiseuille law, shear force acted on the interior wall of liquefier and the apparent shear rate can be evaluated by measuring the pressure drop and volume flow rate through the control volume which is shown in *Equation 3.1* and *Equation 3.2*.

$$\tau_w = -\frac{\Delta P R}{2L} \quad (3.1)$$

$$\dot{\gamma}_w = \frac{4Q}{\pi R^3} \quad (3.2)$$

In the above, ΔP is pressure drop through the circular tube, R and L are radius and length of the tube, respectively, Q is volumetric flow rate, τ is shear stress on the tube, $\dot{\gamma}$ is the shear rate. Thus, the equation of shear stress, shear rate, and viscosity is transformed into the equation of pressure drop, volumetric flow rate, and viscosity, as

$$\tau_w = -\mu \dot{\gamma}_w \quad (3.3)$$

$$\Delta P = \frac{8\mu L Q}{\pi R^4} \quad (3.4)$$

where μ is the Newtonian viscosity. By measuring the force acting on the nozzle from the filament one can predict the pressure drop through a simple force equilibrium, the free body diagram will be given later.

The conceptual design for the test device used in this research is illustrated in *Figure 3-1* which separates the liquefier from the extruder. It is assumed that there is no slippage between the filament and the rollers and that the tension in the filament above the rollers does not contribute to the force measured in the load cell. Therefore, the frictional force along the interior wall of the liquefier and the force due to the pressure drop at the nozzle exit is regarded as the only forces of interest. If the frictional force between the solid portion of filament to the inside wall of heat barrier was ignored and the pressure at the nozzle exit is recognized to be equal to zero, then the resultant force at

the load cell is simplified to be the pressure drop over the entire nozzle multiplied by the inlet area as

$$F = \Delta PA + F_f \quad (3.5)$$

where A is the area of nozzle inlet, F is the resultant force, and the free body diagram is given in *Figure 3-2*.

$$\Delta PA = F_{s1} + F_{s2} \cos \frac{\beta}{2} + F_p \sin \frac{\beta}{2} + F_{s3} \quad (3.6)$$

where F_{s1} , F_{s2} , and F_{s3} are the friction force acted on the interior wall of the nozzle due to the shear of flow, β is the angle of the conical cylinder. Similarly, the volumetric flow rate can be obtained by measuring the mass flow rate divided by the density as

$$Q = \frac{\dot{m}}{\rho} \quad (3.7)$$

where \dot{m} is the mass flow rate, and ρ is the density of the filament feedstock.

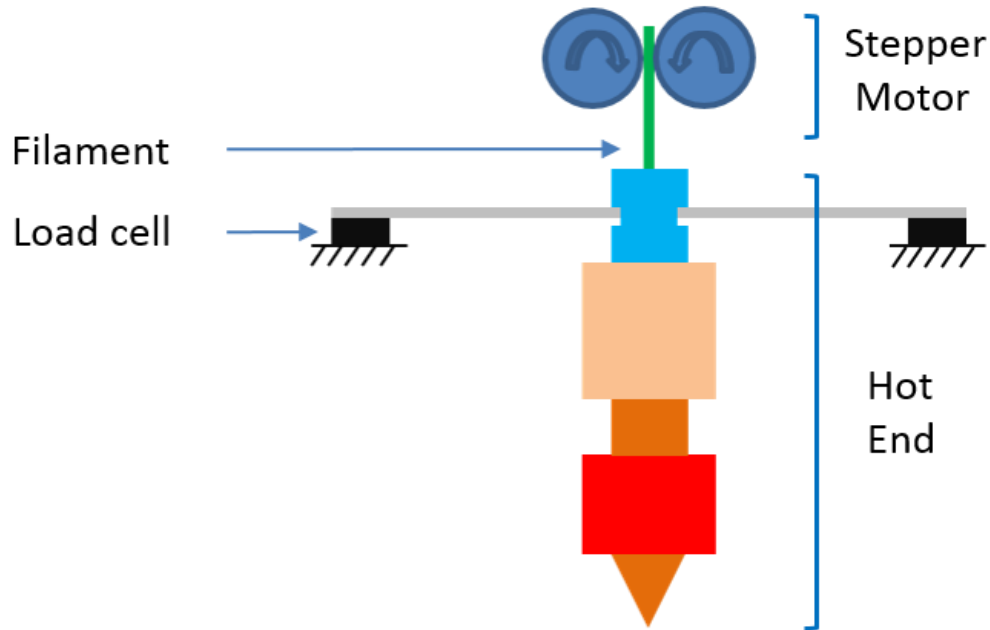


Figure 3-1 The measuring schematic of the device

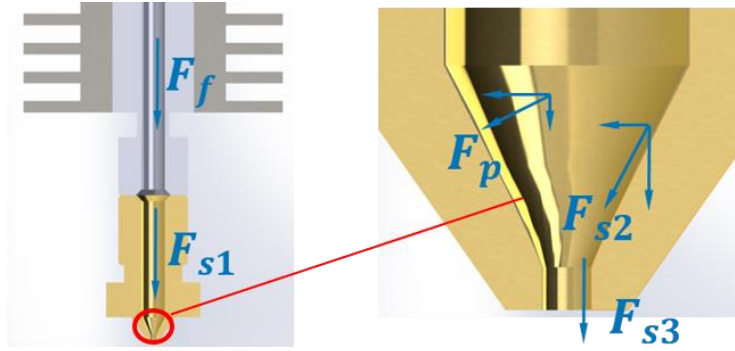


Figure 3-2 Free-body diagram of the system supported by load cell

3.2 Experimental Setup

The initial prototype of the filament rheometer system is designed using SOLIDWORKS (Dassault Systèmes, Education Edition, Waltham, MA), and rendering of the FFF filament rheometer developed in this research appears in *Figure 3-3*.

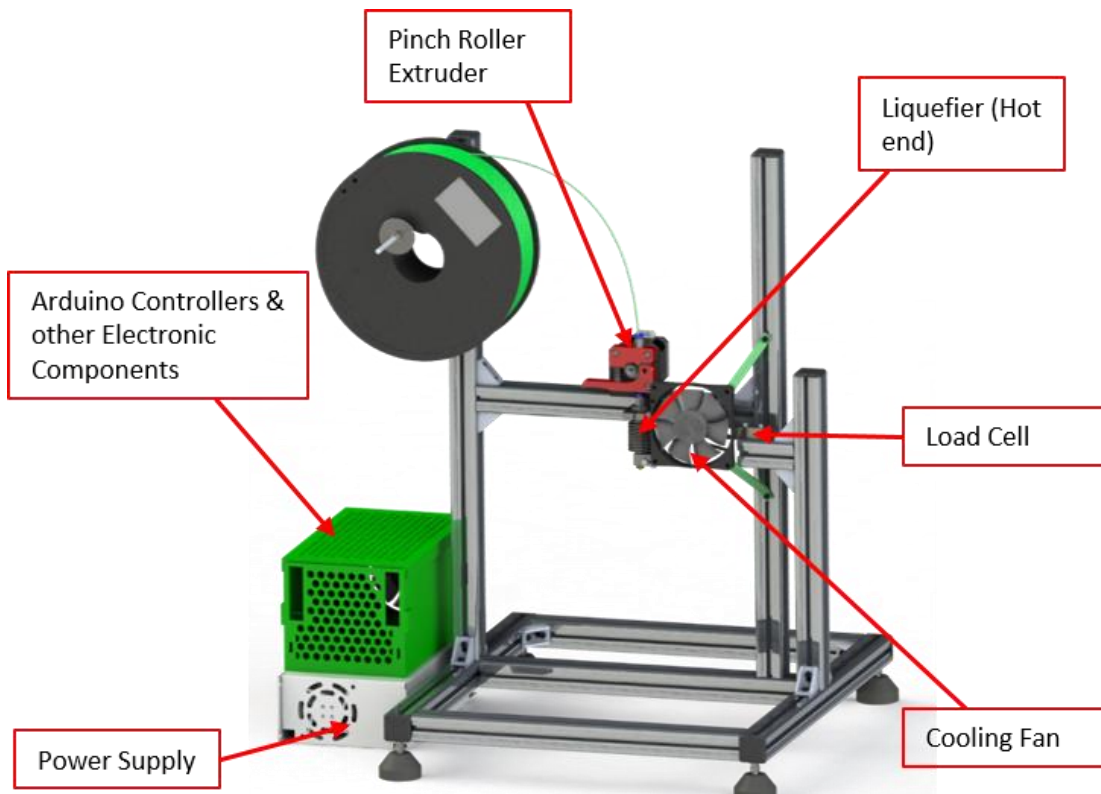


Figure 3-3 Conceptual Prototyping built by SOLIDWORKS

One of the main objectives of building this device is to characterize the filament materials and their rheological properties directly from the filament, quickly and economically. Hence, the components selected for this device are all inexpensive and easily accessible. The cost of the components for the prototype device appearing in *Figure 3-3* is given in *Table 3-1*. The total cost of prototyping is only \$177.17 which satisfied the objective of having a low-cost device.

Table 3-1 The cost of prototyping

Products	Quantity	Price
Power Supply	1	\$20.49
Arduino Uno	1	\$10.90
Arduino Due	1	\$32.99
Load Cell	1	\$8.03
HX711	1	\$8.99
Hot end	1	\$15.99
ADS1115	1	\$6.99
K type thermocouple	2	\$7.85
MAX31855	1	\$12.99
Stepper Motor	1	\$13.99
Extruder Frame	1	\$9.98
TB6600	1	\$14.99
Stainless Nozzle	4	\$12.99
Total	17	\$177.17

The final device used in this research deviated from the SolidWorks prototype as shown in *Figure 3-4* in order to facilitate more easily replacing the components and debugging the circuit connections. Later generations of the device would likely include a

custom frame such as that appearing in *Figure 3-3*. The introduction of each component will be discussed based on the group of their function in FFF in the sequent sections.

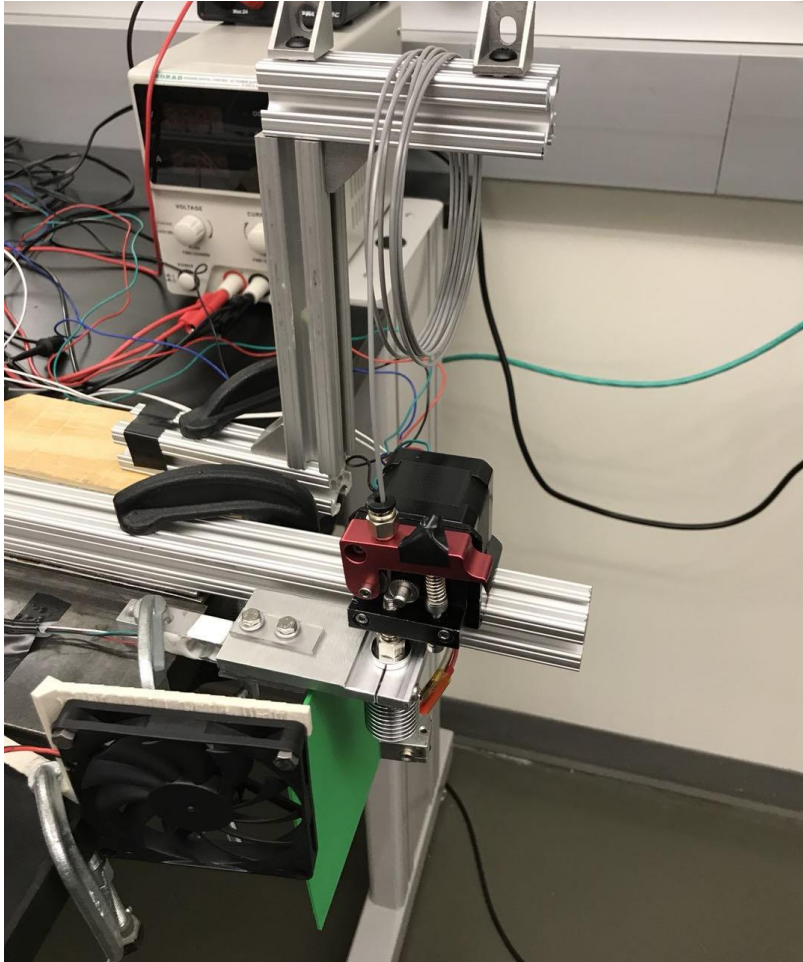


Figure 3-4 Actual Prototyping

3.2.1 Filament Feeding Mechanism

Almost all FFF systems use a pinch roller mechanism to push filament feedstock through the heated nozzle [65]. Typically, one of the rollers has a grooved surface (often designated the driver gear), and separate roller works as an idler pulley which may be grooved or have a smooth surface. *Figure 3-5* shows common rollers that are used in

desktop FFF 3D printers. Typically, a drive gear with a grooved surface is paired with a smooth idler in most applications. However, the opposite is also seen in FFF devices.



Figure 3-5 Different types of driver gears and idler pulleys

Distribution, sharpness, and depth of the teeth on a driver gear are all factors that determine its ability to grab the filament. The number of ‘teeth’ on the drive gear determines the smoothness of the filament delivery. The sharpness and depth of the teeth control the roughness of the roller-filament connection surface. It should be noticed that the combination of the grooved drive gear and flat idler pulley could provide more smooth delivery because of more teeth on the drive gear. However, the teeth are too dense on this kind of drive gear, the filament can be easily stripped. After testing, it was found that assemblies with a flat-surface driver and grooved-surface idler are a better choice for our design. This combination has the capability to deliver the filament without slipping and grinding even at higher speed (e.g., 8 RPM or $4.29e^{-3}$ m/s as the average feeding velocity of the filament). In addition to the properties of drive gear itself, the gripping force between the filament and each of the two rollers, i.e., the compress force in the drive mechanism has a significant affect on the filament friction force. The effect of this drive roller friction force on filament delivery will be discussed in detail below.

The filament drive mechanism frame chosen is shown in *Figure 3-6 (a)*. This type of extruder frame has an adjustable spring to provide a higher friction force on the filament by tightening the spring which is required when operating the device at a higher filament throughput speed, and when extrusion forces are high.

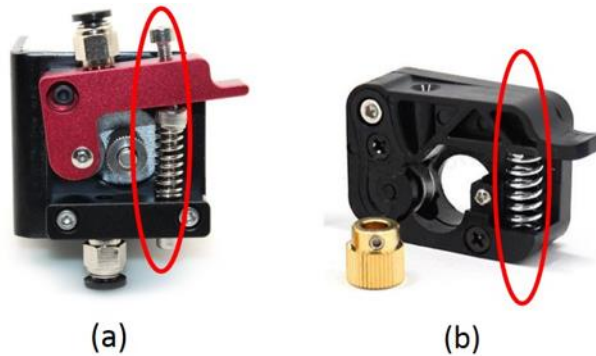


Figure 3-6 Comparison of different extruder frames

To examine how the tightness of the spring affects the force measurement in the liquefier, several experiments were conducted under fixed temperature and feeding speed where the only varying factor is the compression force of the spring. Due to the complexity of measuring the compressive force in the spring, we consider the amount of spring compression as defined by the distance d in *Figure 3-7* between the top of the spring to the underside of upper filament delivery frame as shown.

Measured values of filament force (please reference how the force is measured in *section 3.5*) at various spring displacements. It is observed that if the compressive force in the spring is too small which can be seen when $d = 5mm$ in *Figure 3-8*, slippage will occur between the drive gear and filament. In contrast, if the force is too large, such as the case when $d = 20mm$, the measured force signal becomes noisy and irregular which is likely due to the filament buckling or getting stripped.

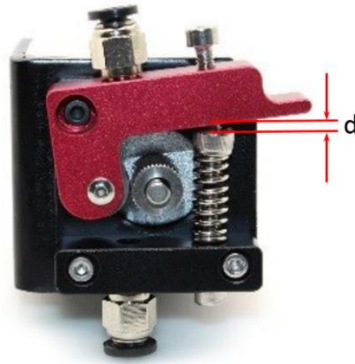


Figure 3-7 Adjustment of spring tightness

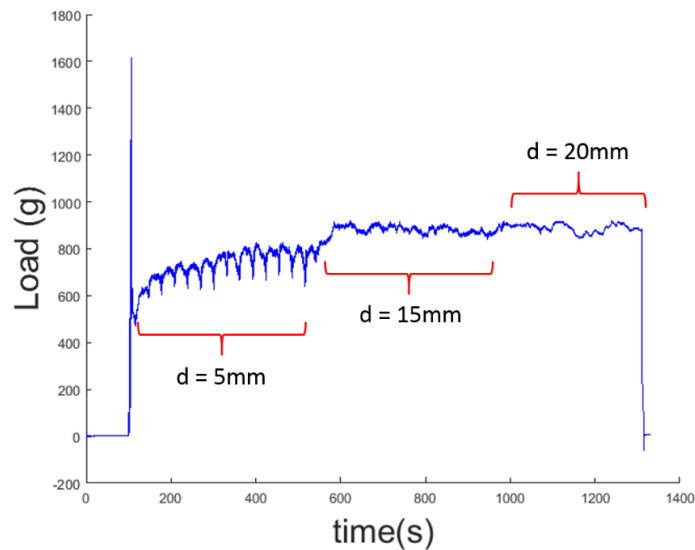


Figure 3-8 Effect of spring compression on force measurement of filament extrusion

The stepper motor that drives the filament is connected to the driver gear to generate stable and continuous force on filament. Stepper motors turn a precise angle or step as controlled by a digital pulse input. The motor's angular position can be accurately controlled via the driver without a feedback mechanism such as Proportional-Integral-Derivative controller (PID) or Pulse Width Modulation (PWM) controller. The 2A 59N·cm Nema 17 bipolar stepper motor is chosen in this project. The 2A designation indicates the rated current for the stepper motor. Our motor is designated as a 59N·cm

which is the holding torque of stepper motor. The actual torque produced by a stepper motor at a given speed depends on many factors such as the step rate and the current passing through the windings. We do not have equations to calculate the running torque of our stepper motor, however, the pullout torque curve is shown in *Figure. 3-9* indicates how torque changes with speed. Here, pullout torque is the maximum torque a stepper motor can generate at a given speed [66].

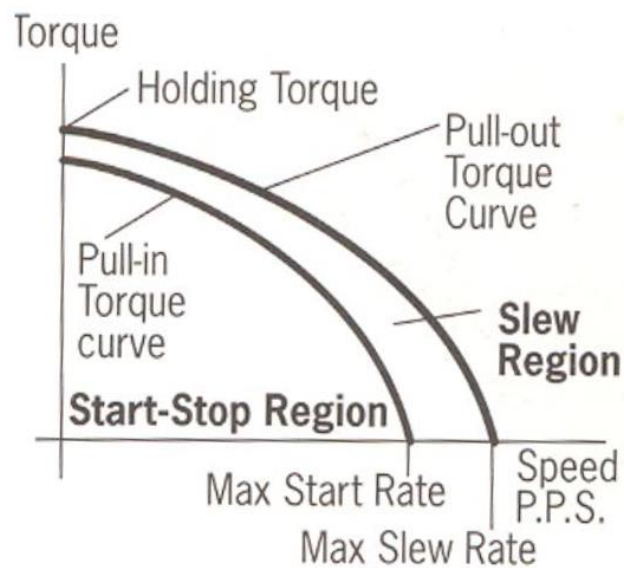


Figure 3-9 The torque-speed curve of a stepper motor [66]

The step angle of our Nema 17 motor is 1.8° which means it has 200 steps per revolution under a full-step condition. One way to minimize the vibration of the system due to the start and stop of each step of a running stepper motor is to smooth the motion of the motor. To this end, we employ the TB6600 stepper motor driver shown in *Figure 3-10* which can subdivide each step into 32 micro-steps by driving the motor under 1/32 micro-step condition. This is a significant improvement that reduces the effective step angle to 0.05625° , resulting in a smoother roller motion when compared to the motor

alone. Furthermore, one can adjust the current going through the stepper motor to optimize the available torque under micro-step mode.

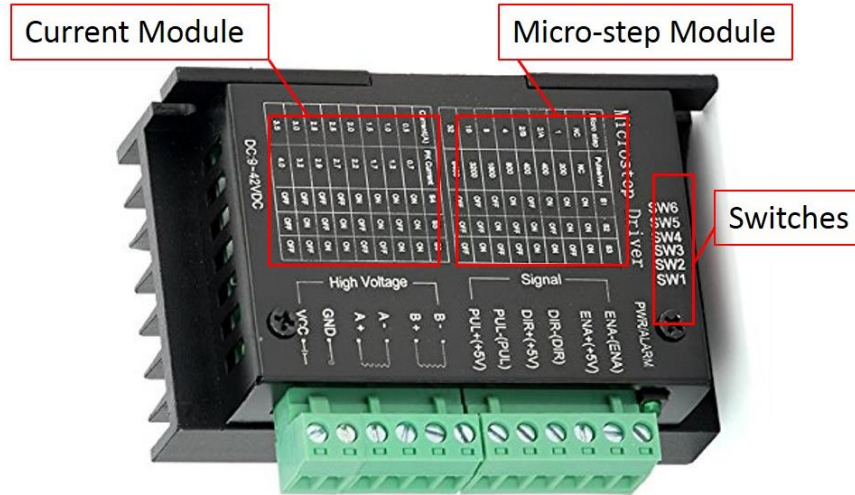


Figure 3-10 TB6600 stepper motor driver

The position of a step in our device has a 3% - 5% error as given by the manufacturer that is not accumulative from step to step [67]. The error from the Arduino board and the motor driver itself will generate a discrepancy of the actual RPM of the stepper motor as compared to the computational value, resulting in the measurement error for filament feeding velocity. To reduce this error and ensure that the system maintains an accurate and stable filament throughput velocity, both computation and experimental measurements are performed. A simple calculation of delay time for the stepper motor in Arduino IDE at a certain RPM can be obtained from the derivation in *Figure 3-11*.

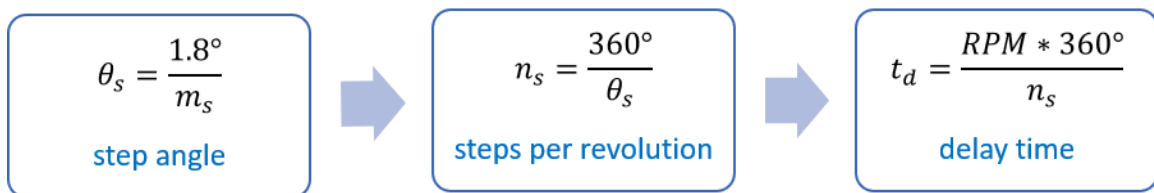


Figure 3-11 Derivation of calculating time interval of each digital pulse

In the above, m_s is micro steps, θ_s is step angle, and t_d is the delay time between each digital pulse. The actual delay time is found by subtracting 288 microseconds from the analytical results for each loop where the redundant 288 microseconds is determined experimentally. The resulting delay time has proved valid for each RPM starting from 0.5 to 8 RPM with 0.5 RPM increment. Therefore, the speed of delivering filament can be accurately controlled by changing the delay time in Arduino IDE as needed.

3.2.2 Liquefier I. Cooling System

The liquefier is the part of the FFF extrusion system where the filament is melted, and it often includes a cooling system for controlling the location of the filament's melting region. Controlling the location where filament softens get melted is essential in this project since the melting zone effects the pressure drop measurement. The role of the melting zone in our research will be discussed further in *Chapter Five*. The cooling system consists of three components, cooling fan, heat sink, and heat break (also referred to as the heat throat or heat barrier). The heat sink is used to dissipate heat from heat break by convection. The heat break is applied to reduce heat conduction from heater block to the upstream part of the hot end. "Heat creep" is a common issue that exists in the FFF 3D printing process, as shown in *Figure 3-12*. The primary cause of heat creep is poor heat dissipation upstream of the nozzle. The efficiency of a cooling fan is one of the critical factors that affect the heat conduction. In the thermal analysis by Annet [68], the significant improvement of heat dissipation is clearly seen after applying the external fan facing to a heat sink as shown in *Figure 3-13*.

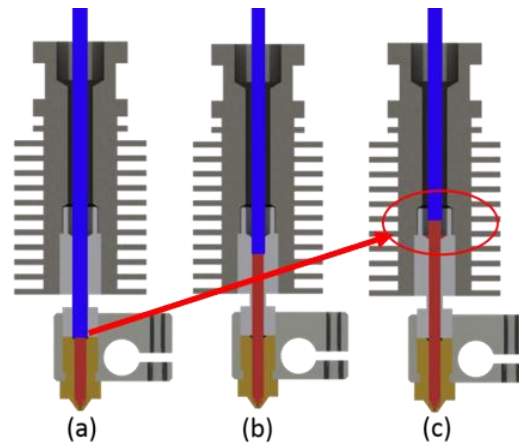


Figure 3-12 Heat creeping (red color marks the melted filament; blue color marks the solid filament). (a) Desired melt region of filament; (b) Melting region is expanded upward; (c) Melting region passes over the inlet of heat barrier which can cause clogging.

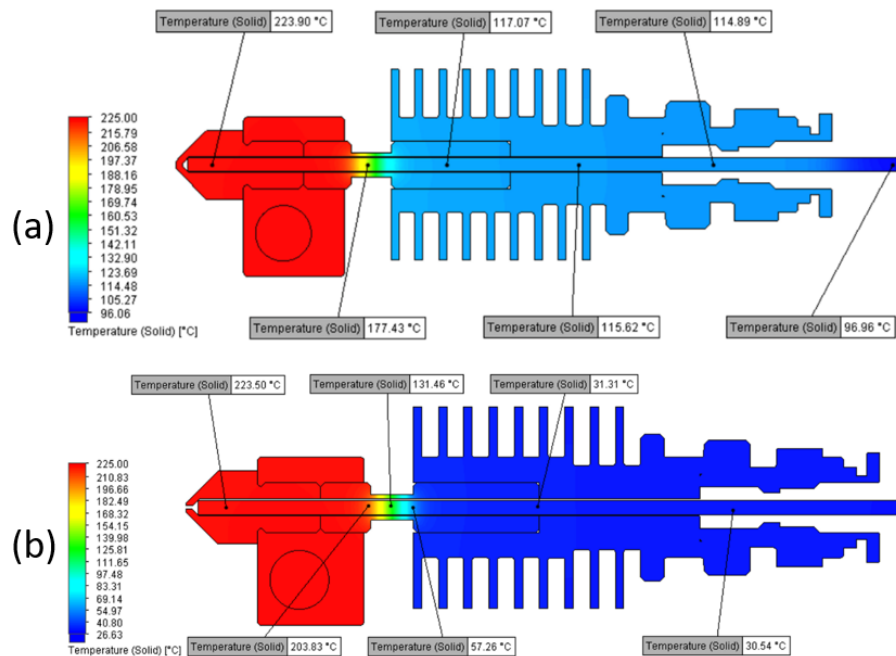


Figure 3-13 Comparison of thermal dissipation (taken from Annet [68]): (a) Temperature map for liquefier without out cooling fan applied; (b) Temperature map for liquefier with cooling fan attached.

Heat breaks are classified into two types according to their material and structure; one is called all-metal heat break and another has the name of “PTFE heat break”. As the name implies, the all-metal heat break is made from metal such as a stainless steel and/or

a titanium alloy. This kind of heat barriers is usually employed to print FFF polymer materials that has a high melting temperature like nylon and PC. Unfortunately, the ability to control the thermal conduction in a metal heat break is not good.

Comparatively, the “PTFE heat break” is a hybrid one that a PTFE tube is inserted into a stainless steel frame. The disadvantage of this kind of heat break is that it is unable to withstand a higher temperature (above 240°C) because of the decomposition of PTFE.

Therefore, the trade-off of selecting the right heat break depends on the filament feedstock and cooling methods being used. In this research, the PTFE heat break is chosen in the liquefier, because all the polymers and polymer composites used have relatively low print temperatures (i.e., lower than 240°C). Analyses of the thermal properties of the materials used in this research will be given in the material thermal analysis section in *Chapter Four*.

3.2.3 Liquefier II. Heating System

A 12V 40W ceramic cartridge heater, 100K NTC Thermistor, K type thermocouple, and nozzle are assembled in a heater block to maintain the uniform extrusion temperature. As shown in *Figure 3-13 (a)*, the desired melting region of filament should be confined within the nozzle. However, results published by Annet [68] and Jerez-Mesa, et al. [69] show that the melting zone often extends beyond the top of the nozzle such that melted polymer is seen within the thermal barrier at the top of the heater block (c.f. *Figure 3-12 (b)*). The dimension of the heater block could be another influential factor of melting region in addition to cooling fan and heat break. *Figure 3-14* illustrates that the heater block on the left side has a smaller size in thickness which

means the shorter portion of heat break will be inserted, allowing part of the heat break to be exposed and cooled in the air.

The heater in our device is powered by 12V DC power supply and controlled via a transistor which acts as an electronic switch by turning current on and off. A schematic of a transistor appears in *Figure 3-15*. A transistor can control the high current and voltage loads from the lower voltage and current side. If the voltage between the base (always connected to the controller) and collector is less than 0.6V, the current from the collector (connected to positive pole) to the emitter (connected to negative pole) will be blocked. Otherwise, the transistor will be turned on. More details will be covered in the section of PID control in Section 3.4.



Figure 3-14 Comparison of thickness of two heater blocks

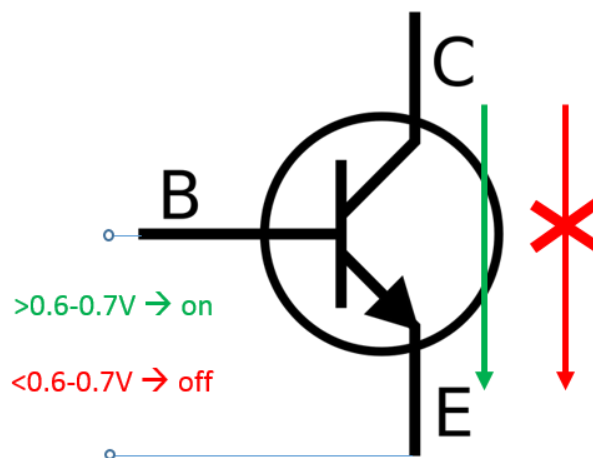


Figure 3-15 Transistor working principle

For general bipolar transistors, when they get hot, the current passed through will also increase due to the increase of current gain which cause further heating generated, sometimes even burn the transistor. To reduce the heat generated by transistor, an IRFP150 NPN MOSFET transistor is used in our device. In general, when metal-oxide-semiconductor field-effect transistor (MOSFET) is heated up, the current that passes through it will decrease.

A Negative Temperature Coefficient (NTC) thermistor is used in our device as the primary temperature sensor to monitor extrusion temperature. The thermistor is made from semiconductor where resistance decreases when the temperature increases. In addition, a K-type thermocouple is used for comparison to verify the accuracy of reading from thermistor. The thermocouple is connected to a Max31855 to convert the voltage to temperature. The thermistor used in this device is shown in *Figure 3-16* where it can be seen that it has a very small tip such that its sensitive range is somewhat limited. Unlike the thermistor, the K-type thermocouple has a larger cap. Thus the reading from thermocouple is an average value over a larger region than that in the thermistor. To help ensure that both devices record the same temperature, a hole is drilled into the heater block to make sure thermocouple is thoroughly immersed within it. This adjustment allows thermistor and thermocouple have the same distance to the nozzle screw hole (*Figure 3-16*).



Figure 3-16 Configuration of two sensors in heater block with equal space to nozzle screw

The nozzle is the heart of our “Filament Rheometer.” Its geometry not only defines the pressure drop in the system but also determines the size and shape of the extruded bead. Six nozzles appearing in *Figure 3-17* from different manufacturers were cross-sectioned and sanded by a 3D measurement device to measure their inside dimensions. Note that nozzles for FFF 3D printers on the market have a high tolerance for variation of the interior nozzle geometry. Note that some of the nozzles in *Figure 3-17* have contraction regions that are rounded, but others are conical. One can also see one of the nozzles even has a serious flaw that the capillary die is not aligned with the axis of the upper die body. Therefore, nozzles have to be carefully chosen before conducting the experiments. Also, the material of the nozzle should also be considered with regarding the filament feedstock. Carbon fibers in the filament are short and have high stiffness. Thus the fiber reinforced filament melts are very abrasive. Therefore, a long-running extrusion of carbon fiber filled filament can easily abrade the nozzles made from brass. Though the stainless nozzle is usually chosen to run CFR-ABS, one needs to be careful to monitor the abrasion.

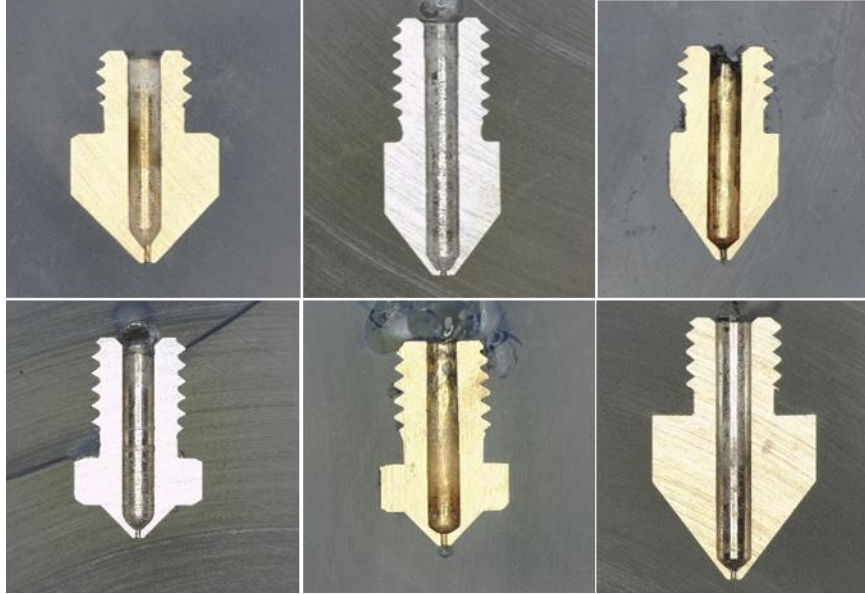


Figure 3-17 Comparison of different nozzles by examining their inside geometries

3.2.4 Force Transducer

A four-wire strain gage based beam-type load cell (see, e.g., *Figure 3-18*) was found to work well for measuring the force exerted on the liquefier by the moving filament. Our cantilever beam load cell is not only used for both static and dynamic forces but also is cost-effective. A strain gage is used to measure strain on the surface of the bending beam which is proportional to the changing in resistance of foil [70]. Correspondingly, an HX711 amplifier is used to accurately measure the small change in resistance when a load is applied to the beam. Note that the HX711 can operate at a sampling rate of 10 samples per second (SPS) or 80 SPS (i.e., at 10 HZ and 80 HZ). One of the disadvantages of the strain-gage-based load cell is that it has a relatively slow speed of response. Thus, the HX711 is has a 10 HZ sampling rate as default [71]. Under 80 HZ, the measured data becomes less accurate.

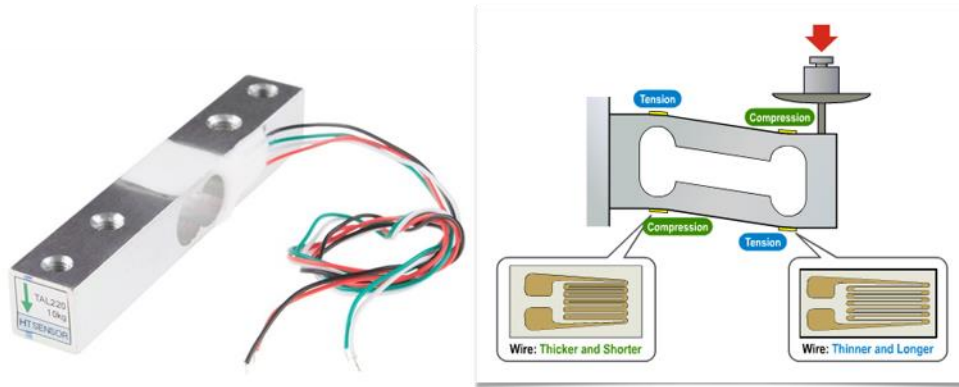


Figure 3-18 Strain-gauge-based Beam Load Cell

A liquefier holding fixture for our FFF filament rheometer firmly fixes the hot end onto the load cell during extrusion which is designed to minimize the error from the vibration. As shown in *Figure 3-19*, the left side of the liquefier holding fixture is fixed to the load cell by screws; the right side has a movable clamp to secure the hot end.

Meanwhile, a polycarbonate plate is placed between the top of the load cell and the liquefier holding fixture to insulate the beam force transducer from heat generated in the liquefier. This additional insulation reduces errors in load cell reading due to increased temperature and thermal expansion on the strain gauge.

The distance from the force transducer strain gauges to the force application point at the liquefier is approximately 80 mm making it necessary to examine the influence of the length of the moment arm on force measurement. The standard 20 g and 100g weights as well as a set of steel plates are suspended from the load cell via a carbon fiber laminate as shown in *Figure 3-20*. Nine measurements were taken, each having a different distance between the load application point and the center of beam load cell. It shown in *Table 3-2*, the beam-type load cell produced the same load reading for all locations of

force application point, thus providing confidence that our force measurements do not depend on location of the hot end on the load cell.

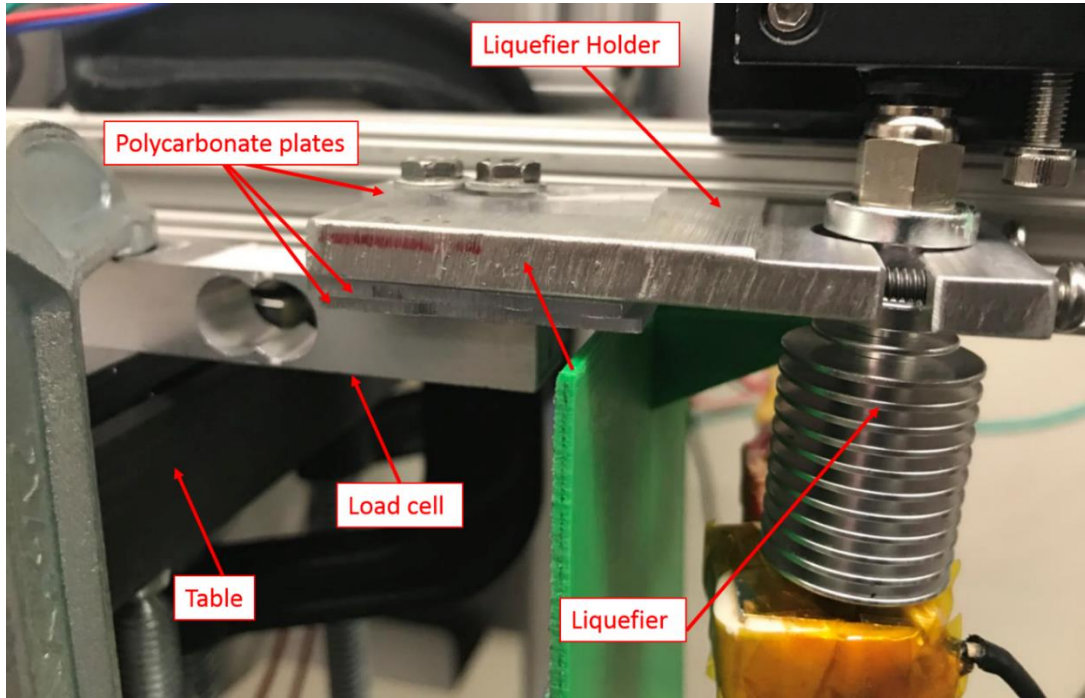


Figure 3-19 Configuration of the liquefier holder

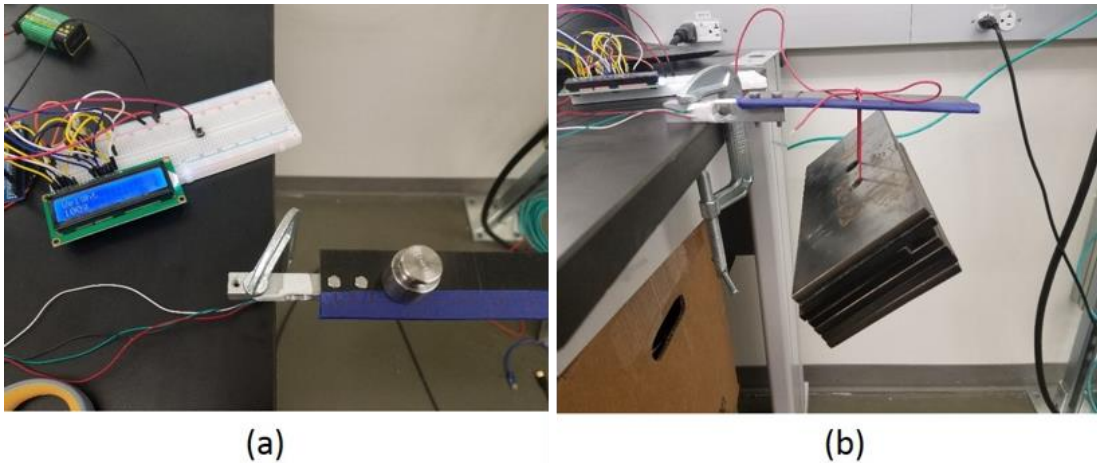


Figure 3-20 Bending tests: (a) 100 g weight; (b) 8226 g steel plates

Table 3-2 Tests of examining the influence of arm of force on load cell measurement

Distance (mm)	20 g weight Reading (g)	100 g weight Reading (g)	8226 g steel plates Reading (g)
30	20	100	8227
50	20	100	8228
90	21	101	8228

3.2.5 Control System

Generally, commercial FFF desktop 3D printers like MakerBot (Brooklyn, New York) prior to 5th generation, Ultimaker (Netherlands), and the RepRap (reprap.org) 3D printers are controlled by the pre-compiled firmware. Though different brands of 3D printers have their configuration, their firmware executes instructions given by G-code, also known as G programming language, which is always generated by the slicing program automatically. From the perspective of 3D printers, the G-code contains the commands such as heating the nozzle to a specific temperature, moving the print head to specified coordinates, adjusting the feeding velocity and so forth. However, neither the firmware nor the programming code is suitable for our objective to build a filament rheometer due to the complexity of modifying the G-code.

Arduino is an open-source electronics prototyping platform that offers a programmable controller that can readily be adapted to our device [72]. Therefore, we use Arduino boards and associated hardware to build the FFF filament rheometer device in this research. Employing the Arduino IDE [73] software, the Arduino boards can control the sensors and other items physically and digitally. Arduino Uno [74] is used as the secondary controller to control the stepper motor that delivers filament through the

liquefier. Arduino Due [75] is chosen to work as the primary controller in order to control the temperature, measure the force, and send instructions to Arduino Uno. The data of interest was displayed and collected by Serial Monitor.

Since our device is considered a prototype, all electronic components are wired on a breadboard. A customized printed circuit board (PCB) to perform the same tasks is left for future work.

3.3 Temperature Performance

The viscosity of polymers and polymer composites are dependent on shear rate and temperature, thus maintaining the extrusion temperature is extremely important to improve the accuracy of measurement. Among the widely-used temperature sensor (see e.g., *Figure 3-21*), thermistors and thermocouples are selected based on factors such as the requirements in this project, the cost, and performance.

	Thermocouple	RTD	Thermistor
Temperature range	Best (-200 °C to 1700 °C)	Better (-200 °C to 800 °C)	Good (-55 °C to 300 °C)
Accuracy	Good	Better	Best
Cost	Best	Good	Better
Sensitivity	Good	Better	Best

Figure 3-21 Comparison of most widely used temperature sensors [76]

3.3.1 NTC Thermistor

In our work, the 3950-100K-NTC thermistor is used as the primary temperature sensor to measure the temperature in the nozzle. Using an external 16-bit analog-to-

digital (ADC) board, the NTC thermistor can measure the temperature over a range of 180°C to 240°C within 0.1°C resolution. Details on the use of the NTC thermistor in the filament rheometer and the efforts to improve the temperature measurement will be discussed in this section.

3.3.1.1 Introduction of NTC thermistor. A thermistor is a type of resistor whose resistance value changes with the temperature. As mentioned previously, the NTC thermistor has a negative thermal coefficient, in other words, the resistance is inversely proportional to temperature. A temperature value of 100K denotes that the resistance of this thermistor at 25°C is around 100 KΩ. The value 3950 is the value of coefficient β in *Equation 3.13*. Thermistors have a high sensitivity of resistance to temperature but typically the temperature measurement range is narrow [77]. In addition, thermistors typically exhibit a nonlinear temperature-resistance relationship as shown in *Figure 3-22*.

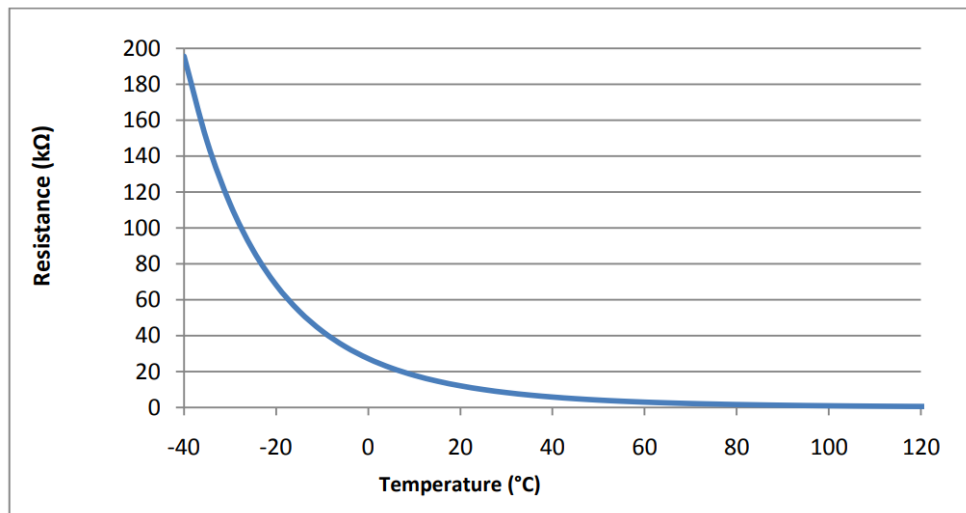


Figure 3-22 Resistance versus Temperature for a 10K NTC thermistor [78]

3.3.1.2 Resistance measurement. Acquisition of thermistor temperature data requires two steps that include, 1) resistance measurement and 2) temperature calculation. First, the real time resistance of a thermistor has to be measured before measuring temperature. While a multimeter may be used to measure the resistance, however, the Arduino may be employed for this purpose by creating an “Ohm-meter” which converts a voltage signal to a resistance. A voltage divider is an elementary circuit used to control or measure the output voltage on the resistor is of interest as shown in *Figure 3-23*. In this way, the resistance of a thermistor can be directly calculated using Ohms law when the input voltage and resistance of the reference resistor is known. Arduino Due has a built-in 10-bit ADC board that allows it to read an analog signal such as the voltage which is mapped to integers from 0 – 1023. Typically, the Arduino Due can provide 3.3V and 5V (have to wired protection resistors to SDA and SLC) power to the circuit. *Figure 3-24* illustrates the steps to measure the resistance of thermistor.

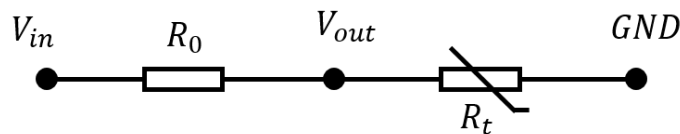


Figure 3-23 Voltage Divider

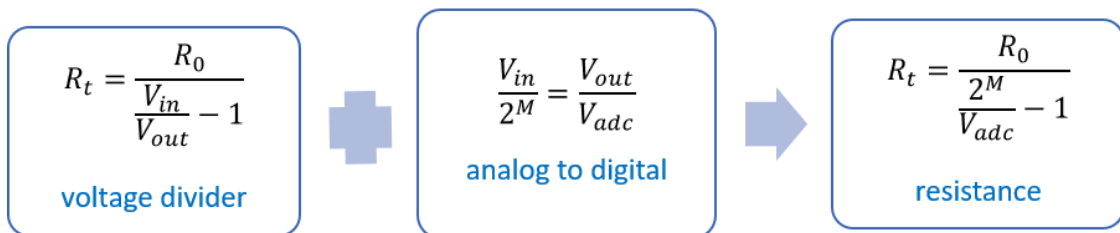


Figure 3-24 Derivation of the resistance calculation for a thermistor

In our work, V_{in} is 5V (if VCC is connect to a 5V pin on Arduino), V_{out} is the voltage across the thermistor, M is ADC's resolution in bits, and V_{adc} is the analog reading.

The above calculation provides a basic introduction to measuring the resistance but lacks information about accuracy and resolution concerning the objective of this research. Therefore, several improvements have to be made to reduce measurement error and get high-temperature resolution even at high-temperature values such as 240°C.

First, the ADS1115 4-channel ADC board is used to provide 15-bit (0 - 32767) resolution analog reading under single-ended mode which is much higher than the built-in ADC on Arduino Due (0 – 1023). If one simply calculates the resistance of the thermistor according to the procedure shown in *Figure 3-24*, an unacceptable error will result since the voltage at VCC and GND are 5V and 0V, respectively. To avoid this error in our research, the voltage divider appearing in *Figure 3-25* is employed. Instead of measuring voltage at VCC and GND, we directly read the voltages at V1 and V2, such that the resistance of thermistor can be calculated using *Equation 3.8*.

$$R_t = \frac{V_0 - V_1}{V_2 - V_0} R_0 \quad (3.8)$$

As a result, the gain error is eliminated from the calculation [78].

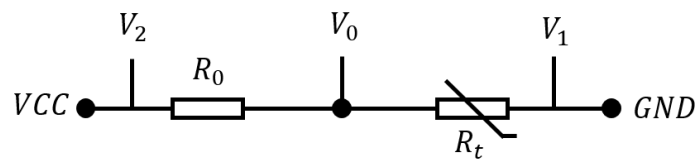


Figure 3-25 Ratiometric method of measuring thermistor's resistance

Selection of the resistance of reference resistor must be addressed for successful implementation of the thermistor. There are two factors needed to be considered in this

process which are resolution and self-heating. Typically, the resistance of the reference resistor is chosen to be equal to the resistance of thermistor. Therefore, to achieve the desired resolution over the desired range of temperature, the reference resistance is chosen near the midpoint of that range. If one requires more accuracy at either of the extreme temperatures, the reference resistor's resistance could be adjusted accordingly. Since the goal of this project is to process polymers and polymer composites above their melting points (i.e., in the range of 180-240°C), a resistor with low resistance should be considered. As given in the reference datasheet for the 100K NTC thermistor from EPCOS [79], the resistance at 210°C (the middle point of the above temperature range) is 459 Ω. Thus, 459 Ω is selected as the resistance of reference resistor to give the best resolution for our device.

However, considering only resolution is insufficient when selecting the resistance of reference resistor to be 459 Ω. Self-heating should also be considered which has an error defined as

$$T - T_0 = \frac{P}{K} \quad (3.9)$$

where K is the heat dissipation constant, P is the electrical power on thermistor, T is thermistor's reading, and T_0 is the actual surrounding temperature. If the reference resistance is too small, the thermistor will receive a higher bias voltage which increases the self-heating error. The heat dissipation constant K was measured to be between 1.6 – 3.1 mw/°C for our device. Setting the temperature tolerance of self-heating to be 0.01°C yields a minimum resistance for reference resistor of 8525 Ω is computed from

$$P = I^2 R \quad (3.10)$$

$$I = \frac{5 V}{(R_{240} + R_0)} \quad (3.11)$$

Finally, a 9922 Ω reference resistor satisfies the self-heating requirement for our device. As mentioned above, the thermistor's resistance decreases temperature, and it follows that the bias voltage on thermistor decrease with temperature as well. Therefore, if the thermistor can be maintained with at least 0.1°C resolution at the maximum temperature of interest, then we impose the same resolution temperature measurements below the maximum temperature of 240°C. We measured the resistance of thermistor at 240.1°C and 240°C to be 248 Ω and 252.5 Ω , respectively. Thermistor voltages corresponding to these temperatures are, respectively, 121.9272 mV and 124.0847 mV. Therefore, the voltage changes 2.1575 mV per 0.1°C. Since the 16 bit ADC board is used, the resolution of digital voltage is computed as $6.144V/2^{15} = 0.1875 \text{ mV}$, where 6.144V is the maximum input of ADS1115. Obviously, the voltage change per 0.1°C (2.1575 mV) is much larger than the ADC resolution (0.1875 mV). In other words, the microcontroller has the ability to measure the temperature change within the desired 0.1°C resolution.

One final note is that all resistors used to build the circuit are the metal film type resistors since this type of resistor is stable with little resistance change from variations in temperature or applied voltage.

3.3.1.3 Temperature calculation. Once the resistance of thermistor is accurately measured, the next step is to convert resistance to temperature. We use the Steinhart-Hart equation [80] to calculate temperature T in Kelvin) for a wide our thermistor which may be written as

$$T^{-1} = A + B \ln(R) + C(\ln(R))^3 \quad (3.12)$$

Where R is the resistance, T_0 is the reference temperature at the corresponding resistance R_0 , and A , B , and C are constants. An alternative option is the Beta parameter equation which may be written as

$$\frac{1}{T} = \frac{1}{T_0} + \frac{1}{\beta} \ln\left(\frac{R}{R_0}\right) \quad (3.13)$$

In the above, there are two unknowns, coefficient β and one variable R , which need to be determined.

The coefficients in the above equations (cf. *Equation 3.12 and 3.13*) must be carefully calculated to promote the accurate temperature readings of thermistor. Nonlinear least-squares regression provides a way to curve fit the coefficients accurately. Therefore, a set of data of temperature versus resistance is measured for the thermistor used on the filament rheometer. In our approach, the thermistor is loaded in a calibration instrument, i.e., ETC-400A (AMETEK Inc, Berwyn, PA) which can keep the isothermal condition for thermistor. The resulting resistance of thermistor is measured using the 334410A (Keysight, Santa Rosa, CA), a digit multimeter. The procedure is shown in *Figure 3-26*. Repeating the measurements within a large temperature span to ensure the optimum curve fitting result, and the data is given in *Table 3-3*.

The manufacturers usually give the temperature versus resistance table (e.g., *Table 3-3*) along with the thermistors that have the same specifications. The example can be seen in [81] and [82]. Some open-source code (e.g., Marlin Firmware [83]) employs the interpolate algorithm for the table to read the temperature. In this project, four thermistors with the same specifications (i.e., the Beta coefficient is equal to 3950; the resistance of thermistor at 25°C is 100 kΩ) are calibrated. The results are given in *Figure*

3-27. It is noticed that the largest temperature difference is around 8°C which demonstrates the necessity of the calibration for thermistor used on the FFF-based machines.

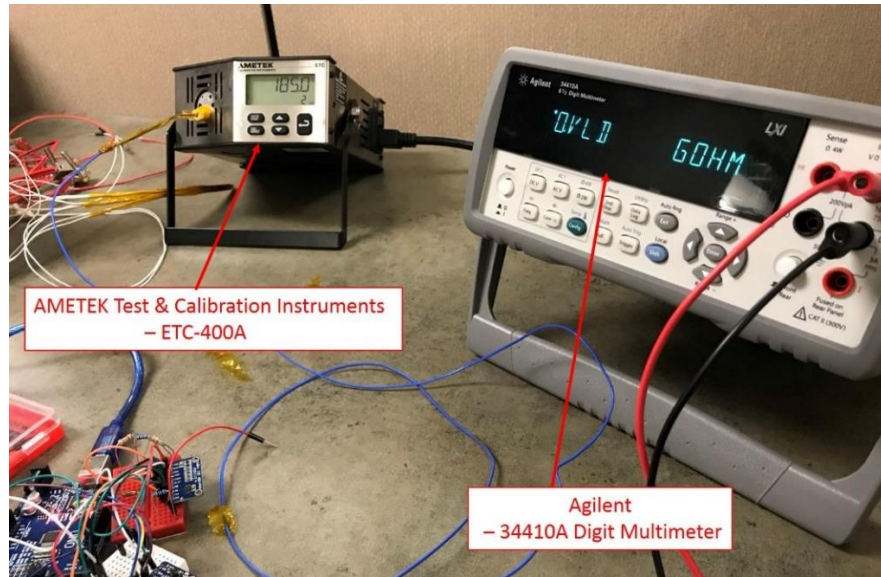


Figure 3-26 Thermistor calibration

In the curve fitting process, the value of $C = 0.0000001884$ was determined with nine decimal digits if accuracy. However, Arduino Uno is only able to compute floating-point numbers with 6 – 7 decimal digits [84], thus the constant C will need to be truncated when using Uno as the temperature microcontroller. To examine how this affects the temperature measurement, the calculated temperature curves are shown in *Figure 3-28* based on *Equation 3.12*. When the C coefficient is not represented accurately, a 10°C error will be generated at a thermistor resistance or 449.2 Ω. To avoid this error, an Arduino Due capable of storing a 15-digit number [85] is chosen as the primary controller to measure and control the temperature for our research.

Table 3-3 Lookup table for the four NTC thermistors used in the project

Temperature (°C)	NO.1 (Ω)	NO.2 (Ω)	NO.3 (Ω)	NO.4 (Ω)
25	100300	99790	113860	100880
30	80830	80520	91865	81230
35	65508	65320	74470	65750
40	53346	53300	60730	53530
45	43730	43725	49760	43790
50	35975	36060	40994	36030
55	29777	29863	33966	29780
60	24751	24880	28238	24754
65	20680	20799	23607	20652
70	17333	17488	19806	17314
75	14606	14740	16705	14575
80	12355	12496	14129	12325
85	10476	10623	12010	10463
90	8935	9070	10244	8897
95	7649	7768	8751	7609
100	6566	6694	7520	6537
105	5663	5775	6487	5633
110	4994	5005	5609	4870
115	4248	4350	4871	4223
120	3694	3793	4237	3674
125	3225.5	3315	3698	3204
130	2820	2910	3238	2804
135	2476	2558	2842	2461
140	2176	2259	2503	2167
145	1923	1995	2209	1913
150	1698.5	1769	1954	1691
155	1505.5	1573.5	1730	1500
160	1333.5	1401.7	1534.2	1335.5
165	1182	1250	1361	1186
170	1053	1121.7	1211.8	1062.5
175	928	1003.5	1079	936.5
180	830.3	896.8	950	843.5
185	743	808	850	758
190	666.6	730.1	764.5	684.5
195	598	661	687	617
200	538.3	598.5	618.5	559.2
205	486	545	557.7	507
210	438.8	495.3	504.7	460.5
215	397	452.3	457	417.7
220	359.7	412.7	424.2	380.6
225	326.2	376.7	375.8	346.2
230	296.6	345	342	315.5
235	270	316.6	311.5	287.8
240	246.2	291	284	263.2

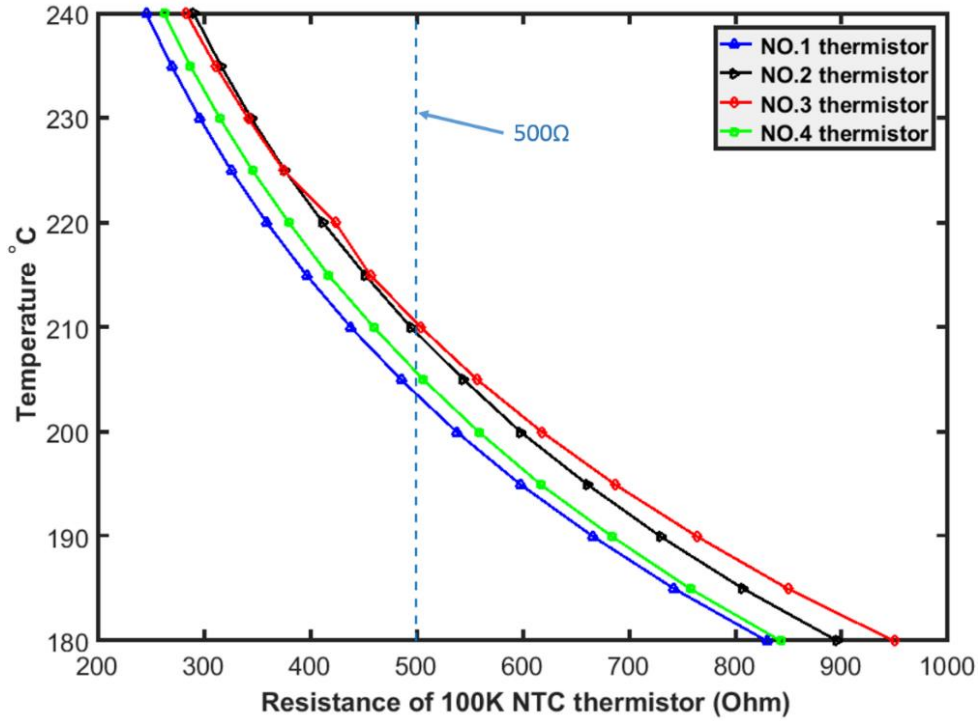


Figure 3-27 Temperature versus resistance curves of four thermistors that labeled with the same value of β .

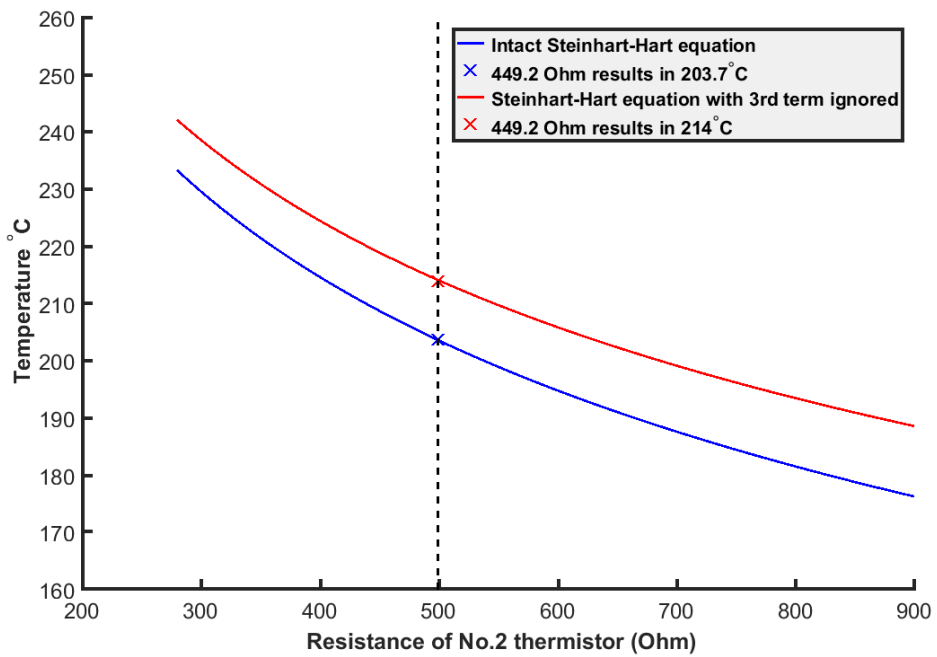


Figure 3-28 Performance of Steinhart-Hart equation on Arduino Uno and Arduino Due

The Steinhart-Hart equation (cf. *Equation 3-12*) can predict temperature more accurately than the Beta equation [86] in *Equation 3-13*. However, most datasheets in the literature are based on the Beta equation. To examine the error between these two equations, calculated temperature using both equations is shown in *Figure 3-29*. The computed results show that the Beta equation yields a higher calculated temperature as compared to the Steinhart-Hart equation for temperatures above 195°C. For example, the difference between the two results is approximately 3°C at 220°C, which is high enough to degrade the accuracy of filament flow property evaluation in this research.

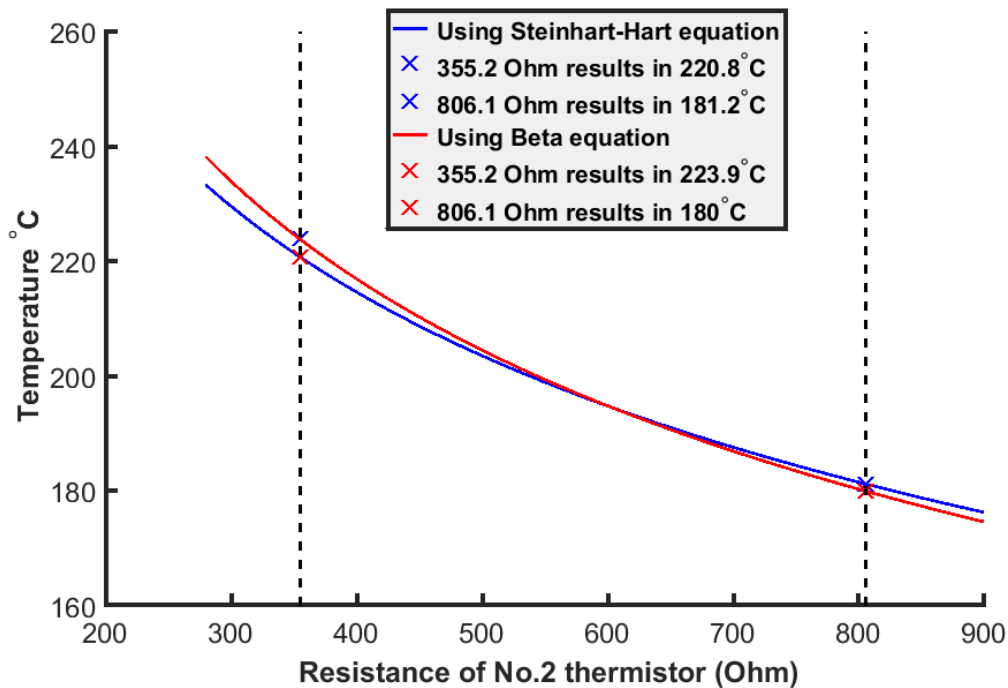


Figure 3-29 Comparison of temperature calculation using Steinhart-Hart and Beta equation

3.3.2 Thermocouple

Unlike a thermistor which has limited performance at high temperatures, a thermocouple has the benefit of covering a wider range of temperature sensing as shown

in *Figure 3-21*. K-type thermocouples are the most widely used thermocouple for desktop 3D printers since they are inexpensive, accurate, and reliable. For these reasons, we use K-type thermocouples in our filament rheometer. A thermocouple consists of two dissimilar metallic wires made, where Nickel-Chromium or Nickel-Aluminum are common for a K-type thermocouple. The wires are joined together within a welded bead at one end, which is called the measurement “hot” junction. The junction at the ends of the wires opposite hot junction are connected to circuitry and often referred to as the reference “cold” junction (cf. *Figure 3-30*). A continuous current flows through the circuit, voltage correspondingly generated on thermocouple is measured and converted to temperature. Note that thermocouples are not a sensor that directly measures the absolute temperature, but instead measures the difference between temperature at the hot junction and reference junction. Additional information on the working principles of a thermocouple, including the Seebeck effect, Peltier effect, and Thomson effect may be found in [87] and [88].

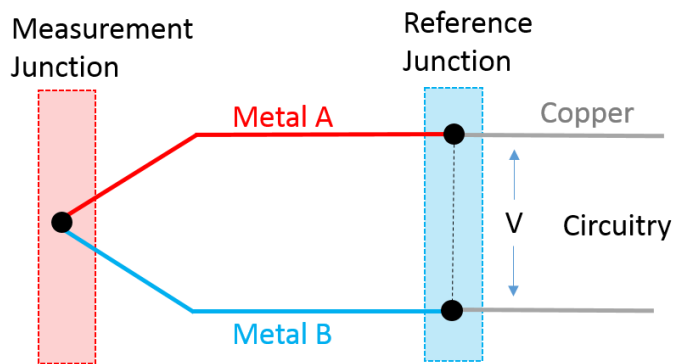


Figure 3-30 Configuration of thermocouple

In the K-type thermocouple, the output voltage increases from 0 mV to 20 mV for temperature from 0°C to 500°C, giving a sensitivity of approximately 41 $\mu\text{V}/^\circ\text{C}$ [89].

Since voltage changes are minimal, an amplifier is required to measure voltage and convert it to temperature accurately. The MAX31855 (Adafruit, New York City) appearing in *Figure 3-31* is an integrated circuit board used in this project which reads and amplifies the voltage and provides a built-in reference junction compensation. It has a temperature output with 0.25°C resolution.

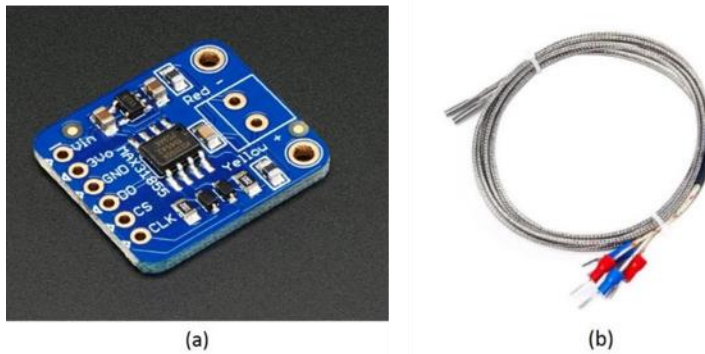


Figure 3-31 (a) MAX31855; (b) K-type thermocouple with 3mm diameter and 15mm length

3.3.3 Comparison of Temperature Sensors

As mentioned above, the distances of the thermistor and the thermocouple to the nozzle screw are the same in our filament rheometer (cf. *Figure. 3-16*). Furthermore, high-temperature resistant cotton is wrapped around the heater block to reduce heat dissipation from the external surfaces, providing a nearly uniform temperature within the hot end. To verify temperature uniformity and to check the accuracy of the temperature measurement, an experiment was performed with the temperature of the heater block was set to 6 different temperature values (i.e., 180°C to 230°C with 10°C increment). The recorded temperature differences between the thermistor and the thermocouple from our device are listed in *Table 3-4*. The maximum measured temperature difference is shown

to 0.9°C at a setpoint of 180°C. The average percentage error between measured thermistor and thermocouple temperatures is 0.368% which demonstrates the accuracy of temperature performance throughout this project.

Table 3-4 Temperature readings from thermistor and thermocouple

Temperature sensors	180°C	190°C	200°C	210°C	220°C	230°C
100K NTC thermistor	180.4	190.2	200.1	210.1	220.1	230.1
K-type thermocouple	181.3	191.0	200.9	210.8	220.8	230.9

3.4 Temperature Control

In addition to temperature accuracy discussed above, the stability of temperature control is also of interest since it is a critical factor that affects the extrusion flow rate. An appropriate temperature feedback control algorithm is required to fulfill this purpose.

Generally, feedback loops contain three components including the object to be controlled, sensors to measure the output of the object, and a controller to produce an input from the object [90]. In our device, the output from sensor serves as the input to the controller and the output of controller acts as input to the object as shown in *Figure 3-32*. Firstly, the setpoint or the anticipated result is defined in the controller as the reference value.

Secondly, the sensor measures the process variable (i.e., temperature) and generates feedback signals to controller as the input. Finally, the controller computes the difference between setpoint and input values for generating and transmitting the output into the object to control its performance. Overall, the combination of sensing, computation, and actuation together control the extrusion temperature to maintain steady state.

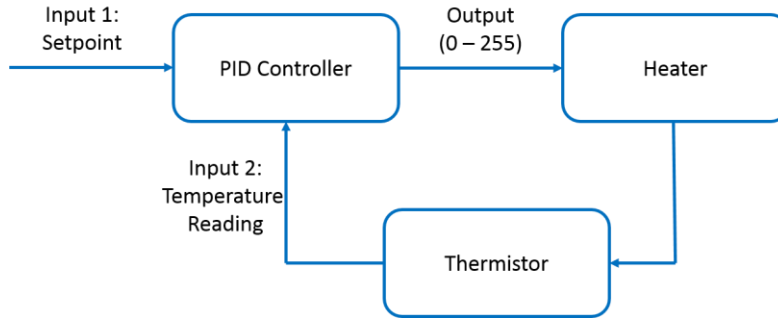


Figure 3-32 Temperature feedback control loop

Proportional-Integral-Derivative (PID) control, one of the most widely used control algorithm, is applied to control the extrusion temperature in this project. A PID controller calculates the error as the difference between measurement and setpoint, then attempts to minimize the error by adjusting the process. There are three coefficients of the error terms in a PID controller that include the following: proportional, integral, and derivative, which are typically constant when the system under specific testing condition. The output of a PID controller acting over time from 0 to t may be written as the sum of these three terms as

$$u(t) = k_p e(t) + k_i \int_0^t e(t) dt + k_d \frac{de(t)}{dt} \quad (3.14)$$

where k_p , k_i , and k_d are the constants (the subscript of each terms are acronyms of pproportional, integral, and derivative), $e(t)$ is the real time error between measured value and desired value, $u(t)$ is the output of PID controller.

The proportional term in *Equation 3.14* depends on the present error, the integral term depends on the accumulation of past error, and the derivative part is determined by the prediction of future error. As expressed in $k_p e(t)$, the proportional response is adjusted by multiplying the error by a constant k_p , called the proportional gain constant.

The value of k_p has influence on the response speed of the control system to the error signal. If k_p is too high, the output will have a drastic change to input error, thus, the process variable will begin to oscillate. On the contrary, a small proportional gain can result in inefficient control action due with minimal influence on the output. The integral response is proportional to both the value of the error and its duration. Thus the integral response will continually increase or decrease the output over time to reduce the error. If the error is large, the effect of this term will be fast. In contrast, changes will be slower when the error is small. Derivative control is determined by the rate of change of error. It can increase the stability of the system, reduce the overshoot, and improve the transient response by slowing down the rate of change of output [91].

Our PID control algorithm is implemented on the Arduino by using the program bu Beauregard [92]. A Pulse Width Modulation (PWM) control is applied to convert the analog control signal from PID into a digital switching signal. The system consists of the power supply, heater, resistors, diode, the IRFP150 NPN MOSFET as shown in *Figure 3-15*.

PWM is a terminology used to describe a type of digital signal applied to modulate an analog value [93]. Digital control is often used to create a square wave, where a signal switches between on and off. In a typical square wave, the frequency of each pulse is fixed. However, pulse frequency varies with time in PWM signal as shown in *Figure 3-33*. The percentage of the signal which is high over an interval of time is known as the duty cycle, which can be presented as the pulse width. Thus, by changing the duty cycle or pulse width (pulse frequency), the output signal can be changed over time. In other words, the on-off pattern can simulate voltages in between full on (5 Volts)

and off (0 Volts) in an Arduino board. Calling the `analogWrite()` function in the Arduino IDE provides the PWM signal that is on a scale of 0 – 255. This signal is transmitted to MOSFET to switch the access from the controller to switch the emitter on and off (cf. *Figure 3-12*) for altering the amount of power supplied to the resistive heater, thus controlling the extrusion temperature.

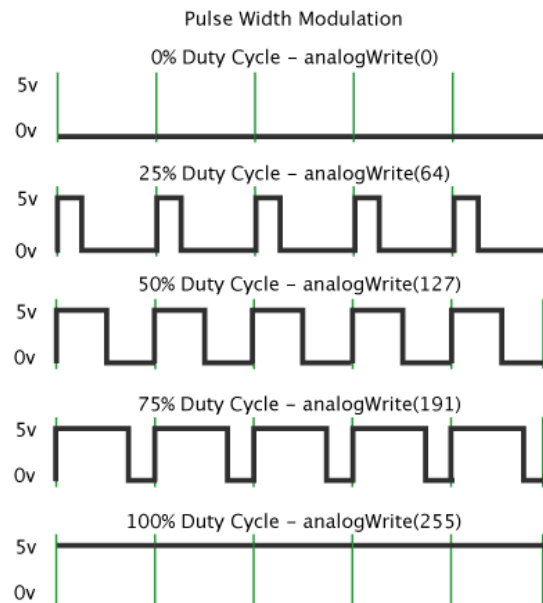


Figure 3-33 Pulse Width Modulation signal [94]

The PID controller is activated in a for-loop in the Arduino IDE in our filament rheometer. The duration of each loop determines how fast the control can be maintained. In this project, the sampling rate (i.e., the for-loop frequency) is defined as 10 HZ which is determined from factors such as the sample rate of load cell reading, filter selection, and the ADS1115 reading frequency, as described in the next section. The heater maintained at various temperatures from 180°C to 220°C with 10°C increments lasting for 10 minutes to test the performance of PID controller. The temperature was found to have small fluctuations within $\pm 0.5^\circ\text{C}$ as shown in *Figure 3-34* which is taken from a

sample measurement. Therefore, we conclude that a 10 HZ controlling frequency is sufficient for our purpose.

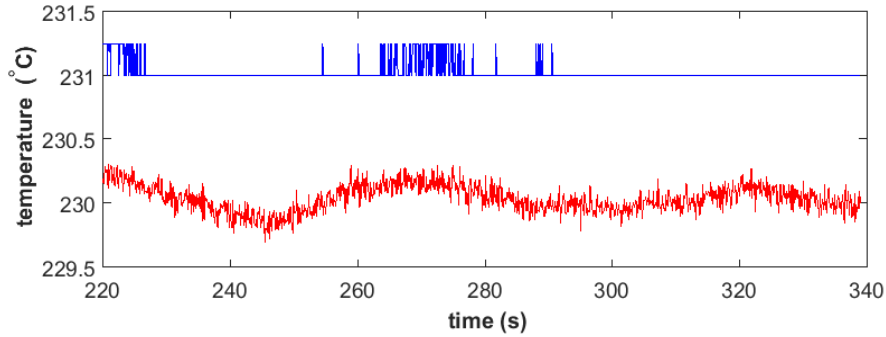


Figure 3-34: Typical temperature fluctuation during temperature control experiment showing values within $\pm 0.3^{\circ}\text{C}$

In addition, the response time of the temperature sensor also affects the control quality. As mentioned at the beginning of this chapter, the thermistor is used as the primary temperature sensor in our PID control circuit. The reason is illustrated in *Figure 3-35*, where the response time of thermocouple is measured which has 5.5 s delay as compared to the reading from thermistor.

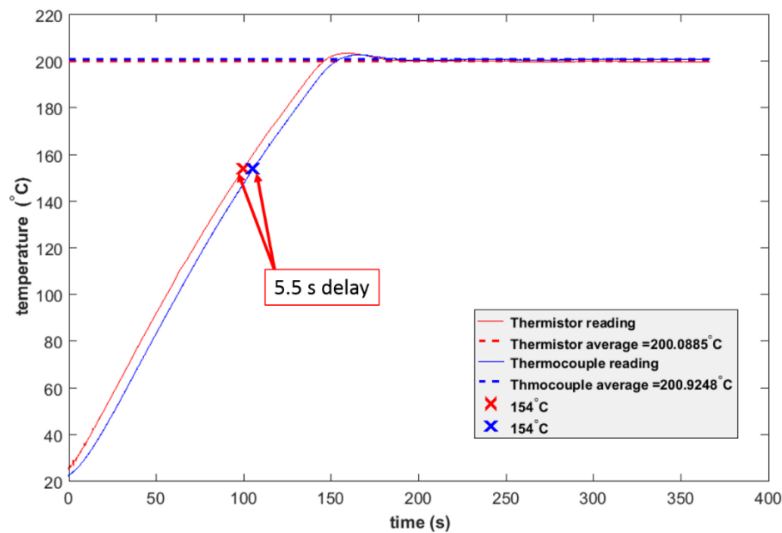


Figure 3-35 Response speeds of thermistor and thermocouple

3.5 Force Signal Processing

Given the temperature control methods described above, we consider that the filament melt flow in the nozzle can be regarded as being at near steady state with respect to temperature and flow rate. Unfortunately, the load signal as measured that is shown in *Figure 3-36* exhibits too much variation to be useful as a filament rheometer. Therefore, the load cell output signal is analyzed here gain a better understanding of fluctuations in the signal. This section considers the analysis of the force transducer output, including a discussion of the force signal, the noise sources, and different filters used in Arduino.

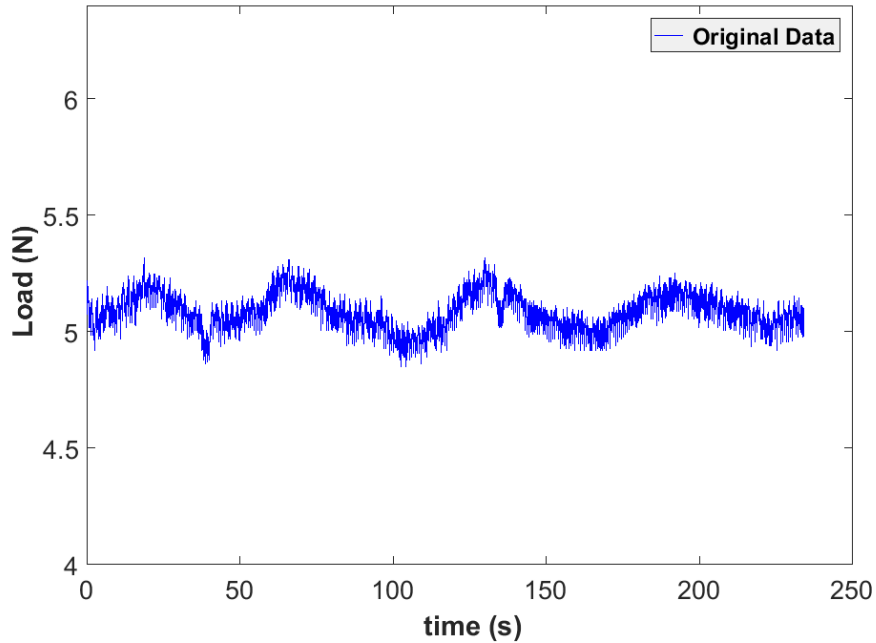


Figure 3-36: Original load cell data of ABS under 210°C & 1RPM

3.5.1 Fourier Analysis – Fast Fourier Transform

Fourier analysis is a technique used to evaluate signals with respect to frequency, which is performed by applying a Fourier transform to convert the signal from time domain to frequency domain. The analysis in the time domain shows how a signal

changes over time, while frequency-domain analysis reveals information underlying the signal such as frequency content and signal's energy.

Understanding Fourier series is the first step for analyzing the frequency content of a signal. A waveform can be considered as the sum of a series of sinusoidal functions, each having a different frequency, amplitude, and phase. Fourier's theorem states that any arbitrary periodic function can be decomposed into an infinite series of sinusoids [95] as

$$f(t) = a_0 + \sum_{k=1}^{\infty} [a_k \cos(k\omega_0 t) + b_k \sin(k\omega_0 t)] \quad (3.15)$$

where ω_0 is the angular velocity. The Fourier coefficients a_0 , a_k and b_k , ($k = 1, \dots, \infty$) can be determined by evaluating the following integral equations:

$$a_0 = \frac{1}{T} \int_0^T f(t) dt \quad (3.16)$$

$$a_k = \frac{2}{T} \int_0^T f(t) \cos(k\omega_0 t) dt \quad (3.17)$$

$$b_k = \frac{2}{T} \int_0^T f(t) \sin(k\omega_0 t) dt \quad (3.18)$$

where $T = \frac{2\pi}{\omega_0}$ is the period. Euler's formula

$$e^{i\theta} = \cos \theta \pm i \sin \theta \quad (3.19)$$

written regarding the imaginary unit $i = \sqrt{-1}$ is employed to write the Fourier series in terms of complex notation more concisely [95] as

$$f(t) = \sum_{k=-\infty}^{\infty} c_k e^{ik\omega_0 t} \quad (3.20)$$

$$c_k = \frac{1}{T} \int_{-T/2}^{T/2} f(t) e^{-ik\omega_0 t} dt \quad (3.21)$$

Unfortunately, Fourier series is unable to analyze the non-periodic signal, such as the force output signal appearing in *Figure 3-36*. To apply Fourier's method to an aperiodic function, we assume that the period T in *Equation 3.21* to be infinite, such that the signal function never repeats, as in

$$f(t) = \frac{1}{2\pi} \int_{-\infty}^{\infty} \left[\int_{-\infty}^{\infty} f(\tau) e^{-i\omega\tau} d\tau \right] e^{i\omega t} d\omega \quad (3.22)$$

The coefficients change to a continuous function of ω as in *Equation 3.22*, which is called the Fourier integral of the signal function $f(t)$. The complex form is written as

$$F(\omega) = \int_{-\infty}^{\infty} f(t) e^{-i\omega t} dt \quad (3.23)$$

where $F(\omega)$ is called the Fourier transform of $f(t)$. Since angular velocity is a variable of frequency, it is clearly demonstrated that Fourier transform could be used to transform between time and frequency domain for non-periodic signal functions.

Signals can be classified by continuous-time and discrete-time signal. *Equation 3.23* defines the Fourier transform of a continuous-time signal $f(t)$. However, in this project, the force signal is collected at discrete points in time yielding a finite set of values. Thus, the discrete-time Fourier transform has to be applied to solve the practical problem. By replacing the integral in *Equation 3.23* with the desired summation, the discrete Fourier Transform (DFT) and the inverse DFT are given respectively as [95]

$$F_k = \sum_{j=0}^{n-1} f_j e^{-ik\omega j} \quad \text{for } k = 0 \text{ to } n - 1 \quad (3.24)$$

$$f_j = \frac{1}{n} \sum_{k=0}^{n-1} F_k e^{ik\omega j} \quad \text{for } j = 0 \text{ to } n - 1 \quad (3.25)$$

where $\omega = 2\pi/n$ and n represents the intervals of samples.

The discrete Fourier transform is a mathematical operation. However, it is computationally onerous due to the n^2 operations that are required to evaluate *Equations 3.24 and 3.25* [95]. If the signal contains an enormous amount of data samples, the direct computation of DFT can be expensive. An alternative approach, the Fast Fourier Transform (FFT), is an efficient algorithm for the evaluation of discrete Fourier transform operation. FFT appears in different forms in digital signal processing (DSP) hardware and software [96].

To apply the MATLAB FFT function, data samples must be equally spaced, for the function `fft()` to decompose the signal into frequency domain. As mentioned in *Section 3.2.2 and 3.4*, factors such as load cell sampling rate, floating point calculation of temperature, and other commands like `Serial.print()` should be taken into account to calculate the loop time in the main Arduino IDE code. However, since all of the electronic components used in our device are all inexpensive and of low quality comparing to the ones used on the commercial measuring apparatus, the sampling rate tends to fluctuate slightly during processing as shown in *Figure 3-37 (a)*.

To address the issue of sampling rate, an adjustment is made in the main Arduino IDE code to confine the data output with same time interval by setting the duration of each loop to be a constant. This constant time is longer than any of the sample interval as in *Figure 3-37 (a)*. Therefore, each loop will be held until the actual loop time is equal to

the preset constant time. The improved result is shown in *Figure 3-37 (b)*, where the sampling rate is defined fixed as 10 HZ.

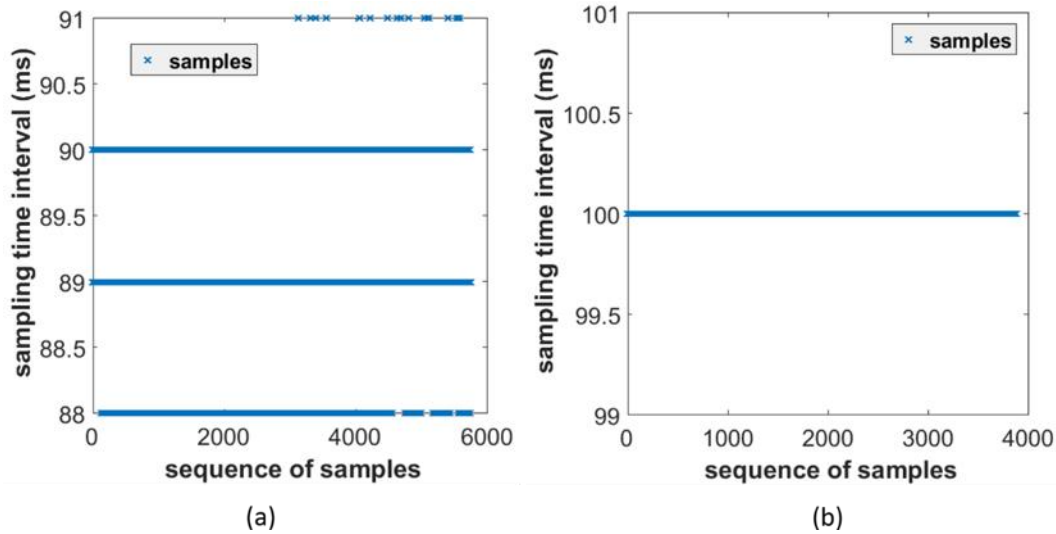


Figure 3-37 (a) Original sampling rate is not a constant; (b) The sampling rate is controlled to be constant

The Fourier transform separates the signal into complex exponentials rather than sinusoids as shown in *Equations 3.24* and *3.25*. The signal contains two equal-amplitude complex exponentials when converted it to the sinusoidal form (Euler's formula) yields a real part that cancels the imaginary part of the result. Hence, the frequency spectrum of the signal is two-sided as shown in *Figure 3-38*.

The first half frequencies are positive frequencies; the other side contains the negative frequencies. The frequency falls in the midpoint is called the Nyquist frequency which is the highest frequency that can be measured in a signal. Since the negative frequencies are meaningless but have the same magnitude as the positive ones, *Figure 3-39* illustrates the one-sided plot of signal in frequency domain which contains all frequencies from low to high. The magnitude of calculation of MATLAB `fft()`

corresponds to the amplitude of the sinusoid at that frequency. In *Figure 3-39*, the magnitude of the signal at each frequency is normalized to the scale of one to make it easier to compare the intensity of each frequency components.

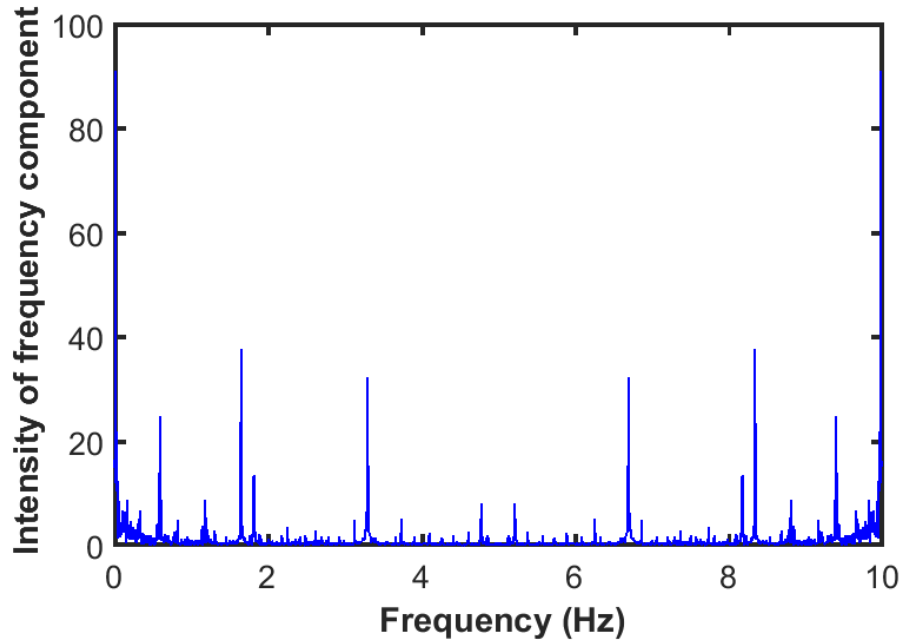


Figure 3-38 Two-sided frequency spectrum of force signal (ABS at 210°C & 1RPM)

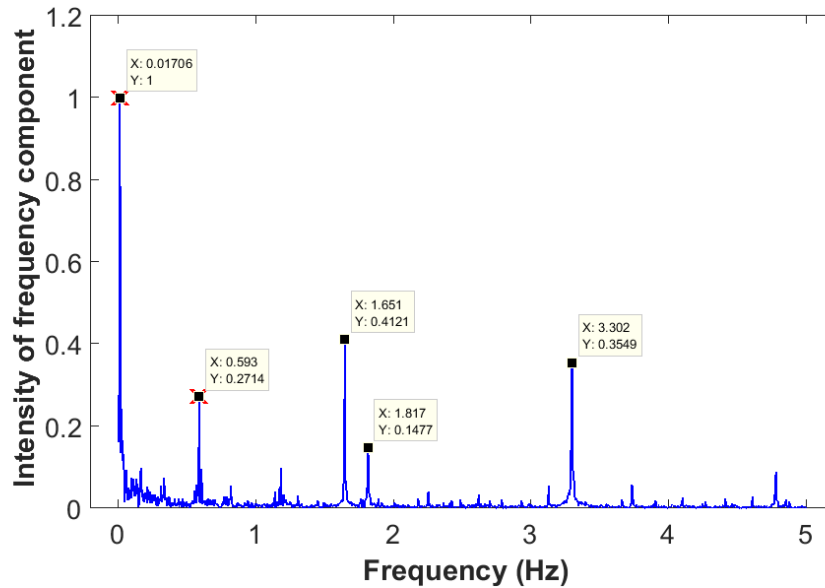


Figure 3-39 One-sided frequency spectrum of the force signal (ABS at 210°C & 1 RPM)

Figure 3-39 lists values of frequencies that are dominant in the signal. It is noticed that there is a frequency bin at 0.01706 Hz which is close to the 1 RPM = 0.0167 Hz rotational frequency of the drive gear. In *Figure 3-36*, the peaks of the wave roughly repeat with the period of 1 minute. Combining the analyses of signal in both time and frequency domain, one can infer that either the idler pulley or the drive gear is not perfectly round, such that the pushing force added on the filament is changing over time. In addition, the frequency when each tooth on drive gear is coming into contact with the filament can also be found in the spectrum. The drive gear has 36 teeth on its surface, such that the frequency of tooth contact is 0.6 HZ. And one can find there is a frequency content among the dominant frequencies at 0.593 Hz. Therefore, the FFT analysis is a useful tool to help researchers to find the apparent factors that cause the fluctuation of the signal, and also give an overview of the noise frequency band.

3.5.2 Filters in Arduino

As shown above, the FFT method can be used as the signal post-processing tool. To realize the benefit, filters are added to reduce the noise when the experiments are in process. Thus the high-frequency noise can be eliminated in real time.

Based on the signal curve in the time domain, there several digital filters that are available for this purpose that include a low pass filter, median filter, and simple running average filter. The purpose of using these filters is to smooth short-term fluctuation in the output signal. In our device, all digital filter algorithms are implemented in Arduino using the Arduino Library directly.

The low pass filter, as the name suggests, is a filter that passes signals with low frequency (lower than the cutoff frequency) and blocks signals with high frequency [97].

A filter's response to different frequencies is characterized as pass-band, transition-band, and stop-band. The pass-band are the region of interest because it contains the signal that passes through and is mostly unchanged. The signal falls in the transition region, and stop-band is highly attenuated but not removed entirely.

The simple running average filter operates by calculating the average value of a series of input data as a single value then output as the signal data. This strategy can also filter out the higher frequency components. The choice of the amount of input data used to average determines the lag time to the latest data point. If this lag time is too large, the filtered signal will not be usable, since it will lose important information. If the lag amount is too small, the filter can be inefficient to filter out sudden changes in signal.

The median filter is a nonlinear filter that can eliminate spikes of signals. The median is defined as the middle value of an array of sorted values. The input data is stored in the buffer and sorted. Then the median of the set of data is output and displayed, the same way as simple running average dose. The advantage of this filter comparing to running average is that it is not influenced by the outliers, such that it can represent a real measurement.

Figure 3-40 illustrates the performance of three filters. In this project, the load cell reading is represented by calculating the average value of the period of the signal of interest. And the comparison of the average values of signals modified by different filters are listed in *Table 3-5*. The results indicate that simply applying the average strategy to find the extrusion loading is a reasonable solution for our research.

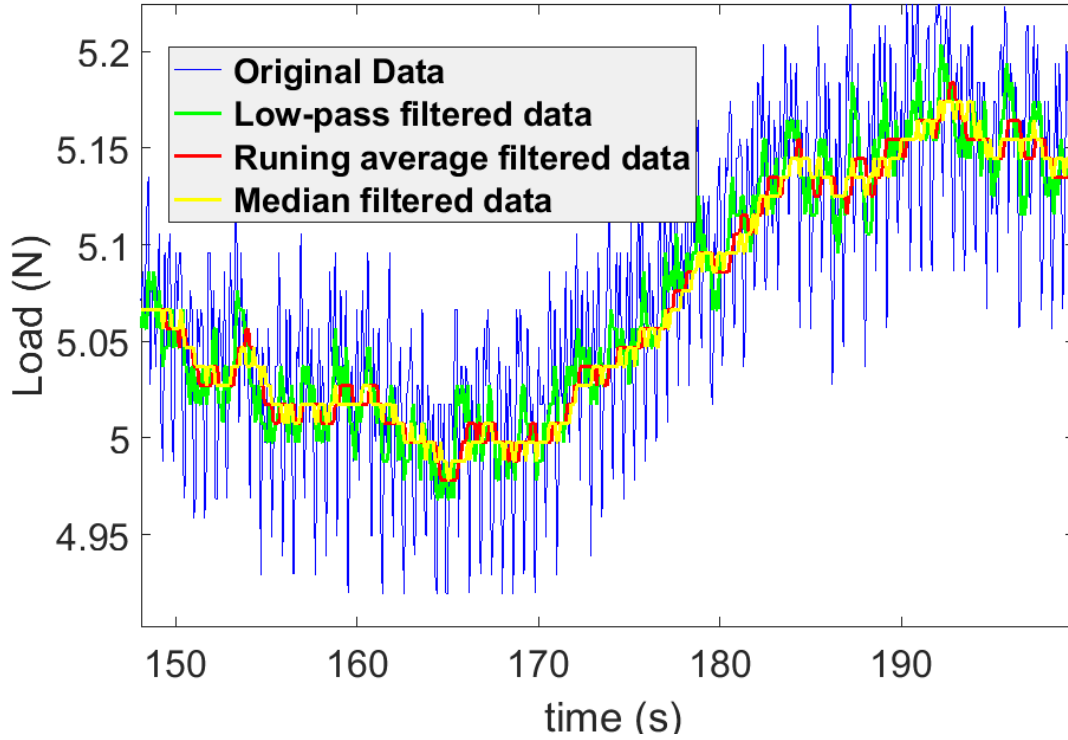


Figure 3-40 Comparison of performance of Low-pass Filter, Simple Running Average filter, and Median Filter

Table 3-5 Average values of the original and filtered force signal data

Signals	Average Value (N)
Original Signal	5.0874
Low-Pass Filter	5.0828
Simple running average filter	5.0827
Median filter	5.0836

3.6 Summary

In this chapter, each component in the proposed filament rheometer device has been discussed from the perspectives of their function, selection, and performance. The most important factors with respect to the measurement of pressure drop such as temperature, filament feeding velocity, tightness of the spring extruder are carefully

measured and controlled. Therefore, the errors of pressure drop measurement due to those factors are minimized. Finally, the specification of the device is given in *Table 3-6*, which is essential as the reference for designing the experiments in the next chapter.

Table 3-6 Specification of the device

Specification	Value
Sampling Frequency	10 HZ
Temperature Accuracy	$\pm 0.7^{\circ}\text{C}$
Temperature Resolution	0.1 $^{\circ}\text{C}$
Stepper motor running speed range	0.5 – 8 RPM

CHAPTER FOUR

Experimental Methods

This chapter describes procedures and methods used for exploring the properties of melted filament material in an FFF nozzle as part of the experimental phase of this research. The six materials considered in this research are two brands of ABS, carbon fiber reinforced ABS, PLA, carbon fiber reinforced PLA, and amphora which are given in *Table 4-1*. Each of these are employed in experiments that obtain pressure drop by measuring the force during extrusion using our low-cost FFF filament rheometer device. Firstly, the thermal properties of these polymers or polymer composites are examined by using Thermogravimetric Analysis (TGA) and differential scanning calorimetry (DSC). The measured thermal properties are used to specify processing temperatures as well as to predict the melting region for our filament rheometer experiments. Then, the force required to extrude the molten material through the nozzle in our filament rheometer is measured to determine polymer melt properties. The rheology properties of these materials are measured in the HAAKE MARS 40 (Thermo Fisher Scientific, Waltham, MA) rotational rheometer.

Table 4-1 Filaments of polymer and polymer composite used in this project

Filaments	Manufacturer	Density (g/cm ³)	Diameter (mm)	Carbon Fiber Content (%)
ABS	3DXTECH (Byron Center, MI)	1.18	1.75	N/A
CFR-ABS	3DXTECH (Byron Center, MI)	1.11	1.75	< 20
ABS	Triptech Plastic (Youngstown, OH)	N/A	1.75	N/A
Amphora	Triptech Plastic (Youngstown, OH)	N/A	1.75	N/A
PLA	3DXTECH (Byron Center, MI)	1.24	1.75	N/A
CFR-PLA	MatterHackers (Foothill Ranch CA)	N/A	1.75	N/A

4.1 Thermal Properties of the Materials

Thermal analysis investigates the effect of temperature on the physical properties of materials. Thermal decomposition temperature, melting point, and glass transition temperature are of particular importance for polymer materials. The thermal decomposition temperature can be used to determine the maximum allowable temperatures used in MARS 40 rheometer, avoiding decomposition of the polymer. Measuring the glass transition temperature and melting points of materials is helpful for our research when adjusting the cooling system on liquefier for controlling the melting zone. The content of carbon fibers can also be measured by performing the TGA test. This information will be used to assess fiber concentration and to determine if the Cox-Merz Rule is valid for these filled materials. All polymer and polymer composite samples in this research are dried in an oven for at least for 24 hours at the appropriate temperatures before conducting any measurement.

4.1.1 Thermal Decomposition

The Q50 (TA Instruments, New Castle, DE), a TGA instrument, is used to measure the thermal degradation behavior. TGA measures how the weight/mass of a sample changes over an interval of increasing temperature which helps determine the thermal decomposition temperature of a material [98]. Before conducting the tests, several factors that affect the measurements are identified. The ramp-heating method is applied for measuring the thermal decomposition temperature in which the sample was heated from around 20°C to 600°C with varying heating rate (10°C/min and 20°C/min) in a nitrogen atmosphere.

Sample mass and heating rate are two experimental parameters that affect TGA measurements and must be controlled to ensure an accurate result. The recommended sample size for the Q50 is a mass between 3mg and 15mg. To inspect the effects from sample size for greater accuracy of measurements, the samples of ABS were cut into two groups of small pieces, and each group had three specimens having a mass 5mg, 8mg, and 10mg respectively. The experiments are conducted for the two groups samples at two different heating rates (i.e., at 10°C/min and 20°C/min). The results of these measurements appear in *Figure 4-1*. It can be seen that the effect of sample size on thermal decomposition temperature measurement can be ignored since the temperature of all masses at either 10°C/min or 20°C/min shows a temperature deviation of only 1°C to 2°C deviation. The effect of heat-ramp rates is considered in *Figure 4-2 and 4-3*. It is evident that the heating rate has a significant effect on decomposition temperatures for the same material. These results show that heating rate increases the measured decomposition temperature.

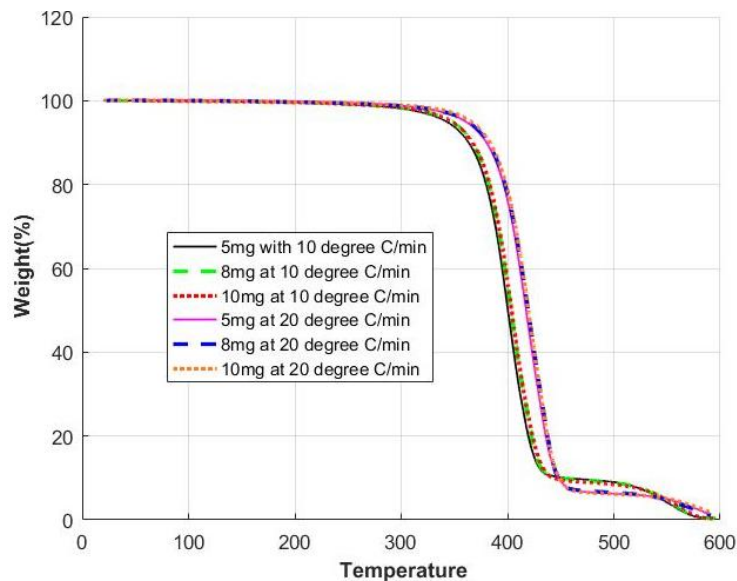


Figure 4-1 TGA curves of ABS (Two-group tests with three different sample size)

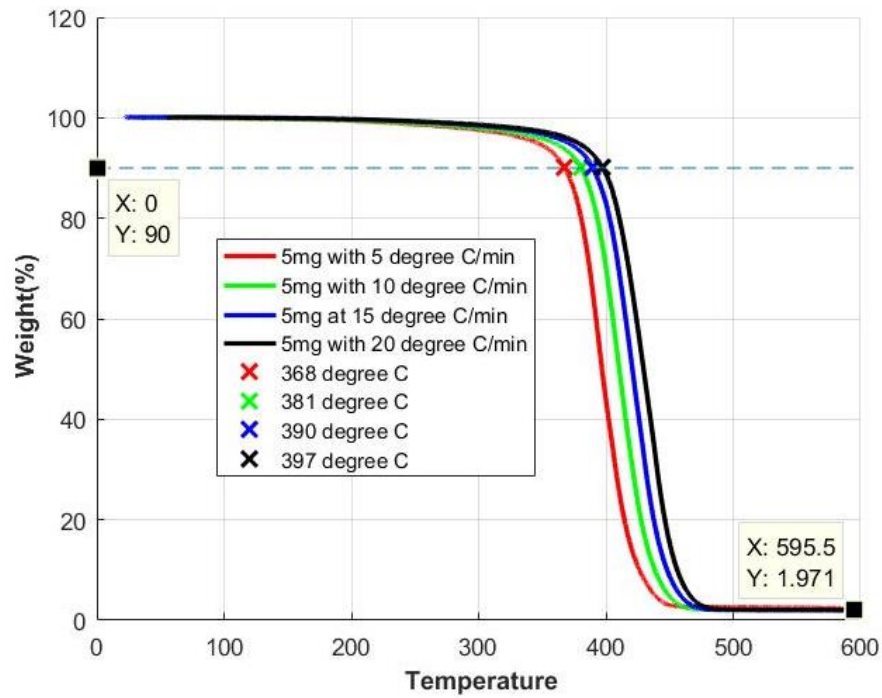


Figure 4-2 Percent weight versus temperature of 5mg samples at varying heating rates

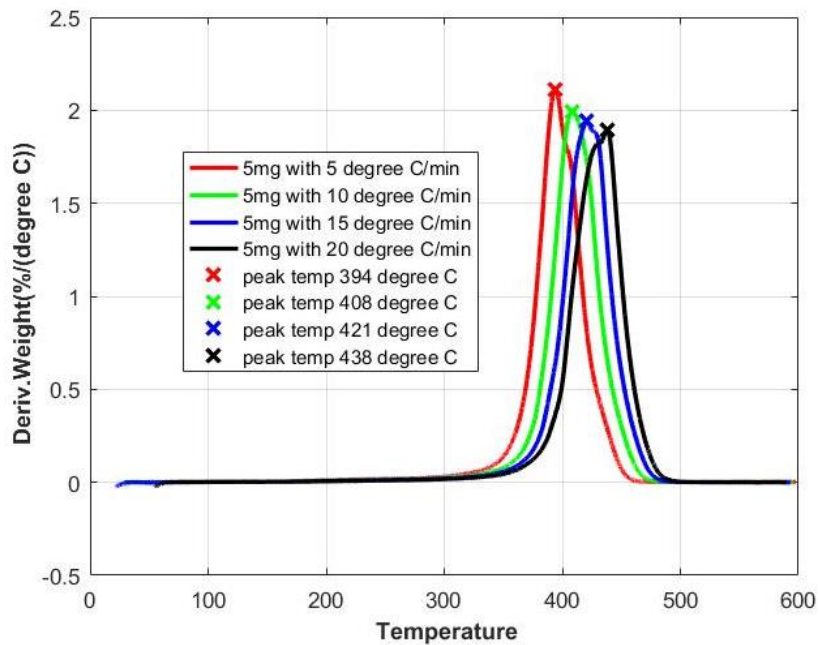


Figure 4-3 Derivative weight with temperature of 5mg samples at varying heat rates

Data given by NETZSCH Analyzing & Testing [99], the recommended heating rate to measure the degradation temperature is between 10°C/min and 15°C/min. Based on this, a heating rate 15°C/min is chosen for testing performed in this thesis. All material samples used in the experiments here are cut into small pieces which have the mass between 5mg to 12mg, and results appear in *Figure 4-4 and 4-5*. Based on previous analyses, the thermal decomposition temperature is given as a range rather than a certain value in *Table 4-2*, where the starting number represents the temperature when the materials start decomposing, and the ending number represents the temperature when the materials' decomposing rates get the maximum values.

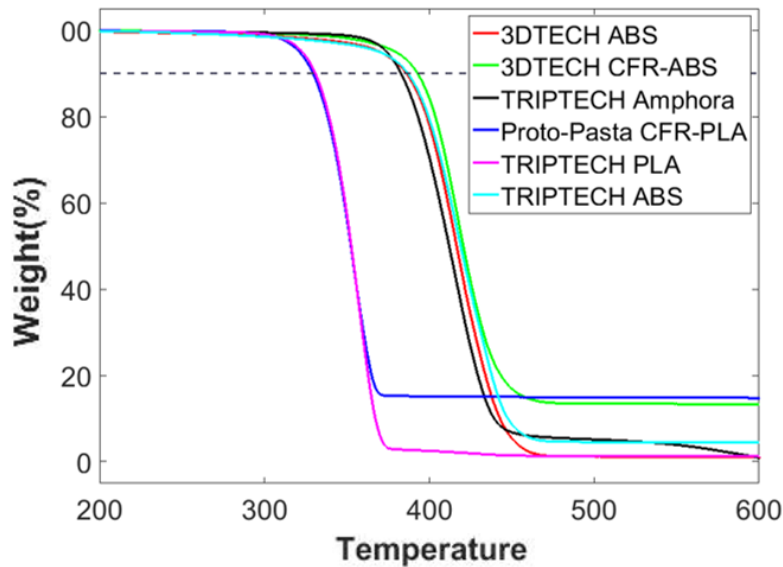


Figure 4-4 TGA weight-temperature curves of six materials

The carbon fiber contents in ABS (3DXTECH) and PLA (MatterHackers) is directly obtained by measuring the mass of ash left in the pin or by simply multiplying the percentage of leftover by the total mass of the sample, as shown in *Table 4-2*. We note that the TRIPTECH ABS filament had 4.5% residual left over after the burn-off

experiment. Since the manufacturer claimed that there have no fibers in this filament, thus the residue could be the un-fully decomposed acrylonitrile, butadiene, or styrene.

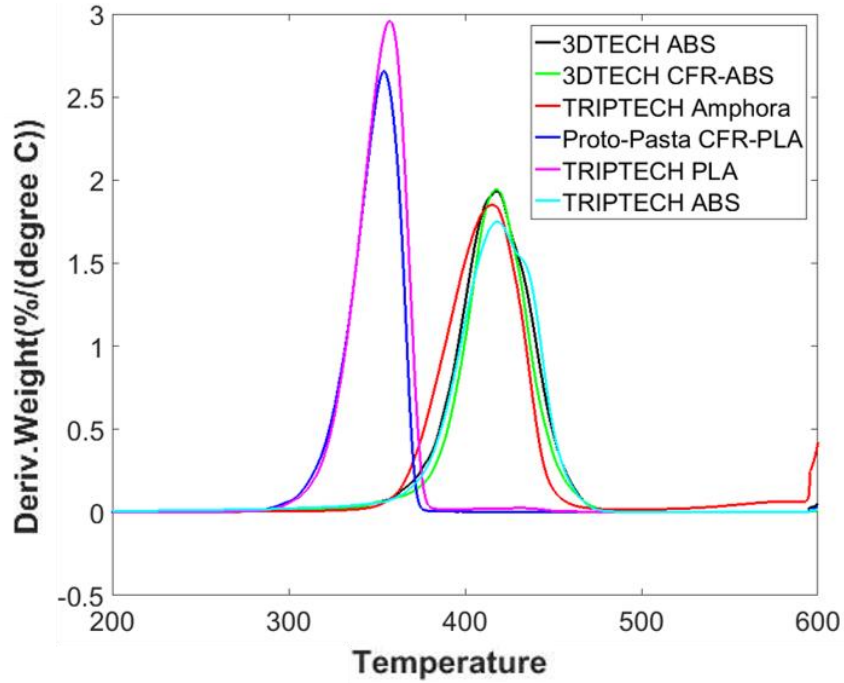


Figure 4-5 TGA Derivative weight with temperature curves of six materials

Table 4-2 Thermal decomposition & Carbon fiber content

Material	3DXTECH ABS	3DXTECH CFR-ABS	TRIPTECH ABS	TRIPTECH Amphora	TRIPTECH PLA	MatterHackers CFR-PLA
Thermal Decomp osition	386°C ~ 418°C	393°C ~ 418°C	387°C ~ 418°C	383°C ~ 415°C	331°C ~ 357°C	330°C ~ 354°C
Carbon Fiber Content	N/A	13.39%	N/A	N/A	N/A	14.82%

4.1.2 Glass Transition and Melting Temperature

In addition to the thermal decomposition temperature, other parameters such as glass transition temperature and melting point are measured using Q20 (TA instruments)

DSC. The DSC measures the amount of heat required to increase the temperature of a sample and outputs the data as a function of temperature. Data from the DSC can be used to evaluate the glass transition and specific heat capacities of polymers [100]. In the experiment, the samples are analyzed using the heating/cooling/heating method. The sample is heated from -90°C to 250°C at a temperature rate of increase of $3^{\circ}\text{C}/\text{min}$, which is followed by cooling at the same temperature rate of change to -90°C . The sample is then re-heated with the same heating rate as before. The heat flow into the sample is determined by taking the difference between a reference sensor and the sample sensor. The resulting energy could have a value that is positive or negative. In a DSC analysis, the glass transition can be identified as the point on the heat flow versus temperature curve that exhibits a vertical shift. *Figure 4-6* is the original curve output from TA Universal Analysis software which shows three heating and cooling cycles for 3DXTECH ABS. The first cycle, which involves heating, gives the properties of the material in its as-molded condition. This step removes prior thermal history and provides the properties of interest for the material. It is typical to select the second heat cycle for a given experiment to further analyze for properties of the polymer melt. Notice that the same sample undergoes the same ramping-heating input, but the re-heating cycle needs less heat than the original heating cycle. The difference is expected to be due to crystallization that occurs during a previous cooling phase.

In a manner similar to that performed in our TGA testing, the influence of the sample size and heating speed on the measurements are examined by conducting three tests using 3DXTECH ABS. The experimental procedure is as follows:

1. Dry sample with 5 mg mass undergoes $5^{\circ}\text{C}/\text{min}$ HCH (heat/cool/heat).

2. Dry sample with 10 mg mass undergoes 5°C/min HCH (heat/cool/heat).
3. Dry sample with 10 mg mass undergoes 10°C/min HCH (heat/cool/heat).

A typical test result appears in *Figure 4-7* which illustrates that sample size and heating rate have little effect on the temperature measurement in the DSC.

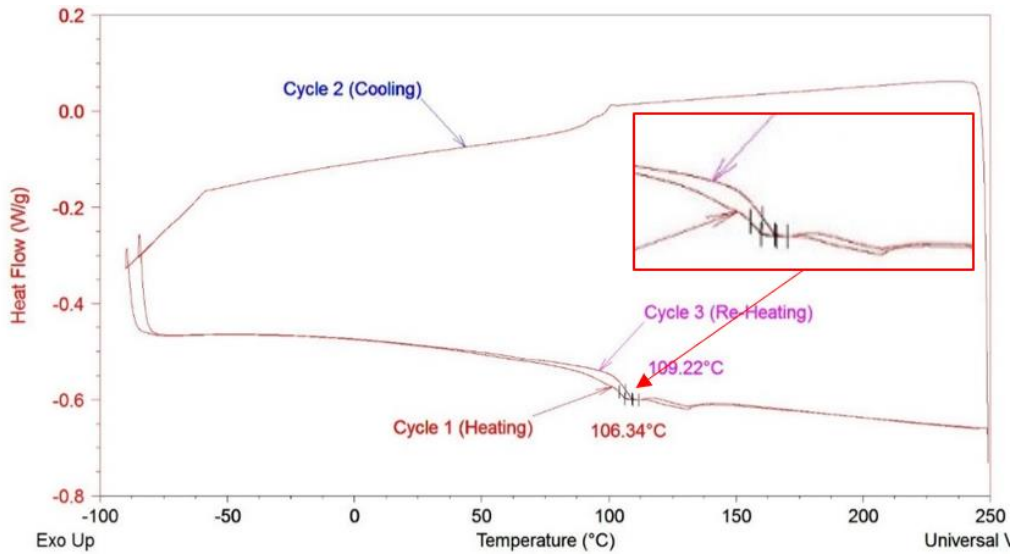


Figure 4-6 DSC results of the 10mg sample heated/cooled by 10°C/min (ABS)

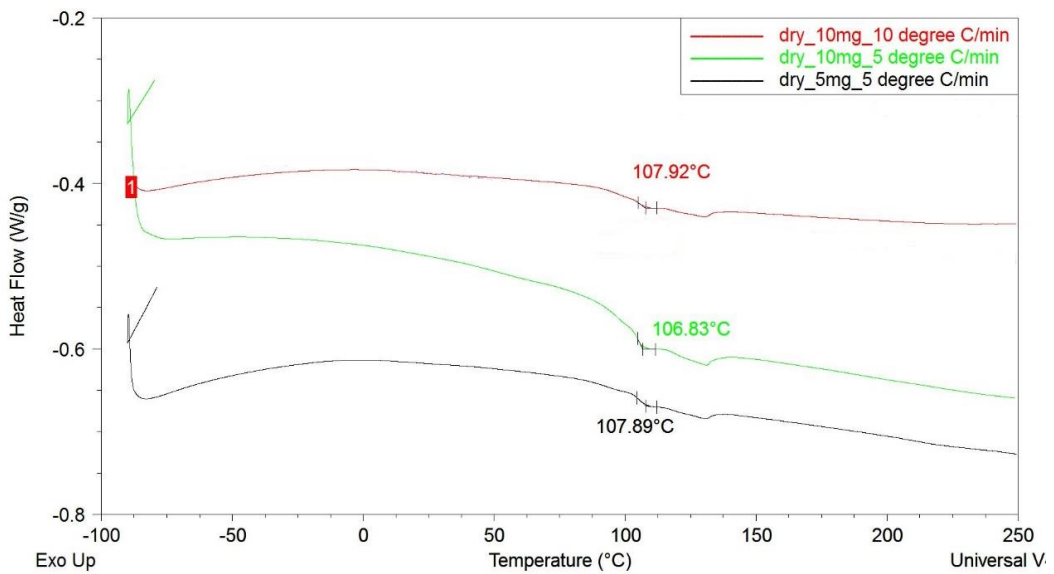


Figure 4-7 Glass transition temperature – comparison experiments (second heating cycle; ABS)

Before testing, our ABS, CFR-ABS, and amphora samples are dried in the oven at 60°C for 24 hours, and PLA and CFR-PLA samples are dried in the oven at 45°C for 48 hours. The drying temperatures are chosen below the published glass transition temperature of these materials. the glass transition (T_g) of the materials are given as a range between the vertical shift starting point to the bottom of the shifted curve, as shown in *Figure 4-8*. Melting is an endothermic process which requires to absorb tremendous heat, the melting temperature can be detected as the temperature at the peak of a jump discontinuity in re-heat cycle in DSC curve with heat flow versus temperature. Similarly, the second heating cycle is selected to obtain the glass transition and melting point of the six materials, as shown in *Figure 4-9* where the measured results are summarized in *Table 4-3*. According to the DSC curves shown in *Figure 4-9*, two brands of ABS and Amphora do not have the certain melting temperature, this is because they belong to the amorphous polymers .

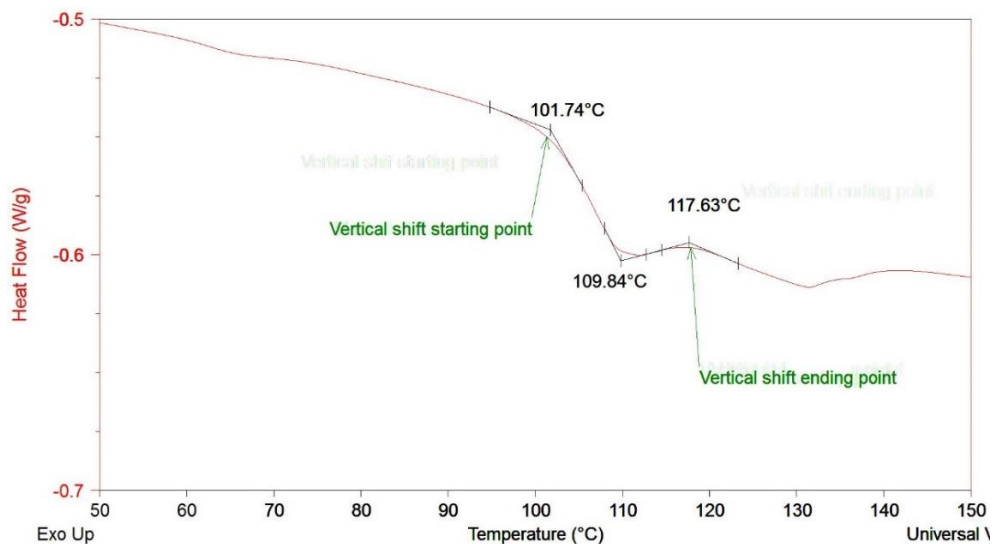


Figure 4-8 The second heating cycle of DSC curves of the materials generated by using heat/cool/heat method (ABS)

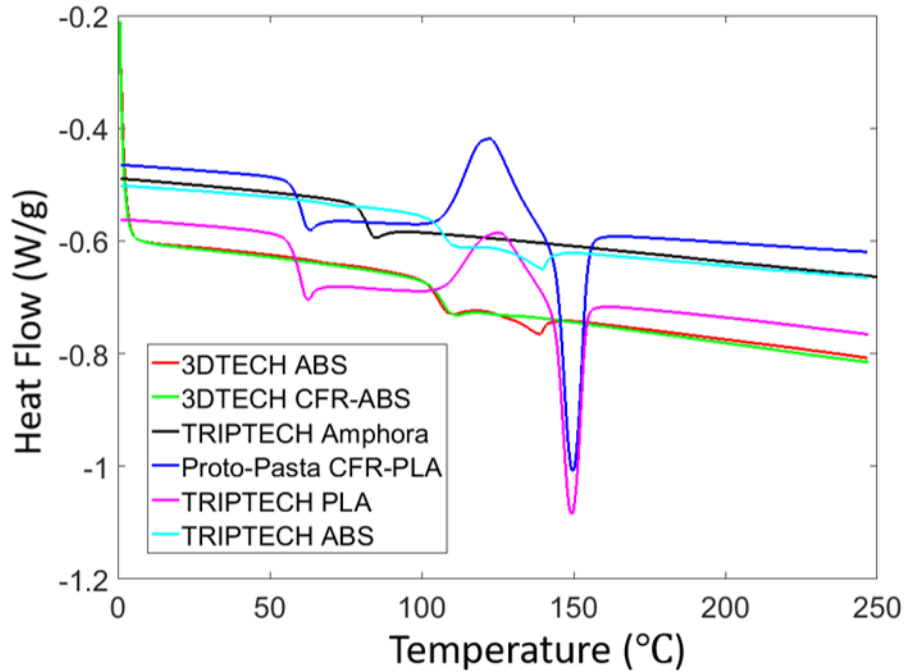


Figure 4-9 The second heating cycle of DSC curves of the six materials

Table 4-3 Glass transition temperature & melting point

Material	3DTXECH ABS	3DXTECH CFR-ABS	TRIPTECH ABS	TRIPTECH Amphora	TRIPTECH PLA	MatterHackers CFR-PLA
T_g	102.8°C	101.8°C	103.7°C	79.6°C	54.8°C	56.1°C
	~ 110.9°C	~ 108.2°C	~ 109.7°C	~ 84.2°C	~ 62.15°C	~ 61.5°C
T_m	N/A	N/A	N/A	N/A	142.32°C	140.8°C
					~ 149.62°C	~ 149.2°C

4.2 Force Measurements

The primary goal of building the filament rheometer device is to realize pressure drop by measuring the force required to push molten polymer and polymer composite material through the nozzle of a desktop 3D printer. As shown in *Equation 3.6*, the load cell is positioned to record the total force exerted on the filament. This includes the shear

force developed by pressure drop in the nozzle, and the friction force generated when the solid portion of filament interacts with the inside wall of the heat sink and heat break.

This subsection introduces the procedure and strategy for the measurement of force in the filament rheometer. In *Chapter Five*, further discussion of the assumptions and the derivation of force analysis is provided.

Minimizing force error in this research consists of six steps. First, the temperature in the nozzle must be maintained as constant at a value near the temperature sensor operating point. Since nozzle and the heat barrier thread into the heater block in practice, it is difficult to put a sensor such as a thermocouple with a large tip directly in contact with the nozzle. Therefore, two holes were drilled into the heater block position the thermocouple at a distance that is midway between the sensor and the screw hole as shown in *Figure 3-16*. In addition, cotton is used to wrap the entire heating block and the portion of the nozzle that is exposed to the air to maintain a near-isothermal processing condition. In addition, both the thermistor and thermocouple must be calibrated as described in Chapter Three. The temperature reading for the two different sensors is given in *Table 4-4*, which supports the assumption that the processing temperature is the same as the temperature that is read from the sensors.

Table 4-4 Comparison of thermistor and thermocouple
 (Note: the temperature data for two sensors are the average values over ten minutes measurement)

Setpoint (°C)	190	200	210	220	230
Thermistor	190.2°C	200.1°C	210.1°C	220.1°C	230.1°C
Thermocouple	191.1°C	200.9°C	210.8°C	220.8	230.9

Secondly, the cooling system has to be efficiently controlled to keep the filament in solid phase in the heat barrier above the nozzle. To achieve this in our device, a cooling fan and PTFE tube are incorporated in the system to reduce the heat conduction from heater block. A 5V 2200RPM fan is attached such that it can cool down the device without being directly in contact with heat sink, thus avoiding the vibration. PTFE has a low thermal conductivity (e.g., near $290 \pm 12 \text{ mW/m}\cdot\text{°C}$ at 232 °C [101]) as compared to the metal parts in the hot end, such as steel which has a density of $3286 \text{ mW/m}\cdot\text{°C}$ [102]. To reduce “heat creeping,” the system is shut down and cooled to room temperature after each measurement. Especially, in the rheological property measurement one should conduct several tests under the same temperature but different feeding velocity, the stop-and-cooling step is critical for maintaining the melting zone to be unchanged.

Thirdly, a matched set of idler and drive gear is selected to decrease the excessive force value on the force-time curve. This increases the accuracy of our mean value making more representative of the extrusion force (cf. *Figure 3-40*). Ten different pairs of drive gear and idler pulley were tested under the same operating conditions where the results appear in *Figure 4-10*. By comparing the output force, pair number 7 gives the smoothest curve among all candidates and is, therefore, chosen for all tests in this thesis.

Furthermore, the calibration of the load cell was performed before conducting a new set of experiments. Through this calibration, it is possible to collect the necessary data to explore how the signal changes when the loading is static and constant. Two strategies are implemented in Arduino DUE for calibration. One strategy allows the user to calibrate the load cell by measuring the weight of a fixed mass and then convert the result to a specific device parameter. Once this parameter is obtained and uploaded to

Arduino IDE it cannot be changed in process. Each new calibration constant is input manually, thus this method is time-consuming but stable. On the contrary, another technique can do the calibration every time before starting a new test. The user simply places a known mass on the load cell, and the value of weight of the mass will be displayed as outputs. Usually, the measurement is close to the known weight in this method, but sometimes the difference can be huge because this strategy is very sensitive to the vibration. Therefore, this method is quick but unstable. The first strategy is applied in this thesis in order to obtain the highest accuracy and stability. The force transducer is strain-gauge-based which sometimes results in a reading with a shift.. To minimize the error, the calibration is performed with the interval of every two sets of experiments.

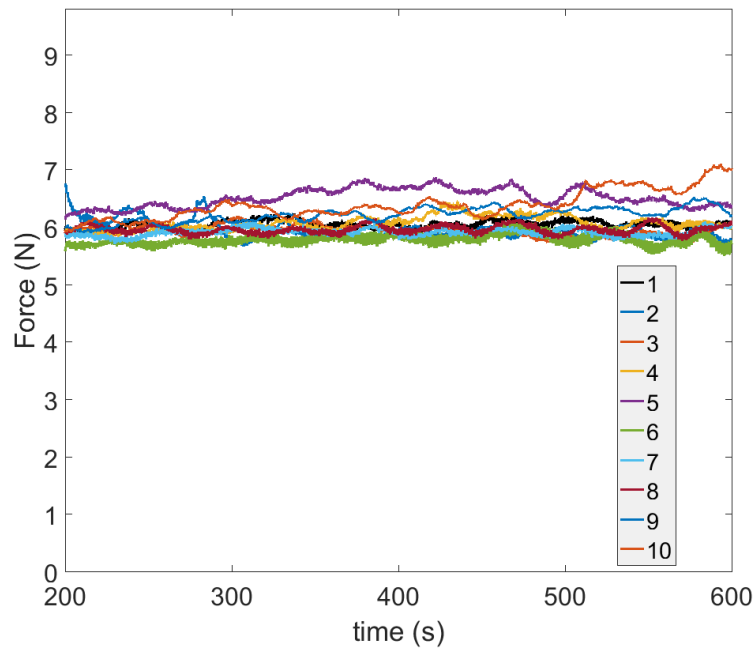


Figure 4-10 Comparison of the performance of ten different rollers

Turing off the stepper motor, then an standard 100g weight is loaded on the load cell, *Figure 4-11* shows that the load cell reading is noisy even under the static and

constant load, which could explain where the high-frequency components in the extrusion force (as in *Figures 3-38 and 3-41*) originates. Further identification of this noise source is beyond the scope of this work, however, most likely it could be the electronic noise from circuit the force is measured in static condition in which the stepper motor is off and no any other vibration in the system.

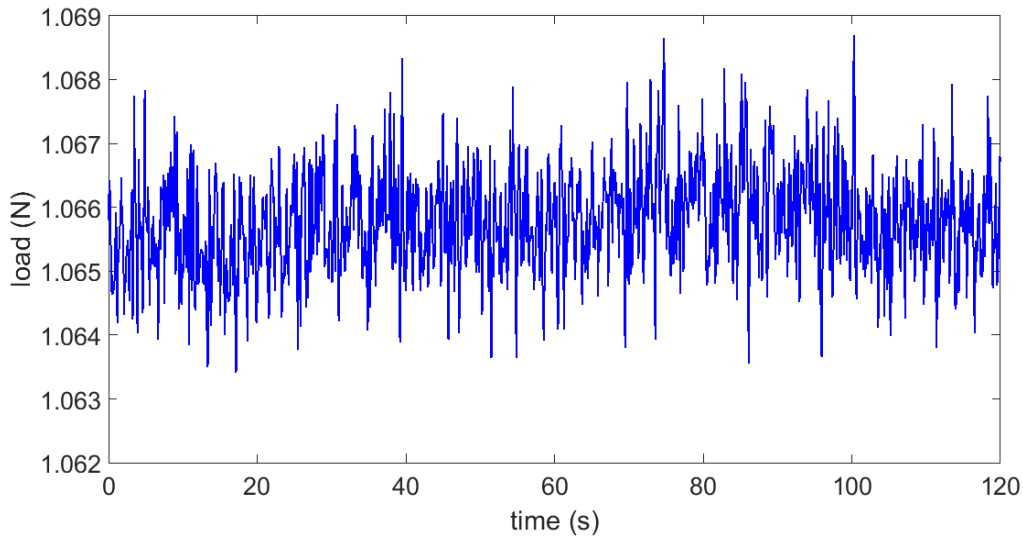


Figure 4-11 Load cell reading under 100g static load

The last step needed to set up our filament rheometer is to explore the friction force acting on the solid filament while it is delivered through the heat sink. Since the inside wall of the hotend is not manufactured as a single part as it contains an inlet screw, heat sink, and heat barrier. When the filament initially delivered into the liquefier, its tip can be easily bumped to the chamfer between these parts. To further explore this issue, the nozzle removed from the hotend as shown in *Figure 4-12*, to measure the friction force between the solid filament and the hotend. In this case, the measured friction force can exclude the force when filament gets stuck in the gaps. The tests are conducted under different feeding velocity. From *Figure 4-32*, the friction force changes with time and

feeding velocity in an irregular manner. In addition, different filaments have different diameter and surface roughness. Therefore, a friction force that is constant for all filaments processed is difficult to measure accurately in practice. Given that the friction forces in *Figure 4-12* are quite small as compared to the filament extrusion force, the friction force is assumed to be zero to simplify our analysis approach.



Figure 4-12 Hotend adjustment for friction force measurement

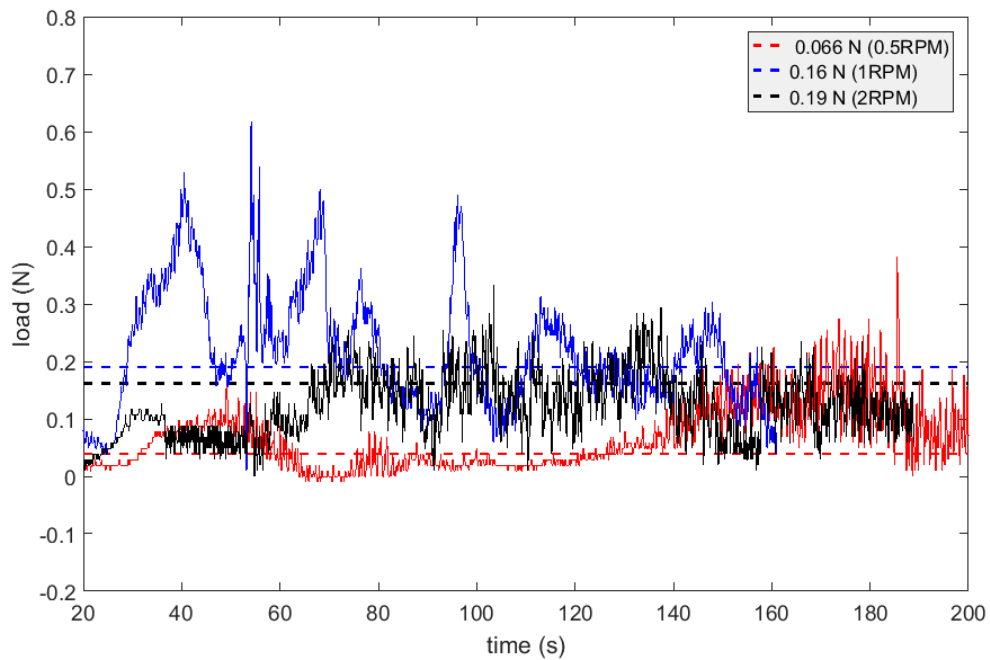


Figure 4-13 Friction force measurement under 0.5RPM, 1RPM, and 2RPM

In order to mimic the extrusion process of the desktop 3D printer when it is in use and measure the required force, the printing temperature and speed are referenced from the MakerBot Replicator. Our processing temperature is fixed at values recommended for the same material in MakerBot. Note here, however, that the MakerBot feed velocity varies for different structural parts such as the shell, filling, raft, and support. By using markings on the filament, the average linear velocity of filament in delivery is measured when the MakerBot prints different structural parts. These measurements make it possible to map the RPM of the stepper motor in extruder to the linear velocity of the filament. *Table 4-5* lists published values of velocity that is recommended for different parts.

Table 4-5 Feeding velocities on MakerBot Replicator

Objects	Raft	Shell	Filling
Feeding Velocity (RPM)	2.77 ~ 3.06	1.22 ~ 1.35	0.87 ~ 0.96

Here we consider the shell data as that of interest in our research. Thus, the average feeding velocity of printing shell and filling which is 1.2 RPM is selected as the experimental condition to evaluate extrusion force in our device. We use the print temperature taken from references for 3DXTECH [103] and TRIPTECH [104] in these measurements. All of the materials are tested under these specified conditions. For each material, 3 measurements are conducted to take the average value. The resulting ‘filament flow index’ is shown in *Figures 4-14* through *4-19*, and in *Table 4-6*.

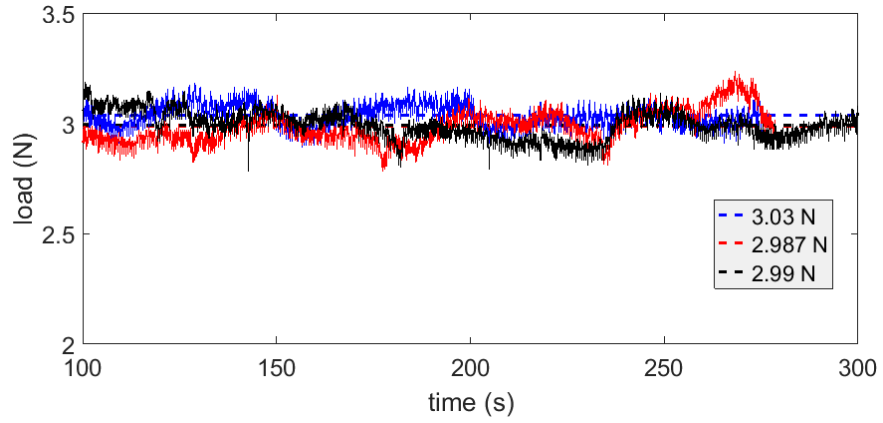


Figure 4-14 Three extrusion force measurements for 3DXTECH ABS

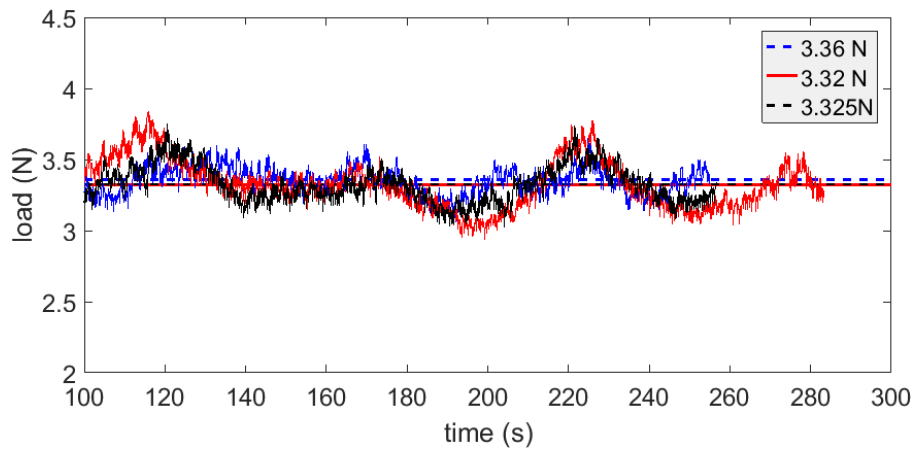


Figure 4-15 Three extrusion force measurements for 3DXTECH CFR-ABS

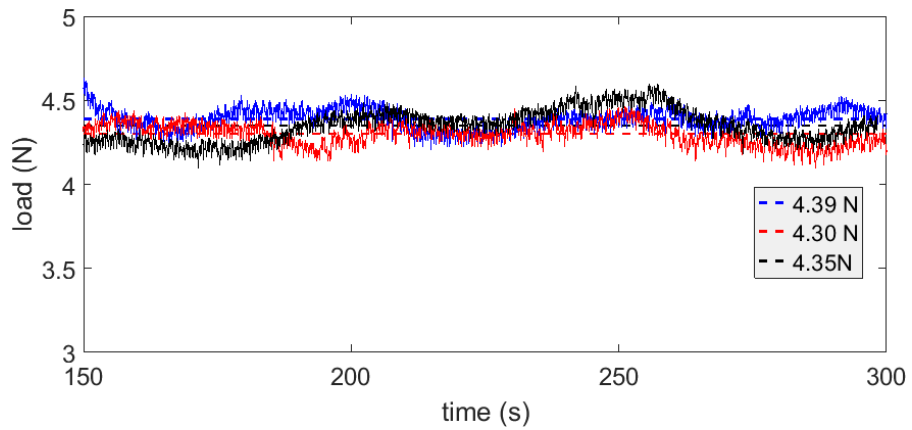


Figure 4-16 Three extrusion force measurements for TRIPTECT ABS

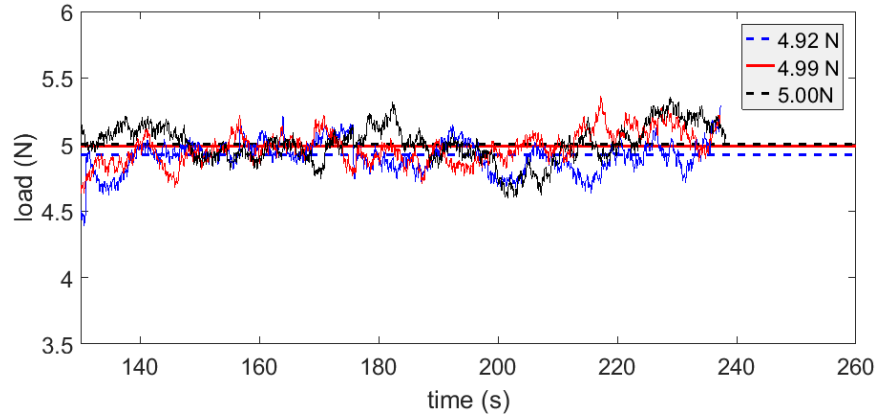


Figure 4-17 Three extrusion force measurements for TRIPTECH Amphora

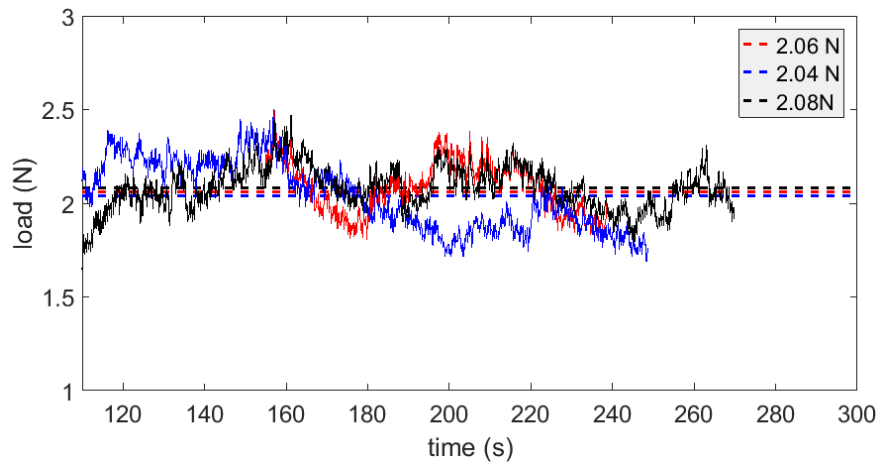


Figure 4-18 Three extrusion force measurements for MatterHackers CFR-PLA

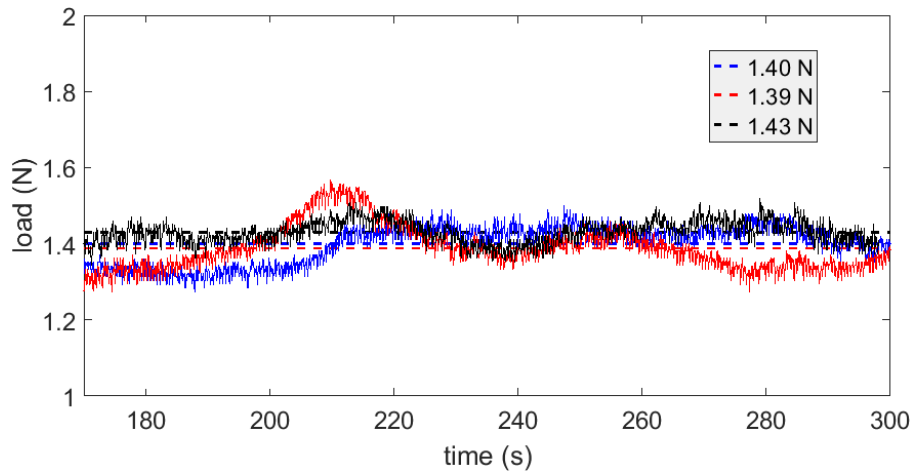


Figure 4-19 Three extrusion force measurements for TRIPTECH PLA

Our filament flow index (FFI) is not only a method used to indirectly measure the molecular weight of the sample, but it also provides a measure of fluidity and ease of the polymer melt flow. The Melt Flow Index (MFI) test is widely used in the plastics industry and follows have to follow either ASTM D1238 or ISO 01133 standards. In the traditional MFI test, under certain temperature and weight of plunger, MFI is defined in units of grams per 10 minutes. In our device, the nozzle has a geometrically complex die which does not conform to ASTM D1238. Therefore, when defining an FFI, using our device, the value of the force which relates to the processing temperature and filament feeding velocity is used as a processing index analogous to MFI for characterizing the filament material.

Table 4-6 Filament Flow Index - Extrusion force for six materials under the normal processing condition

Material	3DXTECH ABS	3DXTECH CFR-ABS	TRIPTECH ABS	TRIPTECH Amphora	TRIPTECH PLA	MatterHackers CFR-PLA
Stepper Motor Speed (RPM)	1.2	1.2	1.2	1.2	1.2	1.2
Processing Temperature (°C)	230	230	230	230	215	215
Force (N)	3.00	3.33	4.35	4.97	1.41	2.06

4.3 Rheological Property Measurement

4.3.1 Measurements Conducted by Filament Rheometer

The extrusion force can be converted to the pressure drop in the nozzle melt flow, and subsequently and further be related to the shear rate dependent viscosity of the

material. Once the extrusion force is accurately measured, it is possible to relate each force measurement for each material to the evaluation of rheological property (i.e., produce a shear rate and viscosity curve). Here we consider the same materials defined above which were evaluated for rheological properties using the HAAKE MARS 40 rotational rheometer (Thermo Fisher Scientific, Waltham, MA). With the intention of acquiring the viscosity curve, more force measurements must be conducted under different feeding velocity to generate enough data points for the curve. In addition to the measured force, the volume flow rate is also required to predict the rheological property of the filaments.

A direct method is used to measure the volume flow rate or linear feeding velocity. Firstly, the filament is randomly cut to different lengths for a total of ten samples. The volume is calculated from the measured diameter and length of the filament under a 3D scanner. Then the density is calculated by measuring the mass and volume of each cut sample as shown in *Figure 4-20 (a)*. Secondly, measuring the mass of extrudate at three different feeding velocity, then take the average of three measurements as shown in *Figure 4-20 (b)*

Then the mass flow rate can be calculated by dividing the mass by the processing time, which can then be further be converted to volume flow rate. This method is straightforward but somewhat time-consuming. As a measuring device our filament rheometer should have the capability of measuring the volume flow rate directly, that is, it is desirable for users do not need to measure the density of the filament. Therefore, an alternative approach is considered here as a supplement to simplify the experimental procedure. By measuring the effective radius of the drive gear, the linear filament feed

velocity can be calculated using *Equation 4.1*, where N represents the RPM. Assuming the filament feed velocity is equal to the average velocity of the molten polymer melt at the entrance of nozzle, the volume flow rate is obtained as the product of feeding velocity V and the area of the inlet of nozzle of radius r given as

$$V = r \frac{2\pi N}{60} \quad (4.1)$$

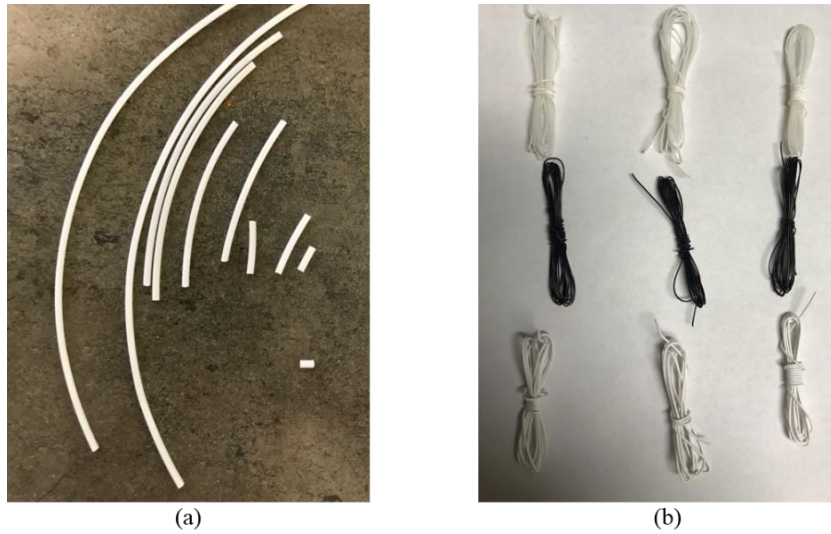


Figure 4-20: Filament used for density evaluation (a) Samples for density measurement, (b) Bundles of the extrudate.

The volume flow rate depends on the density of materials, but the average velocity of the filament at the inlet is independent of the material. In this approach, the measured linear velocity of the filament is assumed to be equal to the average velocity of the flow \bar{v}_z at the inlet of the nozzle. We assume that if the measured mass flow rate from these two methods are the same, then the pressure drop can be determined from the extrusion force and \bar{v}_z . The validation of the filament speed approach is tested by conducting the measurements for all materials at varying temperature and filament feed velocity. The results show that the maximum error between two the methods is within 2%

which is not expected to generate a significant error in evaluating of the rheological properties with our filament rheometer. *Figure 4-21* shows an example of flow rate evaluated from both methods for neat ABS at 220°C.

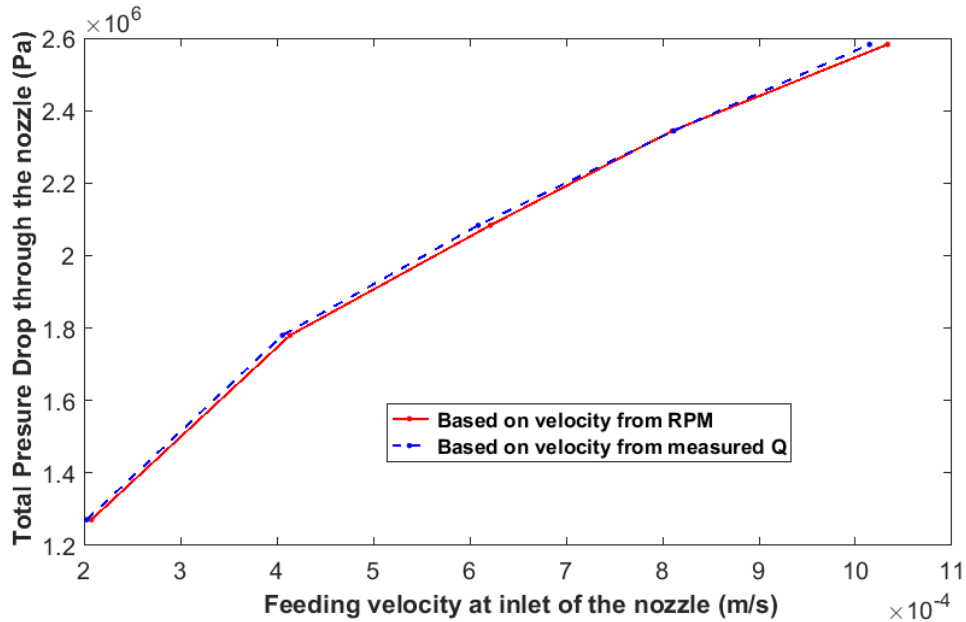


Figure 4-21 Comparison of velocity measurement between two different methods of flow rate measurement

Experiments were performed to evaluate the filament feed velocity for motor speeds ranging from 0.5 RPM to 2.5 RPM with 0.5 RPM interval. At each speed, both pressure drop and volume flow rate were obtained and further evaluated. The relationship between the pressure drop and the filament feed velocity at different temperatures for the six materials appears in *Figure 4-22*. As expected, all six materials yield an increase in force with increasing filament feed velocity. In addition, *Figure 4-23* shows that pressure drop decreases with increasing temperature for CFR-ABS, as expected.

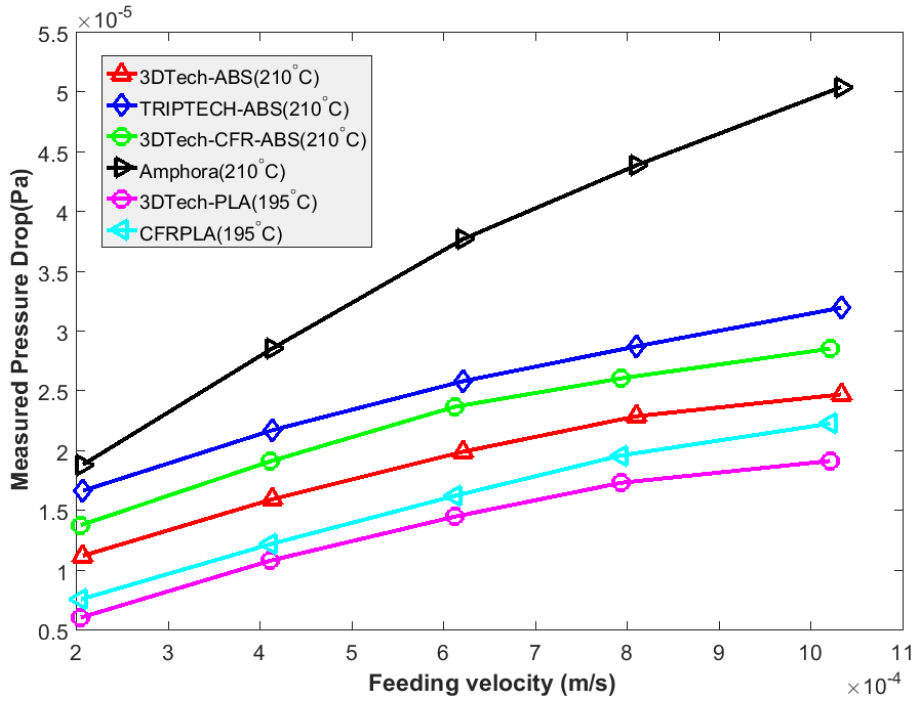


Figure 4-22 Pressure drop versus filament feed velocity for six materials

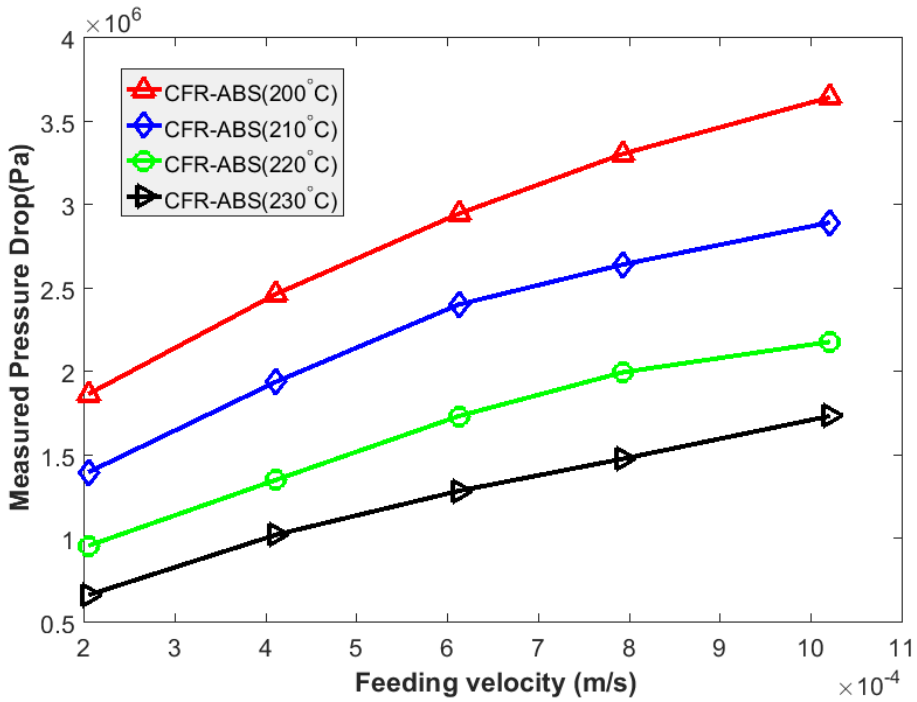


Figure 4-23 Pressure drop changes with temperature for CFR-ABS

4.3.2 Measurements Conducted by HAAKE MARS 40

As mentioned in Chapter Two, both capillary and the rotational rheometers are commonly used to measure the rheology of a polymer or polymer composite melt. Acknowledging that our low-cost filament extruder device is similar extrusion mechanism to the capillary rheometer, a rotational rheometer is considered here as a means for obtaining accurate polymer melt rheology by applying multiple testing methods.

In this research, the HAAKE MARS 40 (Thermo Fisher Scientific, Waltham, MA) cone and plate rheometer is shown in *Figure 4.24 (a)* is used as the professional rheometer capable of obtaining measured rheology properties that can be compared with results measured using our filament rheometer. The MARS 40 enables researchers to conduct rheological testing in controlled rate, controlled stress and controlled deformation mode in rotational oscillation providing controlled stress and controlled deformation of the sample. The sample geometry is defined by two parts of the MARS 40 rheometer: a lower plate and upper cone. The fixed lower plate used on MRS 40 is a cylindrical plate having a flat surface used to place and heat the sample of material. The rotating upper part is connected to the motor to provide rotary motion and typically has a conical plate, thus providing a sample region defined by the cone-and-plate. The cone-and-plate geometry in this research is defined by the parameters $a = 0.103\text{mm}$, $\alpha = 2^\circ$, $r = 10.002\text{mm}$, as shown in *Figure 4-24 (b)*, where the cone and plate material is a titanium alloy C20 2°/Ti – 02150728. The main purpose of using cone-and-plate geometry is to provide a near uniform shear rate within the sample which fills the gap between cone and plate [105].

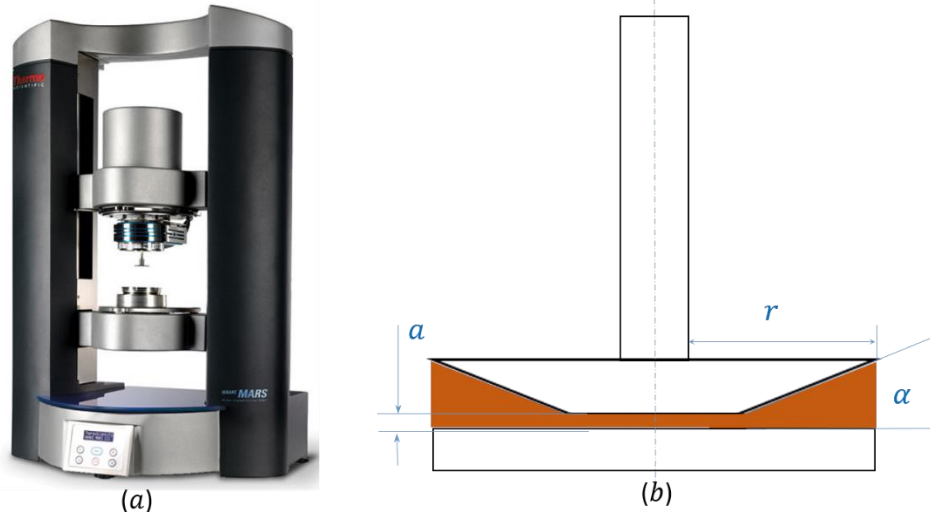


Figure 4-24 (a) HAAKE MARS 40 rotational rheometer; (b) cone-and-plate measuring geometry

Once the instrument is set up, the next step is to prepare the samples. The filament is thoroughly dried in the oven for 48 hours, then is chopped into small pieces. Melting the filament for each material under their thermal decomposition points in the molds, then the molten or softened chopped filament is compressed to make the final disk-like sample, as shown in *Figure 4-25*.



Figure 4-25 Sample Preparation for MARS 40

The purpose of using MARS 40 is to measure the flow properties of pseudoplastic where the viscosity decreases with increasing shear rate. Several measuring modes can be

used to obtain the viscosity curve that includes steady rotation with ramps, rotation with steps, and oscillating movement.

For the rotation ramp, the most straightforward method, the shear rate is continuously increased to generate data points. Under the rotation steps mode, the shear rate also increases in a similar manner to the rotation ramp method, but requires that steady state is attained at each speed (i.e., the resulting shear stress is stable). Results obtained using these two methods appear in *Figure 4-26* which shows that both are incapable of measuring the non-Newtonian viscosity at the high shear rates. This is because of the edge effects which is also known as edge failure which occurs when the deformation of the material becomes large [51, 54]. Therefore, a more stable measuring procedure is selected for our research.

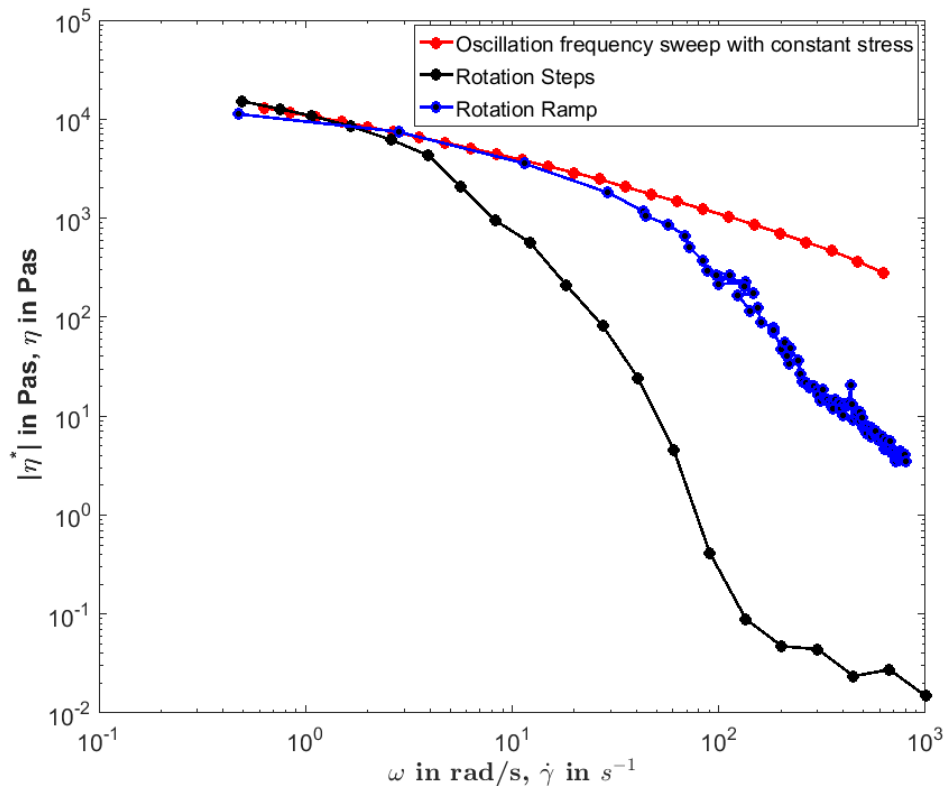


Figure 4-26 Comparison of different experiment mode (TRIPTeCH ABS at 210°C)

The oscillation frequency sweep with constant stress and oscillation frequency sweep with constant deformation are the conventional methods used to obtain complex viscosity curve over a range of shear rates. However, according to Bafna's study [106], these two methods have the precision issues at the extreme shear rate or angular velocity. Bafana found that the oscillation frequency sweep performs better at lower frequencies (or shear rate) under constant stress condition, but provides more accurate measurement at higher frequency at constant oscillation frequency. Therefore, we consider both measuring modes to guarantee more precise viscosity measurements for all materials and shear rate values considered. For more concise presentation, neat ABS (Triptech Plastic) at 210°C is chosen as an example to illustrate the experimental procedures. The same measuring process is used for other materials.

To determine the fix stress or strain values within the linear viscoelastic region (LVER), the oscillation stress sweep and oscillation amplitude sweep tests are conducted. Firstly, the LVER must be determined. A practical approach for detecting the linear viscoelastic region is to look for the region where the elastic modulus $G'(f)$ and loss modulus $G''(f)$ are independent of strain or stress (f is frequency). In this method, two extreme frequencies (the lowest and highest frequency corresponding to the angular frequency that will be applied in the oscillation frequency sweep test) are chosen, i.e., 0.1 HZ and 45 HZ. *Figure 4-27* shows the fixed strain value used for conducting the oscillation frequency sweep can be chosen any value between 0.004 – 0.07. Similarly, the fix stress can be chosen any value from 100-1000 Pa, as shown in *Figure 4-28*.

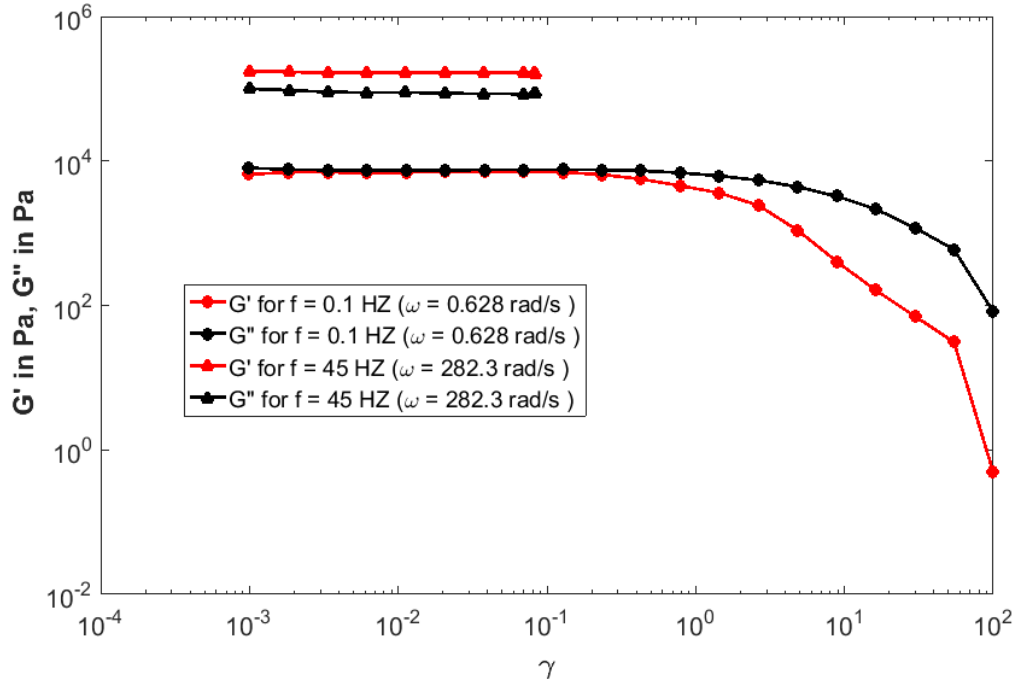


Figure 4-27 Oscillation amplitude sweep measurements

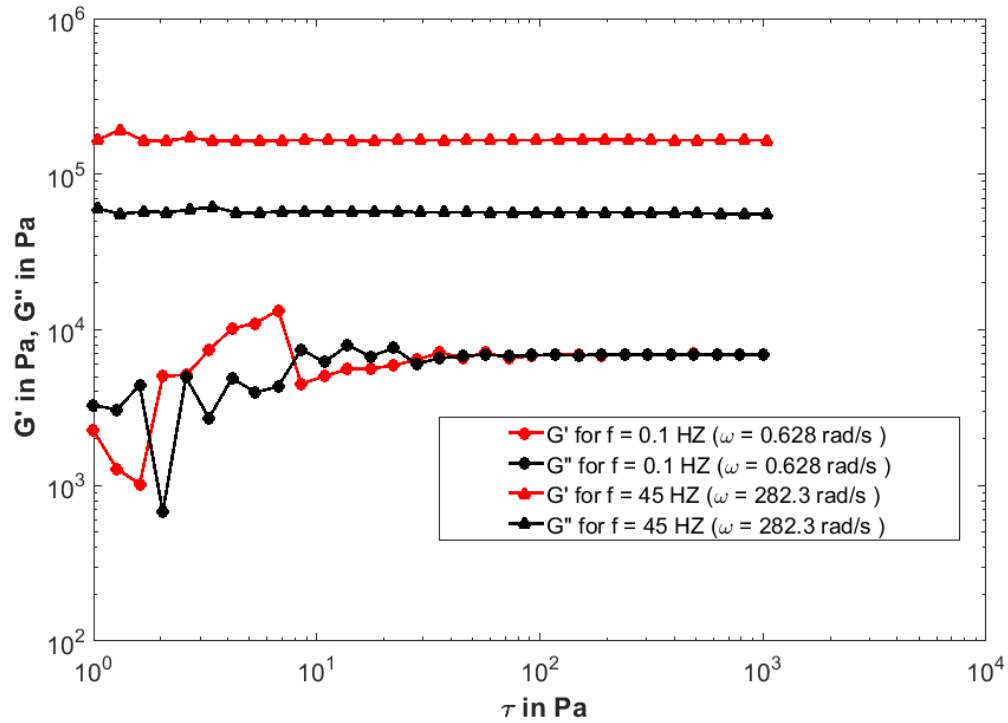


Figure 4-28 Stress sweep used to find the linear viscoelastic region

Applying the obtained stress and strain value in the oscillation frequency sweep with fixed stress and fixed strain tests, the comparison of results is given in *Figure 4-29*. Notice that, the difference between these two methods at two extreme frequency can be ignored, which means the issue mentioned in Bafna's study does not affect the experiments in our case. Repeat the above measurements for all six materials, the fixed stress or strain value of each material can be obtained. Then applying these values in the oscillation frequency tests, the viscosity curves for each material can be obtained

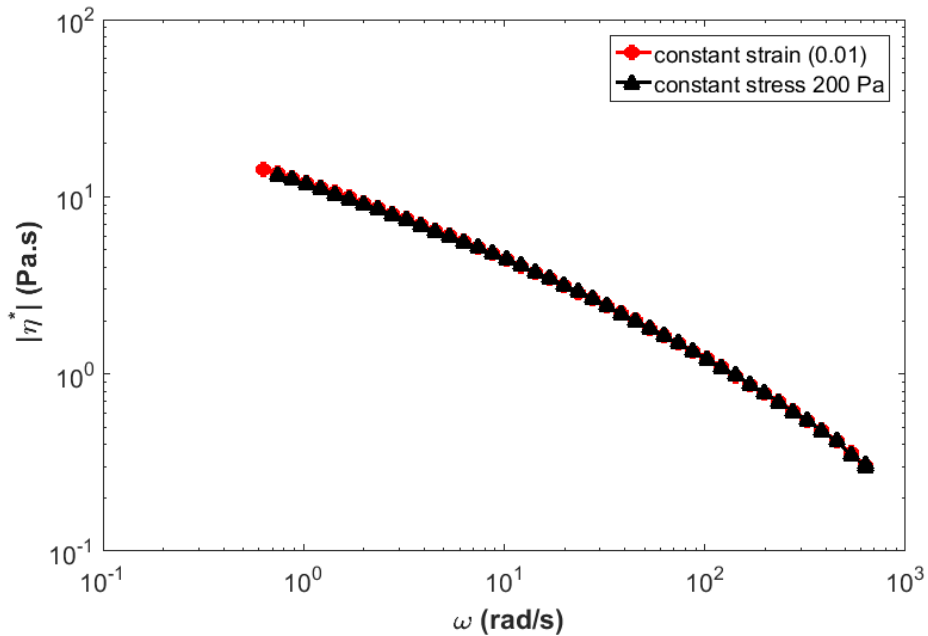


Figure 4-29 Comparison of two frequency sweep measuring modes

What needs to be pointed out is that the oscillation frequency sweep measurements are repeatedly conducted at least five times for each material at the fixed temperature. According the measurements for each material, the measured viscosity curves using MARS 40 for same material have vertical or horizontal shift to each other even under the same experimental conditions. For example, the measurements for

3DXTXTECH CFR-ABS at 210°C are given in *Figure 4-30*. Notice that the first, third and sixth measurements show the high repeatability to each other. In order to report the viscosity curves for a certain material measured by MARS 40, the representative is picked from one of the measurements that has high repeatability to at least two measurements under same condition. For example, in *Figure 4-30* the sixth measurement is chosen as the representative to represent the shear rate dependent viscosity for 3DXTXTECH CFR_ABS at 210°C. Applying the same strategy to other materials, the viscosity curves for all six materials are obtained and given in *Figure 4-31 and 4-32*. Notice that the viscosity curves are reported at two temperatures. The higher temperature is taken from the common printing temperature [107] of the filaments. The lower temperature acts as a reference group to verify if our device can predict the viscosity for the materials at different temperature.

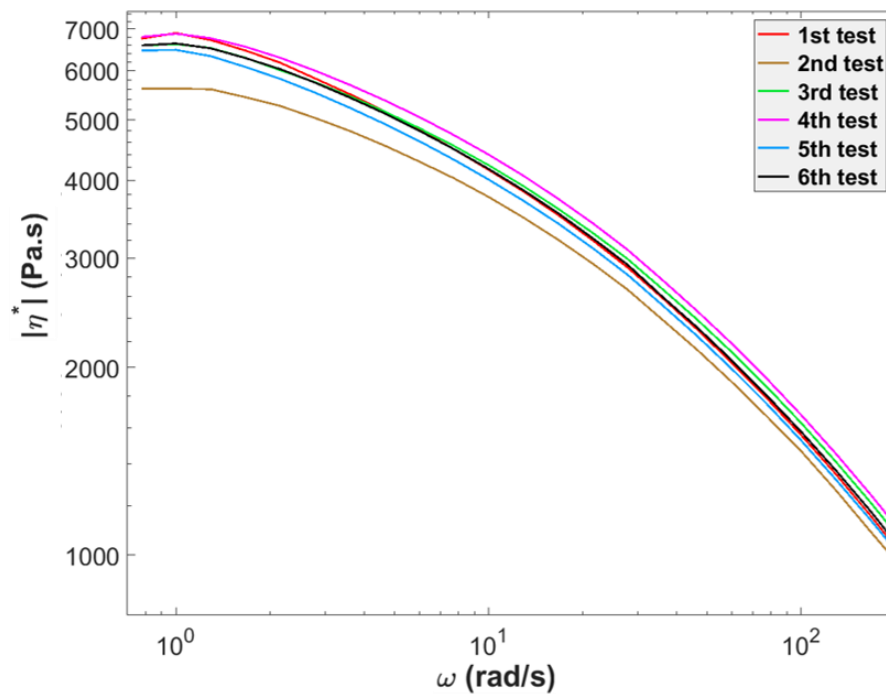


Figure 4-30 Discrepancy of the viscosity curves for the same material under same experimental condition in MARS 40 (3DXTXTECH CFR-ABS at 210°C)

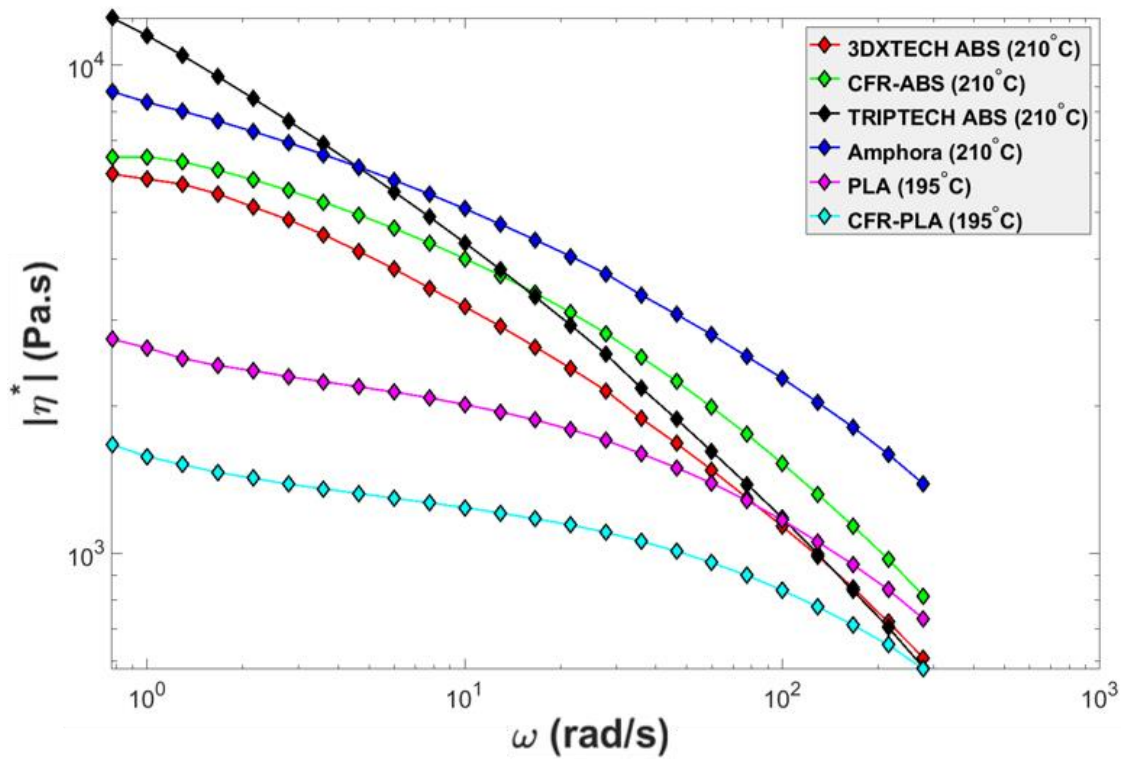


Figure 4-31 Viscosity curves for six materials at lower processing temperatures

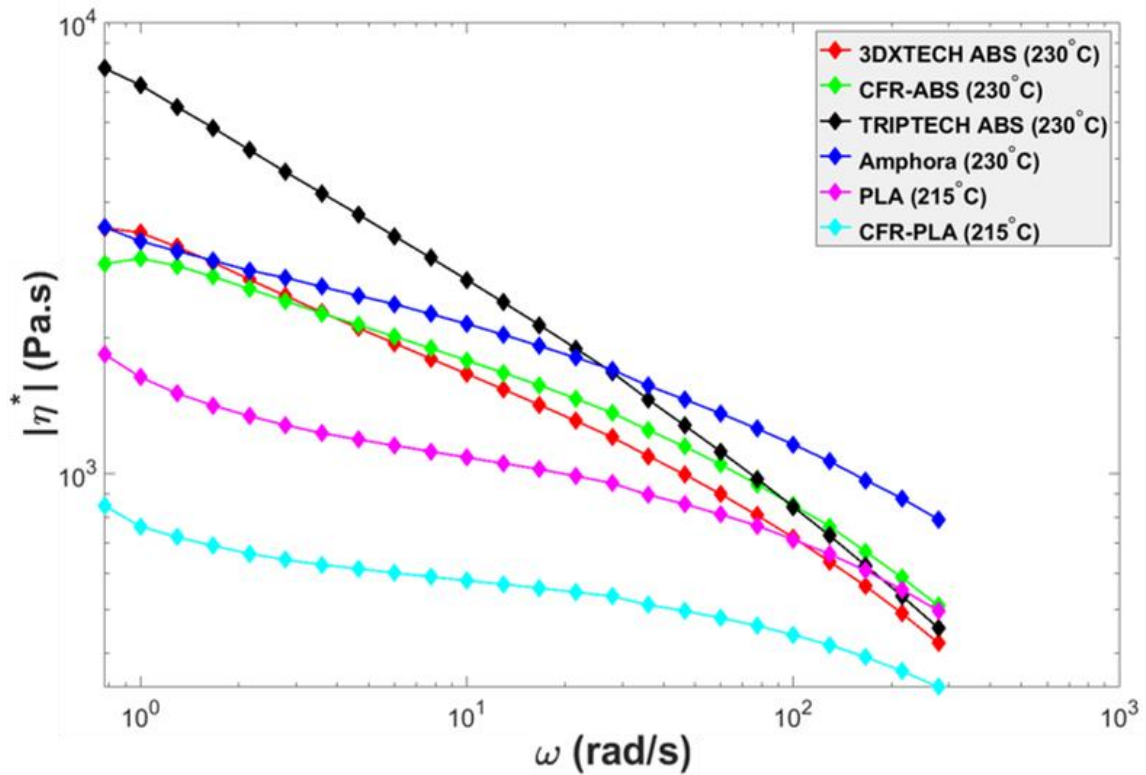


Figure 4-32 Viscosity curves for six materials at higher processing temperatures

The parameters of the curve-fitted data corresponding to the Power Law and Carreau-Yasuda GNF Model in PolyFlow (ANSYS, Canonsburg, PA) are reported in *Table 4-7* and *Table 4-8*, respectively. It is noted that the values of parameters for each material are taken from the average value of each curve-fitted data of five measurements under same condition. The shear rate region (applying Cox-Merz Rule) used for curve-fitting are $50 - 280 \text{ s}^{-1}$ and $0.8 - 280 \text{ s}^{-1}$ corresponding to Power Law Model and Carreau-Yasuda Model. Where n is Power Law index, k is consistency index, a is an exponent factor, λ is a time constant, η_0 is zero viscosity. Notice that, for the Carreau-Yasuda model η_∞ is set to be equal to zero.

Table 4-7 Parameters of Power Law GNF model curve-fitted in PolyFlow from the data by MARS 40 rotational rheometer.

Filaments	Temperature (°C)	n	k
3DXTECH ABS	210	0.424	1.59E+04
	230	0.507	7.04E+03
3DXTECH CFR- ABS	210	0.420	2.25E+04
	230	0.530	7.49E+03
Triptech Plastic ABS	210	0.334	2.52E+04
	230	0.418	1.28E+04
Triptech Plastic Amphora	210	0.546	1.83E+04
	230	0.650	5.89E+03
3DXTECH PLA	195	0.601	7.18 E+03
	215	0.695	3.02E+03
MatterHackers CFR-PLA	195	0.679	3.89E+03
	215	0.777	1.33E+03

Table 4-8 Parameters of Carreau-Yasuda GNF model curve-fitted in PolyFlow from the data by MARS 40 rotational rheometer.

Filaments	Temperature (°C)	a	n	η_0	λ
3DXTECH ABS	210	0.679	0.424	6.82E+03	0.198
	230	0.402	0.507	7.34E+03	0.553
3DXTECH CFR-ABS	210	0.856	0.420	7.18E+03	0.124
	230	0.602	0.530	3.96E+03	0.215
Triptech Plastic ABS	210	0.577	0.334	2.68E+04	0.662
	230	0.462	0.418	2.24E+04	0.234
Triptech Plastic Amphora	210	0.686	0.546	9.91E+03	0.247
	230	0.531	0.650	4.59E+03	0.432
3DXTECH PLA	195	0.9273	0.601	2.44E+03	0.589
	215	0.6383	0.695	1.57E+03	0.498
MatterHackers CFR-PLA	195	0.9293	0.679	1.47E+03	0.433
	215	0.5662	0.777	8.34E+02	0.3147

CHAPTER FIVE

Math Model

The main focus of this thesis is to obtain rheology property of polymer and polymer composite filament from a simple FFF extrusion test device. This chapter presents the derivation of a math model used for this purpose. The relationship between flow rate and pressure drop within a FFF extrusion nozzle using a Power Law fluid model will be derived. The polymer melt flow model will then be used to compute Power Law fluid model parameters from pressure drop and flow rates measured with our filament rheometer. A non-linear least-square regression is applied to curve fit the data points numerically. In the end, the effectiveness and usefulness of the low-cost device is checked by comparing the predicted Power Law fluid parameters to those obtained in *Chapter Four* using the MARS 40 rheometer. An error analysis is also included which considers possible variations in flow domain shape that can result in FFF extrusion.

5.1 Viscosity and Flow Functions in the Nozzle

5.1.1 Nozzle Geometry and Assumptions

A stainless-steel nozzle has a 0.4 mm exit diameter is selected for this study. To obtain a better description of the FFF extrusion flow domain, the inside geometry of the nozzle is measured by cutting the nozzle in half and scanning it using a KEYENCE (Keyence Corporation, Itasca, IL) 3D scanner. The sketch of the inside geometry of the nozzle is given in *Figure 5-1*. The extrusion die contains three regions, the upper circular

tube (I), the conical region (II), and the capillary die (III). Note that the geometry shown in *Figure 5-1* only represents the nozzle itself and does not provide information on the filament melting zone upstream of the nozzle. As mentioned in *Chapter Three*, the melting region depends on the effectiveness of cooling system, thermal properties of the hotend and filament, and flow rate. Generally, the processing temperature in FFF process is well above the glass transition even melting temperature for polymers. The melting zone of filament usually exceeds the nozzle. Besides, the diameter of the capillary die in the nozzle would be slightly decreased, or increased corresponding to the potentials that the high-temperature-resistance residue sticking to the inside wall, and the high stiffness carbon fibers wear the capillary die. All these small changes in melting zone are difficult detected from the force signal accurately but would generate a significant error for the predictions of pressure drop as well as viscosity. The influence of these two parameters on rheology prediction will be given later.

To simulate the polymer melts flow in FFF nozzle extrusion, assumptions must be made to simplify the modeling approach for the complex flow in the nozzle. The assumptions with regards to boundary conditions, thermodynamic, flow, and rheological behavior used in this study are given as follows:

1. *Incompressible polymer and polymer composite melt flow;*
2. *No-slip boundary condition at the nozzle wall;*
3. *Isothermal fluid flow condition;*
4. *Gravity of extrudate is negligible;*
5. *Polymer and polymer composite melt flow is in steady state;*
6. *The pressure at the nozzle outlet is equal to zero;*
7. *Flow entrance and exit effects are negligible.*
8. *The melt rheology is purely viscous and can be modeled with as a Generalized Newtonian Fluid.*

9. The short fiber filled polymer composite is assumed to behave as a homogeneous fluid
10. The Power Law model is applicable to polymer and polymer composite melt flow in the nozzle during extrusion.
11. The Reynolds number of the flow is small making it possible to ignore inertia effects [108].
12. The flow is axisymmetric with respect to the z-axis (cf. Figure 5-2)

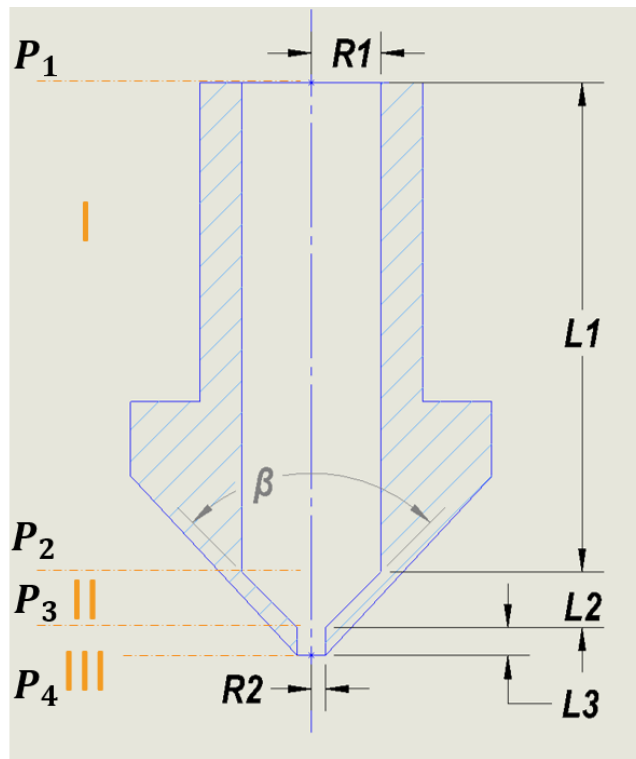


Figure 5-1 Inside dimensions of nozzle

5.1.2 Pressure Drop due to Shear Flow

In addition to the shear stress, polymer melts are also subjected to normal stress when flow through a geometrically complex nozzle. Ignoring entrance and exit effects, the streamlines in region I and III are parallel, such that the polymer melt experiences a laminar pure shear flow. The velocity field becomes more complicated when polymer melt travels through the conical section of the die (region II). In this case, the

polymer melt is not only subjected to the shear but also experiences extensional stress in flow direction due to acceleration of the material in the streamline direction. As mentioned above, and in Chapter Two, this extension component is ignored in this research, and we focus instead only on the shear stress.

To model the simple shear flow, a Generalized Newtonian Fluid (GNF) model commonly used in polymer process modeling is employed in the subsequent analysis. The GNF model is limited to incompressible flows. Among the numerous GNF models in [23] and [52], the Power Law Model is selected for our work to derive a math model that can be used to calculate viscosity parameters from measured filament force and velocity during FFF extrusion. The Power Law fluid is chosen here since it is able to capture the shear thinning behavior of the polymer melt while being simple enough to yield closed-form equations of pressure drop as a function of flow rate in the nozzle.

The constitutive equation of the Newtonian fluids is the most straightforward equation that can be used to model the rheological behavior of polymers at relatively low rates of deformation. Due to its simplicity, the equations of polymer melt flow in the nozzle is derived using Newtonian constitutive equations as the starting point below. Since the inside geometry of a commercial desktop 3D printer nozzle is of relatively high complexity, the overall geometry is divided into three regions as shown in Figure 5-1. The equations of pressure drop are derived for each region separately. First of all, region I is modeled as a small tube in which the polymer melt flows through. We start with the z-component of the Navier-Stokes equation in cylindrical coordinates see e.g., *Figure 5-2*) written as

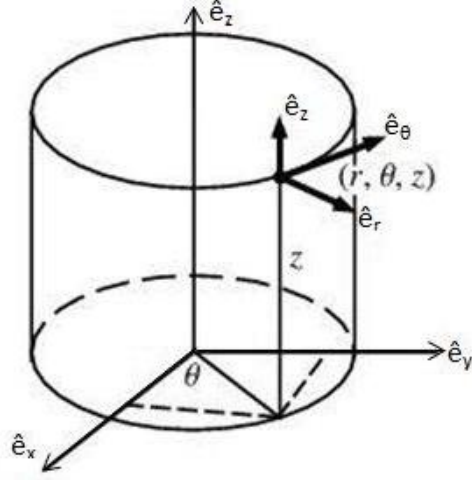


Figure 5-2 Cylindrical coordinate

$$\begin{aligned} & \rho \left(\frac{\partial v_z}{\partial t} + v_r \frac{\partial v_z}{\partial r} + \frac{v_\theta}{r} \frac{\partial v_z}{\partial \theta} + v_z \frac{\partial v_z}{\partial z} \right) \\ &= -\frac{\partial P}{\partial z} + \rho g_z + \mu \left[\frac{1}{r} \frac{\partial}{\partial r} \left(r \frac{\partial v_z}{\partial r} \right) + \frac{1}{r^2} \frac{\partial^2 v_z}{\partial \theta^2} + \frac{\partial^2 v_z}{\partial z^2} \right] \end{aligned} \quad (5.1)$$

where ρ is the density of the polymer, P is the fluid pressure, and v_z , v_r , and v_θ are the components of fluid velocity in axial, radial, and tangential direction, respectively.

According to the assumption 1 and 2 listed above, we define the boundary condition $v_\theta = 0$ and $v_r = 0$ on the nozzle wall. Since the flow is assumed to be steady state, the derivatives with respect to time are zero. In addition, the remaining terms on the left hand side of *Equation 5.1* may be set to zero for low Reynolds number flows. Since the effect of gravity is ignored and the flow is assumed axisymmetric (i.e., derivatives with respect to θ are zero), *Equation 5.1* reduces to

$$\frac{\partial P}{\partial z} = \mu \frac{1}{r} \frac{\partial}{\partial r} \left(r \frac{\partial v_z}{\partial r} \right) \quad (5.2)$$

where an order-of-magnitude analysis yields that the last term on the right-hand side of *Equation 5.1* is small compared to the remaining two terms. We label the pressure at the

entrance and exit of region I in *Figure 5-1* are P_1 and P_2 , respectively, and then integrate *Equation 5.2* along the z -direction to obtain

$$\int_{P_1}^{P_2} dP = \int_0^{L_1} \mu \frac{1}{r} \frac{d}{dr} \left(r \frac{dv_z}{dr} \right) dz \quad (5.3)$$

where the partial derivative have been replaced with total derivatives in our 1D model.

Applying the boundary conditions $v_z = 0$ at $r = R_1$ and $v_z = \infty$ at $r = 0$ in the integration in *Equation 5.3* yields the velocity profile

$$v_z = \frac{\Delta P_1}{4\mu L_1} (R_1^2 - r^2) \quad (5.4)$$

where $\Delta P_1 = P_2 - P_1$, is the pressure drop through region I. To obtain pressure drop ΔP_1 as a function volume flow rate Q , the control volume (CV) appearing in *Figure 5-3* is used.

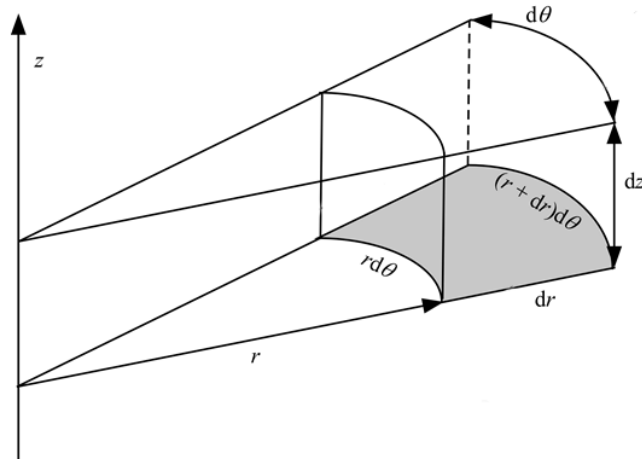


Figure 5-3 Control volume (CV) of the flow

By substituting v_z from *Equation 5.4* into the equation of volume flow rate

$$Q = \int_0^{2\theta} \int_0^{R_1} v_z(r) r d\theta dr \quad (5.5)$$

the equation of pressure drop as a function of volumetric flow rate Q is obtained as

$$\Delta P_1 = \frac{8\mu L_1 Q}{\pi R_1^4} \quad (5.6)$$

Equation 5.6 can also be expressed in terms of the average velocity \bar{v}_z of the flow at the entrance of nozzle as

$$\Delta P_1 = \frac{8\mu L_1 \bar{v}_z}{R_1^2} \quad (5.7)$$

Equations for shear rate and wall shear rate in terms of Q and \bar{v}_z may be derived from the velocity profile equation (cf. Equation 5.4) as

$$\dot{\gamma}_1 = \frac{\Delta P_1 r}{\mu L_1} \quad (5.8)$$

$$\dot{\gamma}_{w1} = \frac{4Q}{\pi R_1^3} \quad (5.9)$$

or

$$\dot{\gamma}_{w1} = \frac{4\bar{v}_z}{R_1} \quad (5.10)$$

where $\dot{\gamma}_{w1}$ represents the wall shear rate in region I. Similarly, it follows that the wall shear stress for a Newtonian Fluid is

$$\tau_{w1} = \frac{4Q\mu}{\pi R_1^3} \quad (5.11)$$

or

$$\tau_{w1} = \frac{4\mu\bar{v}_z}{R_1} \quad (5.12)$$

Considering region II in *Figure 5-1*, we assume that the internal nozzle radius decreases linearly from R_1 at the top of the cone to R_2 at its bottom. To simplify the flow equations in nozzle cone, the conical section is partitioned into small cylindrical elements of height δl and radius δr , as shown in *Figure 5-4*, thereby ignoring the radial flow in each cylinder

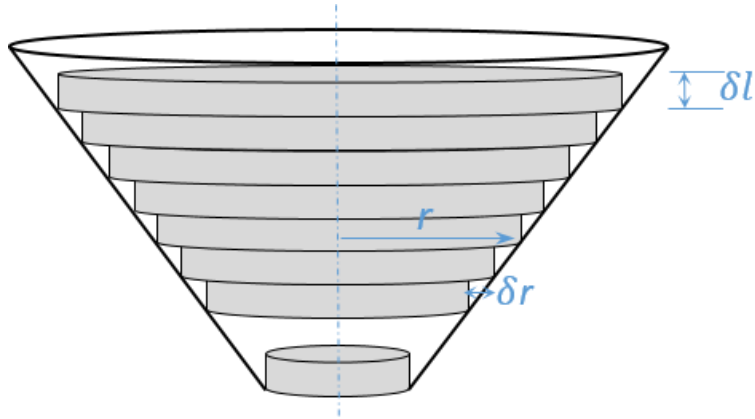


Figure 5-4 Approximation approach of flow in a conical tube

Integrating *Equation 5.6* over the length L_2 gives

$$\Delta P_2 = \int_0^{L_2} \frac{8\mu Q}{\pi R(z)^4} dz \quad (5.13)$$

where $dz = \frac{L_2}{R_1 - R_2} dr$. The result becomes

$$\Delta P_2 = \frac{8\mu Q}{3\pi} \cot \frac{\beta}{2} (R_2^{-3} - R_1^{-3}) \quad (5.14)$$

Which may be written in terms of the average velocity \bar{v}_z as

$$\Delta P_2 = \frac{8}{3} \mu \bar{v}_z R_1^2 \cot \frac{\beta}{2} (R_2^{-3} - R_1^{-3}) \quad (5.15)$$

Equations for pressure drop in region III follows an identical process as that shown above for region I, thus ΔP_3 may be written as

$$\Delta P_3 = \frac{8\mu L_3 Q}{\pi R_2^4} \quad (5.16)$$

or

$$\Delta P_3 = \frac{8\mu L_3 \bar{v}_z R_1^2}{R_2^4} \quad (5.17)$$

The overall pressure drop written in terms of flow rate Q for the entire nozzle with a Newtonian fluid is the summation of *Equation (5.6, 5.14, 5.16)*. While the derivation for a Newtonian fluid appearing above provides a starting point for our

analysis, the shear thinning behavior of a polymer melt must be considered when developing a useful relationship between flow rate and pressure drop for our FFF filament rheometer. Therefore, the following provides a similar derivation based on the Power Law GNF model.

In addition to the polymer viscosity being shear rate dependent, we also consider its temperature dependence. *Equation 2.8* and *2.9* represents the dependence of viscosity of polymeric materials on temperature. In the case of our device, T is the real time temperature measured by the temperature sensor and T_0 is the desired processing temperature (i.e., the setpoint of temperature in Arduino). According to the published data by Nicolae, et al. [109], the activation energy (E_0 in *Equation 2.9*) of PLA is 21-23 kJ/mol. Assuming the gas constant of air R is equal to 8.31 J/(K· mol) [110]. Then E_0/R in *Equation 2.9* has the magnitude of 10^3 . In *Figure 3-34*, the maximum of temperature fluctuation when the low-cost device in operation is 0.3°C. Therefore the magnitude of $(\frac{1}{T} - \frac{1}{T_0})$ is 10^{-6} , such that $a_T(T)$ in $a_T(T)$ is approximately equal to 1. Finally, *Equation 2.8* becomes

$$\eta(T, \dot{\gamma}) = \eta(\dot{\gamma}) \quad (5.18)$$

Besides, the activation energy of ABS is referenced from [111], and the results also yield $a_T(T) = 1$. Therefore, it is safe to assume the viscosity measurements in our device are in the isothermal condition.

To include the polymer melt shear thinning behavior in our analysis, we now consider the constitutive equation of a power-law fluid may be written as [112]

$$\dot{\gamma} = \phi \cdot \tau^m \quad (5.19)$$

where the viscosity typically takes the form [112]

$$\eta = k \cdot \dot{\gamma}^{n-1} \quad (5.20)$$

In the above, m is the flow exponent, ϕ is the fluidity, n is the power law index and k is the consistency index. Note that $k = \phi^{-1/m}$, $n = \frac{1}{m}$. Considering the modeling assumptions listed above, simple shear in a tube yields $\tau = \frac{\Delta Pr}{2L}$ which may be substituted into *Equation 5.19* to obtain

$$\dot{\gamma} = \frac{dv}{dr} = \left(\frac{\Delta Pr}{2L}\right)^m \phi \quad (5.21)$$

Assuming the coordinate system in *Figure 5-2*, we can integrate *Equation 5.21* over region I in *Figure 5-1*, to obtain an expression for the velocity profile as

$$v(r) = \frac{\phi R_1}{m+3} \left(\frac{\Delta P_1}{2L_1}\right)^m (R_1^{m+1} - r^{m+1}) \quad (5.22)$$

It follows that the volume flow rate and mean velocity at the entrance can be derived using the same approach as that used for Newtonian fluids above to respectively yield

$$Q = \frac{\pi R_1^3}{1/n+3} \left(\frac{\Delta P_1 R_1}{2kL_1}\right)^{1/n} \quad (5.23)$$

and

$$\bar{v} = \frac{R_1}{1/n+3} \left(\frac{\Delta P_1 R_1}{2kL_1}\right)^{1/n} \quad (5.24)$$

Rearranging *Equation 5.23* yields

$$\Delta P_1 = 2kL_1 \left(\frac{Q(1/n+3)}{\pi R_1^{3+1/n}}\right)^n \quad (5.25)$$

or

$$\Delta P_1 = 2L_1 \left(\frac{Q(m+3)}{\phi \pi R_1^{m+3}}\right)^{1/m} \quad (5.26)$$

In the same way, the equations of pressure drop and volume flow rate in region II and III are given as

$$\Delta P_2 = \frac{2k \cot \frac{\beta}{2}}{3n} \left(\frac{Q \left(\frac{1}{n} + 3 \right)}{\pi} \right)^n (R_2^{-3n} - R_1^{-3n}) \quad (5.27)$$

or

$$\Delta P_2 = \frac{2m \cot \frac{\beta}{2}}{3} \left(\frac{Q(m+3)}{\phi \pi} \right)^{1/m} (R_2^{-3/m} - R_1^{-3/m}) \quad (5.28)$$

$$\Delta P_3 = 2kL_3 \left(\frac{Q(1/n+3)}{\pi R_2^{3+1/n}} \right)^n \quad (5.29)$$

or

$$\Delta P_3 = 2L_3 \left(\frac{Q(m+3)}{\phi \pi R_2^{m+3}} \right)^{1/m} \quad (5.30)$$

By simply substituting $Q = \bar{v}\pi R_1^2$ into the above equations one can obtain the pressure drop equations with \bar{v} as the independent variable. The ultimate goal of building the analytical math model is to compare and validate the power-law indexes obtained with our FFF filament rheometer to those computed from MARS 40 measured data. Therefore, the expression of pressure drop across the entire FFF nozzle as a function of Power-law index (n) and consistency index (k) is obtained by summing *Equation (5.25, 5.27, 5.29)* as

$$\Delta P = 2k \left(\frac{Q \left(\frac{1}{n} + 3 \right)}{\pi} \right)^n \left[\frac{L_1}{R_1^{3n+1}} + \frac{\cot \frac{\beta}{2}}{3n} (R_2^{-3n} - R_1^{-3n}) + \frac{L_3}{R_2^{3n+1}} \right] \quad (5.31)$$

or

$$\Delta P = 2k \left(\bar{v} R_1^2 \left(\frac{1}{n} + 3 \right) \right)^n \left[\frac{L_1}{R_1^{3n+1}} + \frac{\cot \frac{\beta}{2}}{3n} (R_2^{-3n} - R_1^{-3n}) + \frac{L_3}{R_2^{3n+1}} \right] \quad (5.32)$$

5.2 Simple Analysis of the Melting Zone in the FFF Liquifier

The geometry parameters in *Equation 5.31* must be known before predicting the power-law model coefficients. As described above, the inside geometry of the nozzle can

be measured using a 3D scanner, but the actual geometry that defines the flow domain of the polymer melt during processing may be different than the interior geometry of the nozzle. It would be helpful to have an accurate description of the temperature distribution during processing. Unfortunately, measuring temperature over the small geometry of the hot end near the thermal barrier is difficult. Without knowing specific temperatures over the hot end, it is not possible to assess the height of the molten polymer material within the flow channel upstream of the nozzle.

In this project, the melting zone is examined from the rough measurements. Firstly, the inside geometry of the nozzle is measured using the method mentioned in Chapter Three and is given in *Figure 5-5* and *Table 5-1*. Secondly, running the low-cost device to extrude filament for a certain filament for a period of time. The time is taken the same as the extrusion force measurement time, i.e., three minutes. Then, the nozzle is screwed off from the heater block along with the re-solicited filament inside when the system is cooled down to room temperature. It is noticed that there is a portion of filament where above the nozzle is swelled and its original diameter (i.e. 1.75 mm) is increased to the same as the inside diameter of the heater barrier (i.e., 2 mm), and this part is considered to be melted before pushed into the nozzle when FFF in process. The length of this parts is measured and counted into the melting region. In the end, the melting region is assumed as the combination of the inside dimensions of nozzle with the length of the swelled filament above the nozzle.

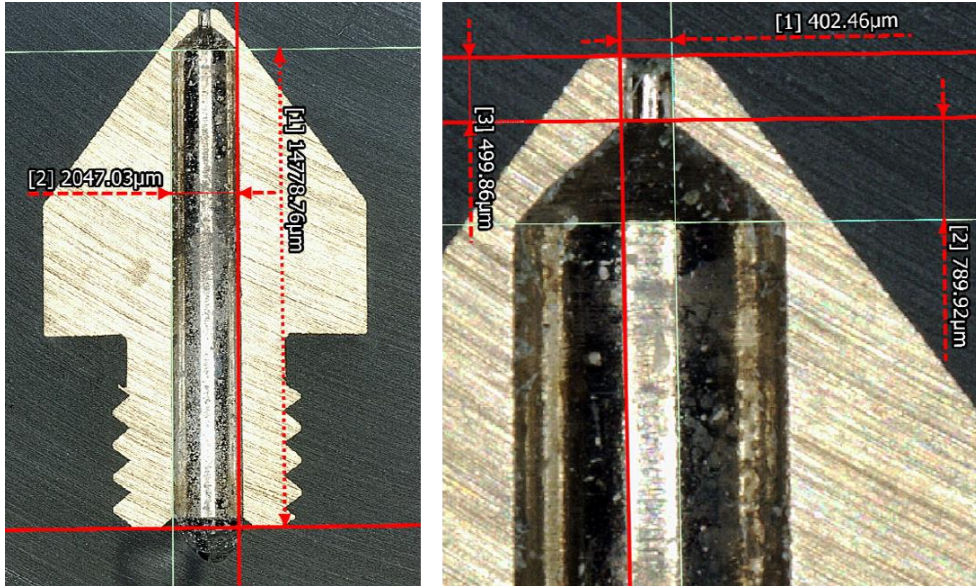


Figure 5-5 Inside dimensions of the nozzle used on Filament Rheometer measured by the 3D measurement system

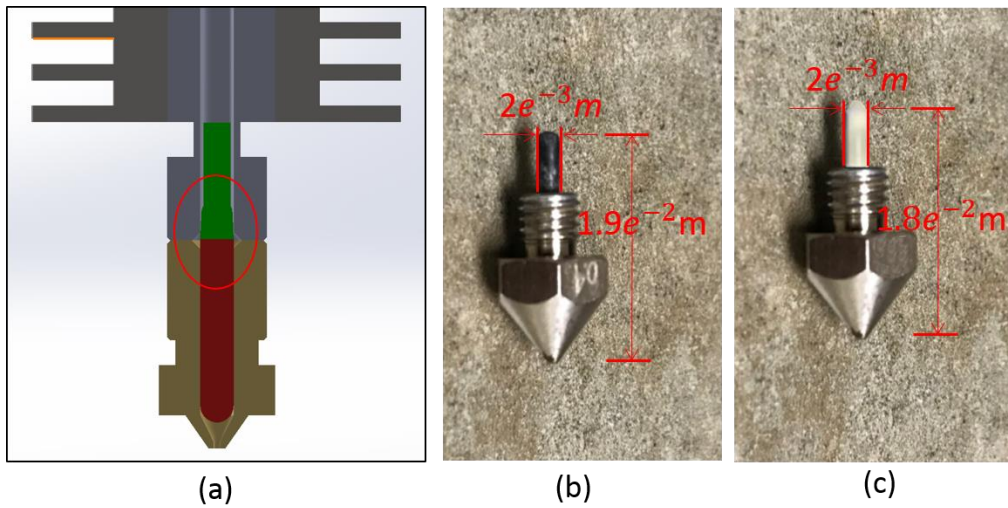


Figure 5-6 Hot end during processing (a) Schematic of melting line moves upward during processing; (b) Observed heat creeping for PLA at 215°C; (c) Observed heat creeping for neat ABS at 230°C.

Table 5-1 Inside dimensions of the nozzle (see e.g., Figure 5-1)

L_1	L_2	L_3	R_1	R_2
$1.47e^{-2} m$	$0.79e^{-3} m$	$0.50e^{-3} m$	$1.02e^{-3} m$	$0.20e^{-3} m$

As mentioned at beginning of this Chapter, the diameter of the capillary die in the nozzle also has the potential to be changed when the experiments in process. However, measurements of the changing of this parameter are impractical. Therefore, the simulation of the melting zone considering the varying parameters (i.e. L_1 and R_2) is implemented in MATLAB. L_1 is set varying from $1.07e^{-2} m$ to $2.57e^{-2} m$ with the increment of $1.0e^{-3} m$, and R_2 varies from $1.5e^{-4} m$ to $2.4e^{-4} m$. Secondly, the value of n and k corresponding to different L_1 and R_2 are predicted iteratively in MATLAB (the method used to predict n and k will be discussed in *Section 5.3*). The contours in *Figure 5-7 – 5-9* show how the prediction of pressure drop, the power-law index, and the consistency index changes if unexpected changing of L_1 and R_2 happened in processing. Notice the red cross in each figure represents the assumed condition of melting region which is the same as the nozzle inside geometry.

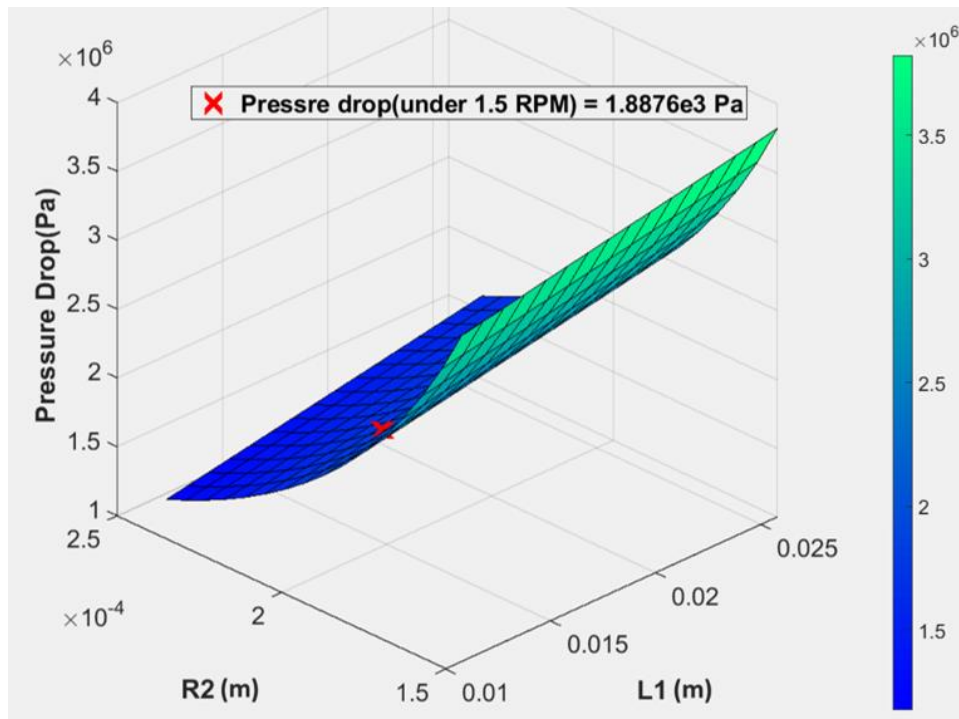


Figure 5-7 Effects of melting zone on prediction of pressure drop

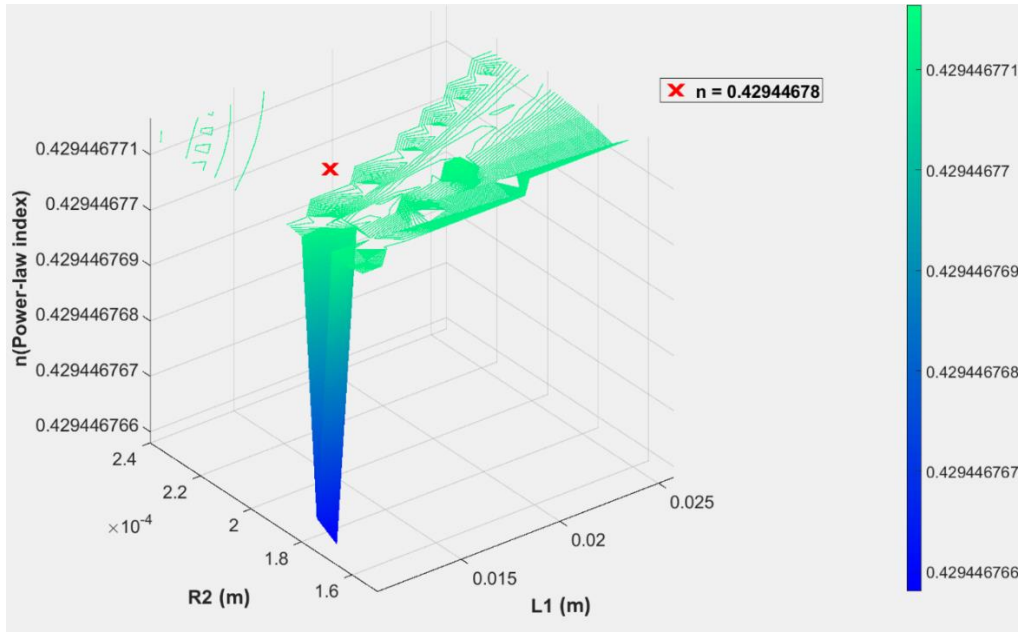


Figure 5-8 Changing of melting zone has negligible effect on prediction of Power Law index

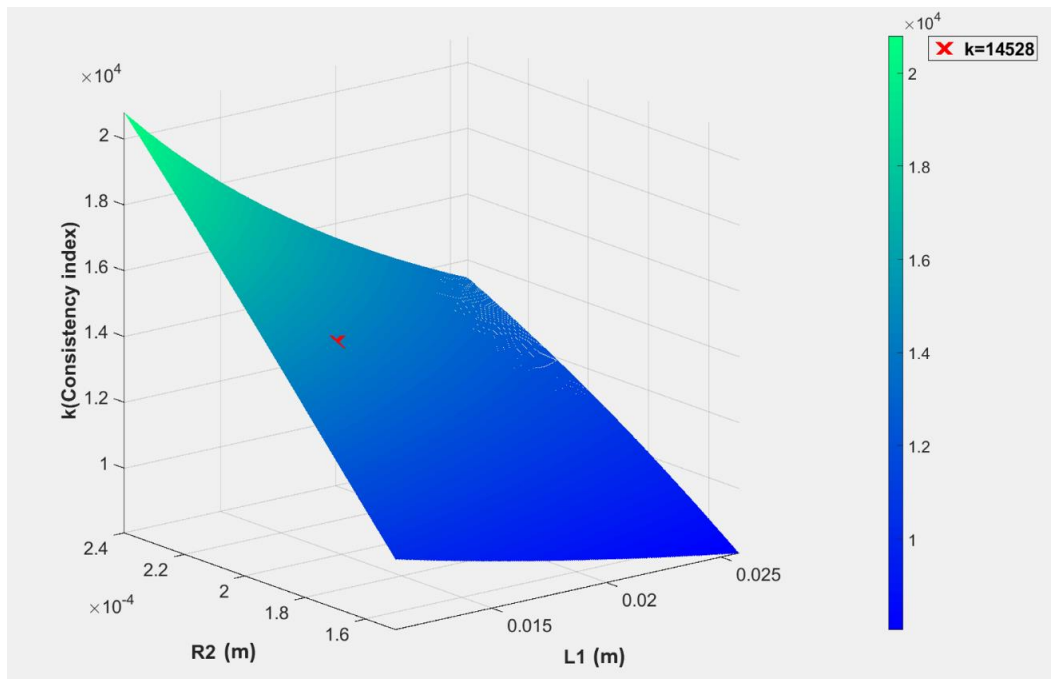


Figure 5-9 Effects of melting zone on prediction of the Consistency index

5.3 Nonlinear Least-Squares Regression

Equation 5.31 provides a function for pressure drop as a function of flow rate for a power law fluid model. It is a nonlinear function contains two unknowns n and k , which can be calculated from experimental data using an appropriate curve-fitting approach. Notice that the dependence of this math model on parameters (n and k) is also nonlinear. Therefore, a nonlinear regression approach is required and is applied in the discussion below to solve for n and k for each of the polymer and polymer composite filaments described above. We employ the Gauss-Newton method for this purpose.

Least-squares is a curve fitting strategy designed to reduce the overall residual errors between the original measured data and the approximated function by minimizing the sum of the squared error. In a general least squares procedure for fitting a set data pairs (x_i, y_i) , $i = 1, \dots, n$, where n is the number of data points used in the fitting process. We define the Sum of the Squared Residual S_r given as [95]

$$S_r = \sum_{i=1}^n (y_i - f(x_j))^2 \quad (5.33)$$

where y_i represents the component in vector $\{Y\}$ which contains the measured values of dependent variable, $f(x_i)$ is the expectation model function that is composed of the unknown coefficients and independent variable. If the function $f(x)$ is linear in the unknown coefficients, then $f(x_j)$ may be expressed as $\sum_{j=0}^m a_j k_{ji}$, where a_j are the coefficients and k_{ji} are the basis functions that exclude the coefficients which may be linear or nonlinear in x_j . In this case, the coefficients can be calculated with one step as:

$$\{A\} = \left[[K]^T [K] \right]^{-1} \{ [K]^T \{Y\} \} \quad (5.34)$$

where components of the matrix $[K]$ are the values of the basis function k_{ji} and the vector $\{A\}$ contains the unknown coefficients $a_j, j = 1, \dots, n$.

When the equation of interest $f(x)$ is nonlinear in the unknown coefficients, such as n and k in *Equation 5.31*, iterative techniques must be applied to obtain a solution. This thesis applies the Gauss-Newton [113] iterative method which is an efficient method commonly used to solve the nonlinear least-squares problem iteratively. Gauss-Newton method uses a first-order Taylor series to linearize the nonlinear equation. Assuming ordered pairs of data having the form (x_i, y_i) ($i = 1, 2, \dots, n$) are known, the value of the equation of interest at the points $x_i, i = 1, \dots, n$ is expressed as $y = f(x_i; a_0, a_1, \dots, a_m)$. Then the measured data y_i may be written in terms of the discrepancy e_i as

$$y_i = f(x_i; a_0, a_1, \dots, a_m) + e_i \quad (5.35)$$

Expanding *Equation 5.35* as a Taylor series about a known point, and truncating the second and other higher order derivatives gives

$$f(x_i)_j = f(x_i)_{j-1} + \frac{\partial f(x_i)}{\partial a_0} \Delta a_0 + \frac{\partial f(x_i)}{\partial a_1} \Delta a_1 + \dots + \frac{\partial f(x_i)}{\partial a_m} \Delta a_m, \quad (5.36)$$

$$j = 1, 2, 3, \dots$$

Substituting *Equation 5.36* into *Equation 5.35* yields a set of equations of the form

$$y_i - f(x_i)_j = \frac{\partial f(x_i)}{\partial a_0} \Delta a_0 + \frac{\partial f(x_i)}{\partial a_1} \Delta a_1 + \dots + \frac{\partial f(x_i)}{\partial a_m} \Delta a_m + e_i \quad (5.37)$$

which can be expressed as

$$\begin{bmatrix} y_1 - f(x_1) \\ y_2 - f(x_2) \\ \vdots \\ y_n - f(x_n) \end{bmatrix} = \begin{bmatrix} \frac{\partial f(x_1)}{\partial a_0} & \frac{\partial f(x_1)}{\partial a_1} & \dots & \frac{\partial f(x_1)}{\partial a_m} \\ \frac{\partial f(x_2)}{\partial a_0} & \frac{\partial f(x_2)}{\partial a_1} & \dots & \frac{\partial f(x_2)}{\partial a_m} \\ \vdots & \vdots & \dots & \vdots \\ \frac{\partial f(x_n)}{\partial a_0} & \frac{\partial f(x_n)}{\partial a_1} & \dots & \frac{\partial f(x_n)}{\partial a_m} \end{bmatrix} \begin{bmatrix} \Delta a_0 \\ \Delta a_1 \\ \vdots \\ \Delta a_m \end{bmatrix} + \begin{bmatrix} \Delta e_0 \\ \Delta e_1 \\ \vdots \\ \Delta e_m \end{bmatrix} \quad (5.38)$$

In the Least Square procedure, the error vector in *Equation 5.38* is zeroed and we define

$$Z = \begin{bmatrix} \frac{\partial f(x_1)}{\partial a_0} & \frac{\partial f(x_1)}{\partial a_1} & \dots & \frac{\partial f(x_1)}{\partial a_m} \\ \frac{\partial f(x_2)}{\partial a_0} & \frac{\partial f(x_2)}{\partial a_1} & \dots & \frac{\partial f(x_2)}{\partial a_m} \\ \vdots & \vdots & \dots & \vdots \\ \frac{\partial f(x_n)}{\partial a_0} & \frac{\partial f(x_n)}{\partial a_1} & \dots & \frac{\partial f(x_n)}{\partial a_m} \end{bmatrix},$$

$$dA = \begin{bmatrix} \Delta a_0 \\ \Delta a_1 \\ \vdots \\ \Delta a_m \end{bmatrix}$$

and

$$D = \begin{bmatrix} y_1 - f(x_1) \\ y_2 - f(x_2) \\ \vdots \\ y_n - f(x_n) \end{bmatrix}$$

It follows that *Equation 5.38* is written concisely as $[Z][dA] = [D]$, where Z is Jacobian, $\{dA\}$ is used to update the values of the coefficients in $\{A\}_j = \{A\}_{j-1} + \{dA\}$ based on the initial guess $\{A\}_0$. In each iteration, $\{dA\}$ can be calculated by multiplying the transpose of Jacobian then solve the system of equations, which is shown as

$$\{dA\} = \left[[Z]^T [Z] \right]^{-1} \{ [Z]^T \{D\} \} \quad (5.39)$$

The nonlinear least-squares regression in this research is implemented in MATLAB and used to determine values of n and k for each filament at certain experimental conditions using *Equation 5.31* as the model function. And the corresponding partial derivative of *Equation 5.31* with respect to k and n are respectively given as

$$\frac{\partial \Delta P}{\partial k} = \left(L_1 R_1^{-1-3n} + L_3 R_2^{-1-3n} + \frac{\cot\left[\frac{\beta}{2}\right](-R_1^{-3n} + R_2^{-3n})}{3n} \right) 2\pi^{-n} \left(\left(3 + \frac{1}{n}\right) Q \right)^n \quad (5.40)$$

$$\begin{aligned} \frac{\partial \Delta P}{\partial k} = \frac{2k\pi^{-n} \left(3 + \frac{1}{n}\right)^n Q^n R_1^{-3n}}{3(1+3n)} & \left\{ -\frac{3L_1}{R_1} (A + (3+9n) \ln(R_1)) \right. \\ & + \frac{R_2^{-1-3n}}{n^2} \left[-3n^2 (A + (3+9n) \ln(R_2)) L_3 R_1^{3n} + \cot\left(\frac{\beta}{2}\right) R_2 (-B \right. \\ & \left. \left. + 3n(1+3n) \ln(R_2)) R_1^{3n} + (B + 3n(1+3n) \ln(R_1)) R_2^{3n} \right] \right\} \end{aligned} \quad (5.41)$$

where A and B are given as

$$A = 1 + \ln(\pi) + 3n \ln(\pi) - (1+3n) \ln\left(\left(3 + \frac{1}{n}\right) Q\right) \quad (5.42)$$

$$B = 1 + n(4 + \ln(\pi) + 3n \ln(\pi)) - n(1+3n) \ln\left(\left(3 + \frac{1}{n}\right) Q\right) \quad (5.43)$$

A good initial guess does not only guarantee the convergence of the iteration but also reduces the number of iteration required to compute a solution. Again, the power law index n represents the slope of the viscosity as a function of shear strain rate curve in log-log space. Therefore the value of n must be within the range of 0 to 1 (note that $n = 1$ for

a Newtonian fluid). Generally, the value of power index for most polymers is between 0.2 and 0.7 ([112], [114]), and the consistency index always falls between $1e3$ and $1e5$ $\text{Pa} \cdot \text{s}^n$. Thus, we choose an initial guess as $n = 0.5$ and $k = 10000 \text{ Pa} \cdot \text{s}^n$. Data used to determine n and k with the Gauss-Newton method includes extrusion forces measured for various polymers or polymer composites at two different temperatures. Notice the higher temperature for each material is chosen according to the general printing processing temperature on a desktop 3D printer [115]. Furthermore, the lower temperature is picked as the reference group to assess the functionality of the low-cost device.

To assess the goodness of the least squares curve fitting results, the error between the measured data and the prediction data may be quantified using S_r and S_t . The sum of the squares S_r is described above, and the square of the residual S_t quantifies the discrepancy between real data and the central tendency or mean value of y_i and $y(x_i)$,

$$S_t = \sum (y_i - \bar{y})^2 \quad (5.44)$$

where $\bar{y} = \frac{\sum y_i}{n}$. The difference between S_r and S_t represents the error reduction of the regression. Normalizing this difference to S_t gives

$$r^2 = \frac{S_t - S_r}{S_t} \quad (5.45)$$

where r is the correlation coefficient, and r^2 is the coefficient of determination. In an ideal fit, $r^2 = 1$.

5.4 Comparison of Viscosity Curves

Before performing the nonlinear least-squares curve fitting procedure to solve for Power Law fluid parameters n and k for each of the filaments given in *Table 4-1*, a set of data of their pressure drop must be measured using the filament rheometer as the

variables to be fitted. The filament is thoroughly dried out in the oven, then the extrusion force for each filament is measured at the fixed temperature (the same as the measurements conducted using MARS 40) but varying the RPM of stepper motor from 0.5 RPM to 2.5 RPM with 0.5 RPM increment. The volume flow rate is also measured in this process. Repeat the above procedure for same material at the five speeds of stepper motor, five sets of extrusion force versus the volume flow rate data are measured. One example taking from 3DXTECH ABS at 210°C is given in *Figure 5-10* and *Table 5-2* where the corresponding pressure drop over and the average velocity of the flow at the nozzle entrance are calculated. Repeat the same measurements for all six materials, then a group of data of pressure drop are obtained.

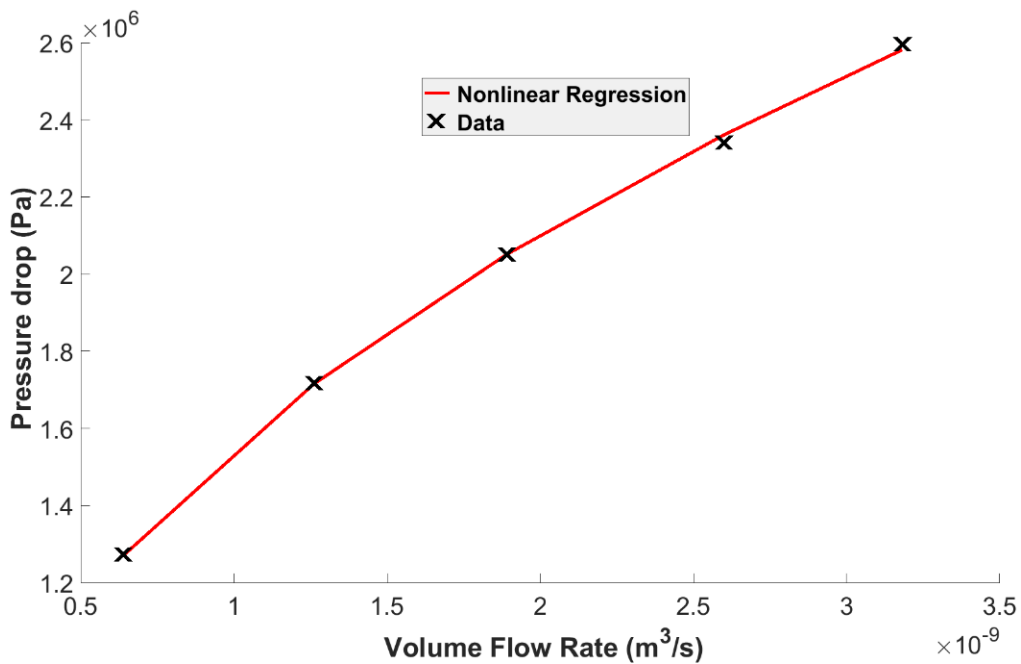


Figure 5-10 Curve fitting for the pressure drop versus volume flow rate data set of 3DXTECH ABS at 210°C

Having the volume flow rate data as the independent variable and the pressure drop as the independent variable, the Power Law parameters n and k in *Equation 5.31* are

curve-fitted using the Gauss Newton least-squares approach in MATLAB. The values of n , k , and the corresponding coefficient of determination r^2 are given in *Table 5-3*.

Once these parameters are known, the power-law model can be used to compute the viscosity as a function of shear rate with *Equation 5.31*. For the polymers and polymer composites considered here, we apply the Cox-Merz rule to obtain viscosity curves as a function of shear strain rate where data is obtained from MARS 40 rotational rheometer (cf. *Figure 4-31 and 4-32*) for each material as shown from *Figure 5-11 to 5-14*. As mentioned in *Chapter Two*, research by Guo [64] suggests that the Cox-Metz rule is invalid for short glass fiber filled suspension. However, we apply the Cox-merz rule here to our carbon fiber filled materials to assess the results obtained from MARS and our device, as shown in *Figure 5-15 and 5-16*. As mentioned in *Chapter Four* the viscosity measurements for same material under same experimental condition using MARS 40 exist some vertical or horizontal shift. Therefore, the viscosity curves from MARS 40 are plotted in the form of the average value along with the error. The circular markers are the average value of five measurements of the complex viscosity at the corresponding angular frequency.

Table 5-2 Pressure drop and volume flow rate measurements for 3DTECH ABS at 210°C at five stepper motor speed.

RPM	0.5	1	1.5	2	2.5
Extrusion Force $F(N)$	3.66	5.08	5.99	6.73	7.40
Pressure Drop D_p (Pa)	1.16E+06	1.62E+06	1.91E+06	2.14E+06	2.35E+06
Volume Flow Rate Q (m^3/s)	6.44E-10	1.28E-09	1.91E-09	2.54E-09	3.18E-09
Average velocity of flow at nozzle entrance \bar{v} (m/s)	2.05E-04	4.07E-04	6.07E-04	8.10E-04	1.01E-03

Table 5-3 Power Law GNF Curve-fitting results using Gauss Newton least-squares approach for all six materials at two different temperatures

Filaments	Temperature	n	k	r^2
3DXTECH-ABS	210°C	0.431	1.45E+04	0.9985
	230°C	0.501	6.68E+03	0.9990
3DXTECH-CFR-ABS	210°C	0.435	1.85E+04	0.9970
	230°C	0.502	8.12E+03	0.9980
TRIPTECH-ABS	210°C	0.353	2.33E+04	0.9997
	230°C	0.425	1.22E+04	0.9971
TRIPTECH-Amphora	210°C	0.570	1.72E+04	0.9998
	230°C	0.682	6.22E+03	0.9976
TRIPTECH-PLA	195°C	0.606	6.74E+03	0.9824
	215°C	0.688	2.88E+03	0.9975
Proto-Pasta-CFR-PLA	195°C	0.671	4.52E+03	0.9979
	215°C	0.764	1.52E+03	0.9938

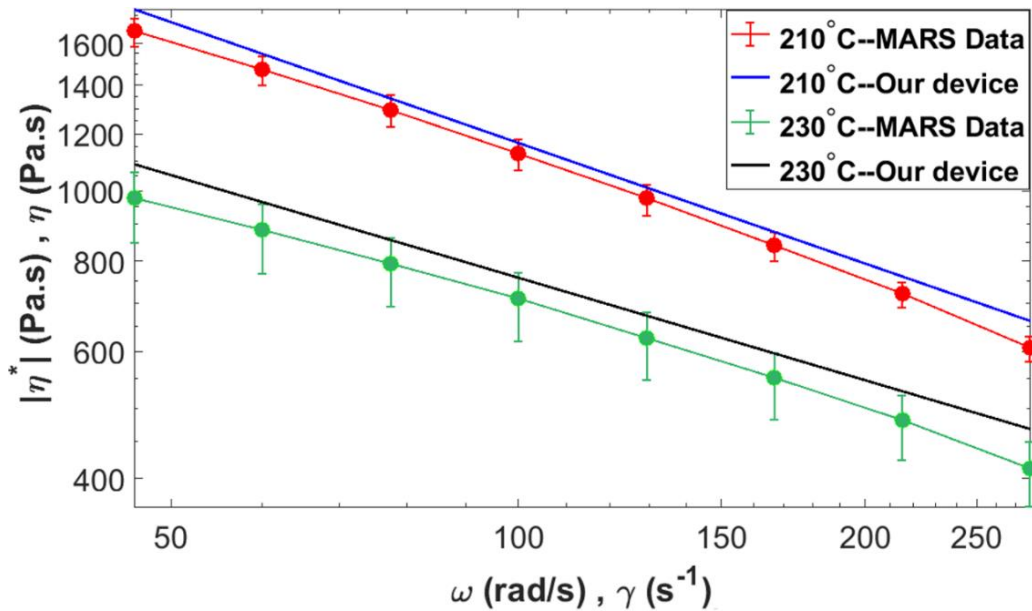


Figure 5-11 Viscosity as a function of strain rate using the Cox-Merz rule for 3DXTECH ABS. Comparison of data obtained from the MARS 40 and the FFF filament rheometer.

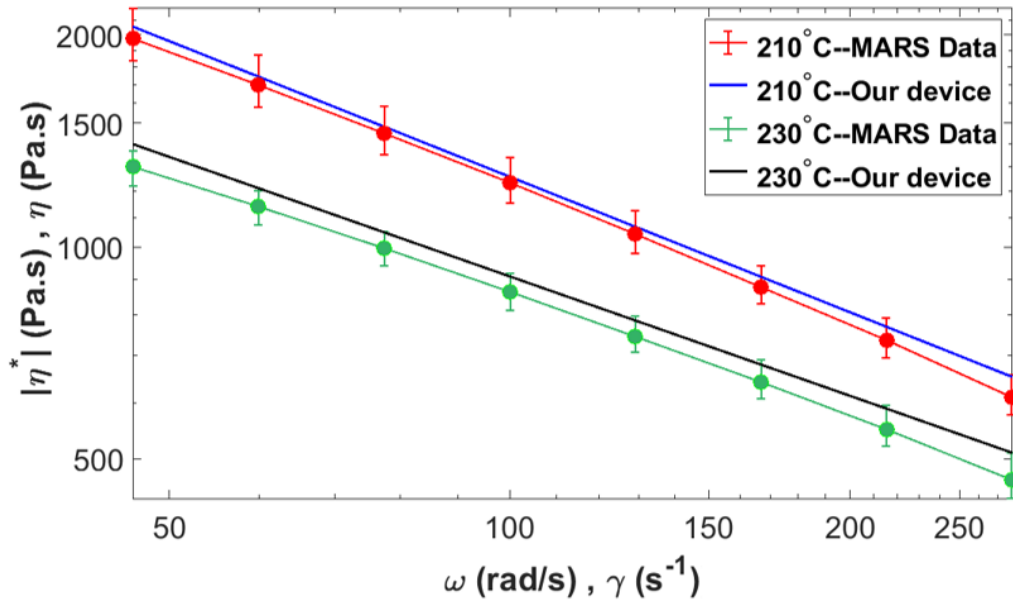


Figure 5-12 Viscosity as a function of strain rate using the Cox-Merz rule for TRIPTECH ABS. Comparison of data obtained from the MARS 40 and the FFF filament rheometer.

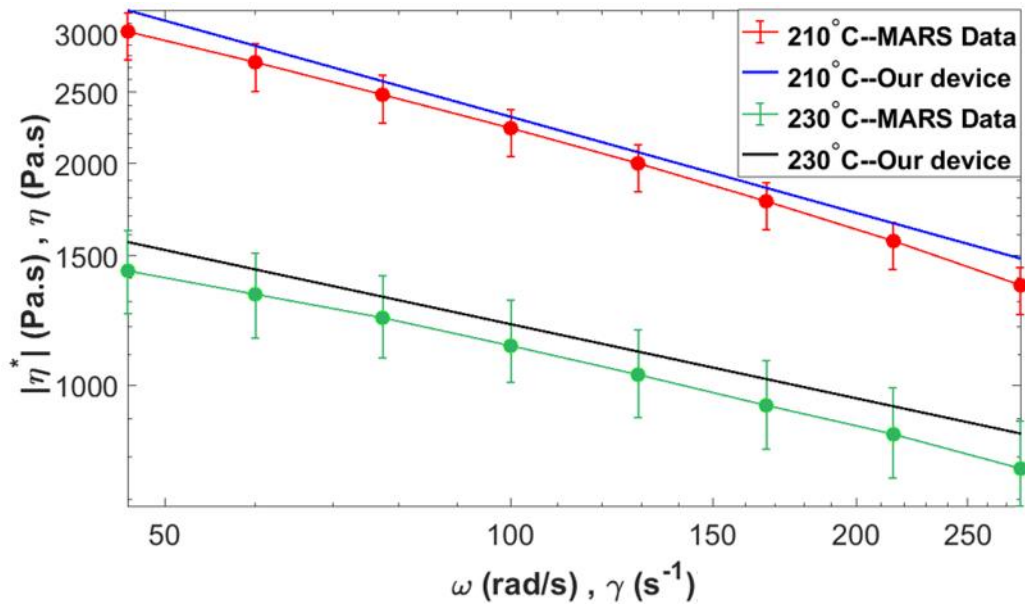


Figure 5-13 Viscosity as a function of strain rate using the Cox-Merz rule for TRIPTECH Amphora. Comparison of data obtained from the MARS 40 and the FFF filament rheometer

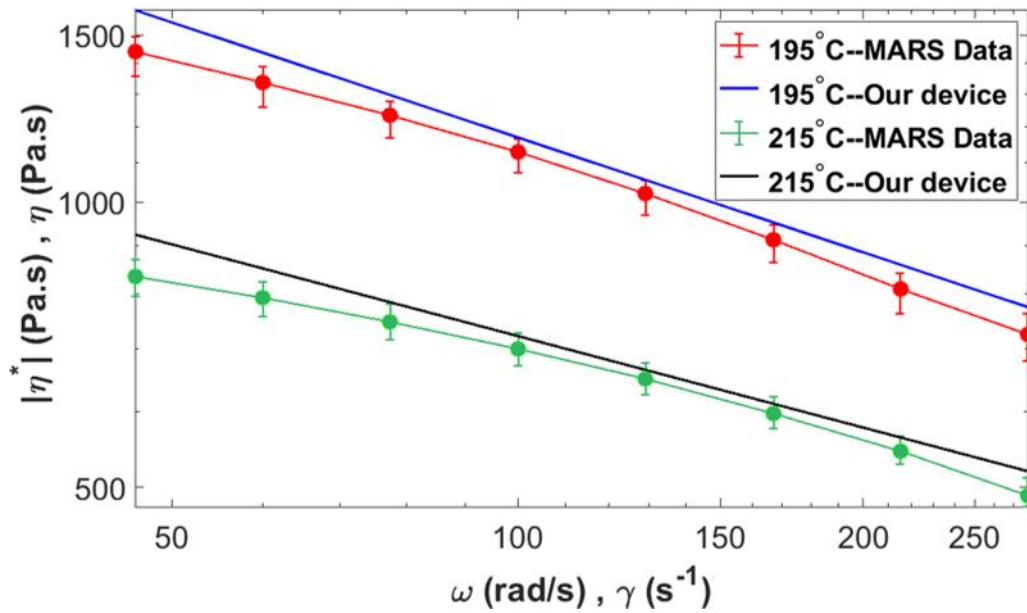


Figure 5-14 Viscosity as a function of strain rate using the Cox-Merz rule for TRIPTECH PLA. Comparison of data obtained from the MARS 40 and the FFF filament rheometer.

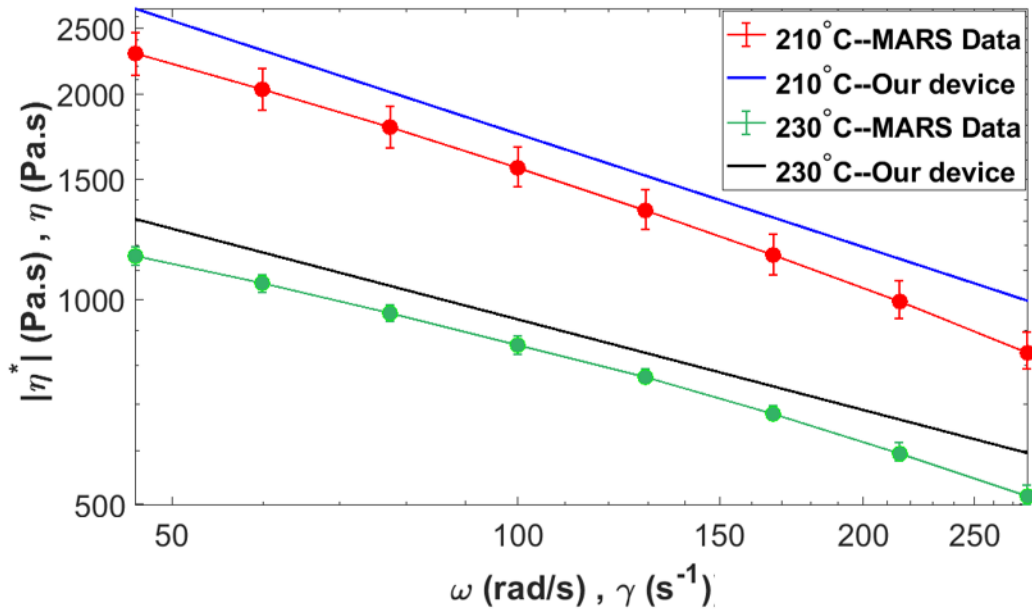


Figure 5-15 Viscosity as a function of strain rate using the Cox-Merz rule for 3DXTECH CFR-ABS. Comparison of data obtained from the MARS 40 and the FFF filament rheometer

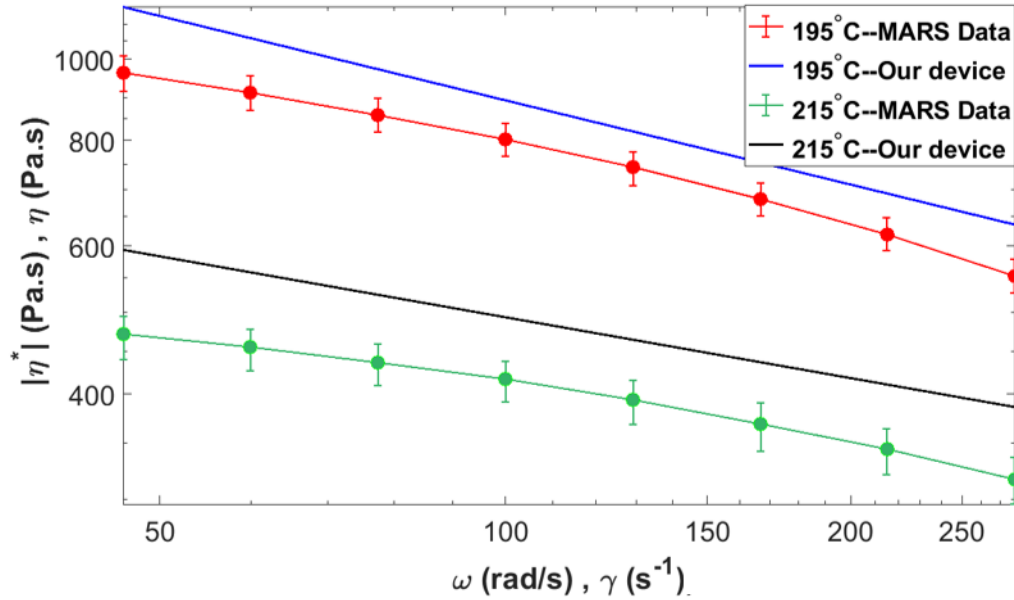


Figure 5-16 Viscosity as a function of strain rate using the Cox-Merz rule for MatterHackers CFR- PLA. Comparison of data obtained from the MARS 40 and the FFF filament rheometer

It is observed that the new method by correlating the new-designed device and the power-law pressure drop model is capable of predicting the shear rate dependent viscosity for pure polymers from accurately. However, the predicted viscosity curves for the carbon fiber reinforced materials have a bit off to the curves from MARS. Notice that, though the prediction of the consistency index for the carbon fiber reinforced polymer composites has discrepancy to what is measured using the rotational rheometer, the Power-law index has relatively high agreements to each other.

Theoretically, the observed discrepancies of the predicted rheological property of the carbon fiber filled polymer composites are mainly due to the different behaviors of fibers in different flow motion. According to Mutel's study [116,117], it is reasonable to assume that the fibers will maintain the original randomly orientated state under the small deformation in oscillation test. The viscosity of polymer composites have randomly

orientated fibers are higher than the same ones with aligned fibers [116]. It should be noted that, this comparison is between the professional rheometers with different measuring techniques. But the observed discrepancies in our study is different as compared to the general phenomena in which the complex viscosity should be higher than the viscosity measured from capillary rheometer. Therefore, it gains specific importance to explain. For the low-cost device the ratio of the length and the diameter of the capillary die is fairly small regarding to the one in a capillary rheometer, which means the flow in it is not fully developed. Therefore, the results observed in *Figure 5-15 and 5-16* could be explained according to the study in [117], that is the changing in fiber orientation of fiber-filled polymer melts under shear process leads to a manifest increase of shear stress before reaching a steady state (i.e., fibers are aligned). Apparently, the increasing shear stress will give rise to a higher pressure drop measurement in such a processing approach, which ultimately leads to the discrepancies of the predicted viscosity curve. It is also noticed that the discrepancies of the consistency index for 3DTECH CFR-ABS is smaller than MatterHackers CFR-PLA. This probably because the fiber concentration of MatterHackers CFR-PLA is higher than the 3DTECH CFR-ABS's. Another potential reason could be the different of the aspect ratio of carbon fibers of these two materials.

Having the discrepancy information graphically, it is natural to move forward to conduct the error analysis between the prediction and the real data. Some efforts are made to assess the error. However, it is practically hard to set the criterion to quantify it. Firstly, there has no strict restrictions of the shear rate region been defined for power-law model in the published paper yet. The predicted values of power-law parameters highly

depend on the objective shear rate region. Taking the curve fitting of data for 3DXTECH ABS at 210°C as the example, the difference of the power-law parameters over different shear rate interval is shown in *Table 5-4*. It is noticed that, a slightly change in the objective shear rate region will generate a significant error of the prediction of power-law parameters.

Table 5-4 Effects of choosing shear rate interval for Power-law model on the curve-fitted values of n and k

3DXTECH ABS at 210°C	n	k
$\omega(3e^1 - 2e^2 \text{ rad/s})$	0.4781	1.2321e+04
$\omega(4e^1 - 2e^2 \text{ rad/s})$	0.4700	1.2792e+04
Error	1.69%	3.68%

Furthermore, even conducting the tests carefully for the same material under same experimental condition using the professional rheometer one can still get the viscosity curves that different to each other. Considering the viscosity curves for 3DXTECH ABS at 210°C in *Figure 4-30*. If the objective interval of angular frequency for power-law model is picked from 40 to 200 (rad/s) the deviation of the consistency index of between the second and the fourth test is about 19.8% off. For the highly close tests (the first and the sixth test) the error is still up to 2%.

Having the above analysis as the premise, the power-law parameters that are predicted from our device (i.e. *Table 5-3*) and from MARS (i.e. *Table 4-7*) is compared in *Table 5-5 and 5-6* quantitatively. Two preconditions must be mentioned. Firstly, the power-law parameters from MARS are curve-fitted with the angular frequency interval that is from 50 rad/s to 280 rad/s. This interval is chosen not only based on the published

data for ABS and PLA in [118],[119],[120] but also for obtaining the highly agreement to the predicted power law parameters using our device. Secondly, the curve-fitted data from MARS are chosen from the one of the data that have highly agreement to each other (e.g., any data from the first or the sixth measurement in *Figure 4-30*).

Table 5-5 Comparison of the predicted power-law index (n) between the low-cost device to the MARS 40 rotational rheometer

Filaments	Temperature(°C)	Filament Rheometer n	MARS 40 n	Error (%)
3DXTECH	210	0.431	0.424	1.6
ABS	230	0.501	0.507	1.7
3DXTECH CFR-ABS	210	0.435	0.420	3.6
	230	0.502	0.530	5.2
Triptech Plastic	210	0.353	0.334	5.6
ABS	230	0.425	0.418	1.5
Triptech Plastic	210	0.570	0.546	4.3
Amphora	230	0.682	0.650	5.1
3DXTECH	195	0.606	0.601	1.9
PLA	215	0.688	0.695	1.8
MatterHackers	195	0.671	0.679	1.1
CFR-PLA	215	0.764	0.777	1.7

Table 5-6 Comparison of the predicted power-law consistency index ($k \text{ Pa} \cdot \text{s}^n$) between the low-cost device to the rotational rheometer

Filaments	Temperature(°C)	Filament Rheometer k	Mars 40 k	Error (%)
3DXTECH	210	1.45E+04	1.59E+04	8.8
ABS	230	6.68E+03	7.04E+03	5.0
3DXTECH CFR-ABS	210	1.85E+04	2.25E+04	10.4
	230	8.12E+03	7.49E+03	8.4
Triptech Plastic	210	2.33E+04	2.52E+04	7.5
ABS	230	1.22E+04	1.28E+04	2.5
Triptech Plastic	210	1.72E+04	1.83E+04	6.0
Amphora	230	6.22E+03	5.89E+03	5.6
3DXTECH	195	6.74E+03	7.18 E+03	6.1
PLA	215	2.88E+03	3.02E+03	4.6
MatterHackers	195	4.52E+03	3.89E+03	16.3
CFR-PLA	215	1.52E+03	1.33E+03	14.7

CHAPTER SIX

Conclusions and Future Work

6.1 Conclusions

A thorough understanding of the flow behavior and properties of polymer melts in Fused Filament Fabrication processes is of central importance for studies focusing on the process optimization and mechanical properties improvement of the printings.

Rheological properties of interest include the shear rate dependent viscosity, the storage and loss modulus, and the stress relaxation time. Polymers used in FFF printers exhibit shear-thinning behavior which is known to benefit polymer extrusion. Both capillary and the rotational rheometers are commonly used to measure rheological properties of polymers but are expensive and require a trained technician for their operation.

Therefore, a method is needed that allows FFF users to directly obtain rheological data for their filament of choice.

This thesis develops filament rheometer which is composed of a device and computational approach that directly characterizes the rheological properties of FFF filament. Firstly, a device was fabricated that measures the extrusion force within FFF filament. The extrusion force is used to propose a FFF Filament Melt Index which is analogous to the Melt Flow Index that can be used to characterize the filament. Secondly, a model for pressure drop model as a function of volumetric flow rate was developed where the polymer melt was assumed to be a Power Law GNF fluid. Thirdly, the pressure drop was measured at a specified temperature and temperature at five different

volumetric flow rates. This data was used to obtain Power Law parameters with a curve-fitting algorithm in MATLAB. The predicted shear rate dependent viscosity was validated with rheological measurements obtained with a MARS 40 rotational rheometer.

Several efforts were made to minimize the measurement error of the filament rheometer. For the beam load cell, the effects from the temperature and bending moment on the force measurement were shown to be negligible when measuring the filament force acting on the liquefier. For the extruder, vibration from start and stop of each step of the stepper motor was minimized by subdividing each step into 32 micro-steps. In addition, the speed of the stepper motor was verified to be accurate and directly related to volumetric flow rate experimentally. Extensive work was done to ensure that the temperature in the nozzle accurate as shown in *Figure 3-34* and *Table 3-4*. In the end, the force signal in *Figure 4-14 – 4-19* demonstrated repeatability of the measurements using our device.

Experiments using our filament rheometer were conducted for six commercially available filaments that are commonly used in FFF printers. This included pure polymers and carbon fiber reinforced polymer composites. The rheological properties of each filament were evaluated at two different temperatures, with one being a common print temperature. A second slightly lower temperature was included to verifying the function of our filament rheometer on assessing same filament at different temperature.

Comparison results between the measured viscosity using our device to those obtained with a rotational rheometer in *Table 5-5* and *5-6* shows that power law index can be obtained within 6% of measured values for all polymer and polymer composites

tested using our device. Consistency index estimates are mostly within 10% with the exception of one fiber filled polymer composite which shows less accuracy.

In summary, this research fabricated a low-cost device to allow people to measure the extrusion force and volumetric flow rate in a FFF process. The filament rheometer developed here is shown to be an effective way to quickly characterize the rheology of FFF filaments. The method presented in this study can accurately predict the Power Law parameters including the power law index and consistency index of thermoplastics used in FFF. Results show a high level of accuracy when predicting the power law index, however, the device was much more effective at predicting the consistency of neat polymer filament than it was for short fiber composite filament.

6.2 Future Work

According to the current findings of this work, there are several options for the future studies based on our device:

- Improve the filament feeding mechanism to provide for a smoother filament delivery and improved filament force measurement.
- Modify the nozzle by increasing the diameter of the capillary die to allow for an extended range of shear rate measurement. By considering lower shear rates, the Carreau-Yasuda model could be implemented, allowing the filament rheometer to be used to compute the zero viscosity of filament.
- In addition, by further modify the nozzle capillary geometry, the Bagley correction could be evaluated for FFF nozzle flow. By customizing the nozzle used on our device, it would be possible to measure the die swell pressure with different ratios of L/D .
- Modify the filament rheometer to accept 2.85mm filament.
- Consider the contribution of extensional flow in the nozzle contraction region when evaluating total pressure drop in the FFF nozzle.

- Use the filament rheometer to evaluate the pressure drop occurring during polymer bead deposition.
- Develop a detailed finite element model of the nozzle fluid flow and polymer temperature during the FFF process. This model could then be used in and inverse analysis to obtain polymer melt flow properties.
- Transfer the technology presented in this thesis to a small portable device that could be commercialized.

The low-cost filament rheometer has the potential to provide a better understanding of the flow properties of polymer and polymer composites in FFF. The future studies suggested here will help to lay a solid foundation for improving the FFF technology.

BIBLIOGRAPHY

- [1] A. Gold, S., Strong, R., and N. Turner, B., 2014, “A Review of Melt Extrusion Additive Manufacturing Processes: I. Process Design and Modeling,” *Rapid Prototyp. J.*, **20**(3), pp. 192–204.
- [2] Shahriar, B. B., France, C., Valerie, N., Arthur, C., and Christian, G., 2017, “Toward Improvement of the Properties of Parts Manufactured by FFF (Fused Filament Fabrication) through Understanding the Influence of Temperature and Rheological Behaviour on the Coalescence Phenomenon,” *AIP Conf. Proc.*, **1896**(1), p. 040008.
- [3] Huang, S. H., Liu, P., Mokasdar, A., and Hou, L., 2013, “Additive Manufacturing and Its Societal Impact: A Literature Review,” *Int. J. Adv. Manuf. Technol.*, **67**(5), pp. 1191–1203.
- [4] Badiru, A. B., Valencia, V. V., and Liu, D., 2017, *Additive Manufacturing Handbook: Product Development for the Defense Industry*, CRC Press.
- [5] Chua, C. K., Leong, K. F., and Lim, C. S., 2003, *Rapid Prototyping: Principles and Applications (with Companion CD-ROM)*, 2nd Edition, World Scientific Publishing Company.
- [6] Gao, W., Zhang, Y., Ramanujan, D., Ramani, K., Chen, Y., Williams, C. B., Wang, C. C. L., Shin, Y. C., Zhang, S., and Zavattieri, P. D., 2015, “The Status, Challenges, and Future of Additive Manufacturing in Engineering,” *Comput.-Aided Des.*, **69**, pp. 65–89.
- [7] Wohlers, T. T., and Caffrey, T., 2014, *Wohlers Report 2014: 3D Printing and Additive Manufacturing State of the Industry Annual Worldwide Progress Report*, Wohlers Associates, Fort Collins, Col.
- [8] Columbus, L. 2015 Roundup of 3D Printing Market Forecasts and Estimates. Available online: <http://www.forbes.com/sites/louiscolumbus/2015/03/31/2015-roundup-of-3d-printing-market-forecasts-and-estimates> (accessed on 29 June 2016).
- [9] L.A. Verhoef, B.W. Budde, C. Chockalingam, B.G. Nodar, Ad, J.M. van Wijk, “The effect of additive manufacturing on global energy demand: an assessment using a bottom-up approach,” *Energy Policy*, 112 (2018), pp. 349-360.

- [10] Mohsen Attaran, "The rise of 3-D printing: The advantages of additive manufacturing over traditional manufacturing," *Business Horizons*, Volume 60, Issue 5, 2017, Pages 677-688, ISSN 0007-6813,
- [11] Talagani, M. R., DorMohammadi, S., Dutton, R., Godines, C., Baid, H., and Abdi, F., 2015, "Numerical Simulation of Big Area Additive Manufacturing (3D Printing) of a Full Size Car," *SAMPE J.*, **51**(4), p. 11.
- [12] Wang, T.-M., Xi, J.-T., and Jin, Y., 2007, "A Model Research for Prototype Warp Deformation in the FDM Process," *Int. J. Adv. Manuf. Technol.*, **33**(11), pp. 1087–1096.
- [13] M.H. Khaliq, R. Gomes, C. Fernandes, J. Nobrega, O.S. Carneiro, L.L. Ferras "On the use of high viscosity polymers in the fused filament fabrication process," *Rapid Prototyp. J.*, 23 (4) (2017), pp. 727-735
- [14] L. Wang, W.M. Gramlich, D.J. Gardner "Improving the impact strength of Poly(lactic acid) (PLA) in fused layer modeling (FLM) Polymer," 114 (2017), pp. 242-248
- [15] Berretta, S., Davies, R., Shyng, Y. T., Wang, Y., and Ghita, O., 2017, "Fused Deposition Modelling of High Temperature Polymers: Exploring CNT PEEK Composites," *Polym. Test.*, **63**, pp. 251–262.
- [16] Novakova-Marcincinova, L., and Kuric, I., "Basic and Advanced Materials for Fused Deposition Modeling Rapid Prototyping Technology," p. 4.
- [17] Wu, W., Geng, P., Li, G., Zhao, D., Zhang, H., Zhao, J., Wu, W., Geng, P., Li, G., Zhao, D., Zhang, H., and Zhao, J., 2015, "Influence of Layer Thickness and Raster Angle on the Mechanical Properties of 3D-Printed PEEK and a Comparative Mechanical Study between PEEK and ABS," *Materials*, **8**(9), pp. 5834–5846.
- [18] Karsli, N. G., and Aytac, A., 2013, "Tensile and Thermomechanical Properties of Short Carbon Fiber Reinforced Polyamide 6 Composites," *Compos. Part B Eng.*, **51**, pp. 270–275.
- [19] Ning, F., Cong, W., Qiu, J., Wei, J., and Wang, S., 2015, "Additive Manufacturing of Carbon Fiber Reinforced Thermoplastic Composites Using Fused Deposition Modeling," *Compos. Part B Eng.*, **80**, pp. 369–378.
- [20] C. Duty, V. Kunc, B. Compton, B. Post, D. Erdman, R. Smith, et al. Structure and mechanical behavior of big area additive manufacturing (BAAM) materials *Rapid Prototyp. J.*, 23 (2017)

- [21] Brenken, B., Barocio, E., Favaloro, A., Kunc, V., and Pipes, R. B., 2018, "Fused Filament Fabrication of Fiber-Reinforced Polymers: A Review," *Addit. Manuf.*, **21**, pp. 1–16.
- [22] W. Hao, Y. Liu, H. Zhou, H. Chen, D. Fang "Preparation and characterization of 3D printed continuous carbon fiber reinforced thermosetting composites," *Polym Test*, 65 (2018), pp. 29-34
- [23] Bird, R. B., Armstrong, R. C., and Hassager, O., 1987, "Dynamics of Polymeric Liquids. Vol. 1, 2nd Ed.: Fluid Mechanics."
- [24] Dechant, J., 1990, "Polymer Handbook. 3rd Edition. J. BRANDRUP and E. H. IMMERGUT (Editors). ISBN 0-471-81244-7. New York/Chichester/Brisbane/Toronto/Singapore: John Wiley & Sons 1989. Cloth Bond, ca. 1850 Pages, £ 115.00, \$175.00," *Acta Polym.*, 41(6), pp. 361–362.
- [25] Krevelen, D. W. van, 2012, *Properties of Polymers*, Elsevier.
- [26] Scott, C. E. "PolymerProcessing,". <http://www.polymerprocessing.com/>
- [27] Nam, S., 1987, "Mechanism of Fluoroelastomer Processing Aid in Extrusion of LLDPE," *Int. Polym. Process.*, **1**(2), pp. 98–101.
- [28] Hatzikiriakos, S. G., and Dealy, J. M., 1993, "Effects of Interfacial Conditions on Wall Slip and Sharkskin Melt Fracture of HDPE," *Int. Polym. Process.*, **8**(1), pp. 36–43.
- [29] C. L. M. H. Navier, "Mémoire Sur Les Lois Du Mouvement Des Fluides - Wikisource" *Mem. Acad. Sci. Inst. Fr.*, Vol. 6 (1823), pp. 389-416 Key: citeulike:5061179
- [30] M.K. Agarwala, V.R. Jamalabad, N.A. Langrana, A. Safari, P.J. Whalen, S.C. Danforth Structural quality of parts processed by fused deposition Rapid Prototyping J, 2 (4) (1996), pp. 4-19
- [31] Cogswell, F. N., 1972, "Converging Flow of Polymer Melts in Extrusion Dies," *Polym. Eng. Sci.*, **12**(1), pp. 64–73.
- [32] Kwon, T. H., Shen, S. F., and Wang, K. K., 1986, "Pressure Drop of Polymeric Melts in Conical Converging Flow: Experiments and Predictions," *Polym. Eng. Sci.*, **26**(3), pp. 214–224.
- [33] Boles, R. L., Davis, H. L. and Bogue, D. C. (1970), Entrance flows of polymeric materials: Pressure drop and flow patterns. *Polym Eng Sci*, 10: 24-31. doi:10.1002/pen.760100106.

- [34] Kwon, T. H., Shen, S. F., and Wang, K. K., 1986, "Pressure Drop of Polymeric Melts in Conical Converging Flow: Experiments and Predictions," *Polym. Eng. Sci.*, **26**(3), pp. 214–224.
- [35] Phan, D. D., Swain, Z. R., and Mackay, M. E., 2018, "Rheological and Heat Transfer Effects in Fused Filament Fabrication," *J. Rheol.*, **62**(5), pp. 1097–1107.
- [36] Bellini, A., Güçeri, S., and Bertoldi, M., 2004, "Liquefier Dynamics in Fused Deposition," *J. Manuf. Sci. Eng.*, **126**(2), pp. 237–246.
- [37] Ramanath, H. S., Chua, C. K., Leong, K. F., and Shah, K. D., 2008, "Melt Flow Behaviour of Poly-Epsilon-Caprolactone in Fused Deposition Modelling," *J. Mater. Sci. Mater. Med.*, **19**(7), pp. 2541–2550.
- [38] Sukindar, N. A., Mohd ariffin, M. khairol anuar, Baharudin, B. T., Nor Aiza Jaafar, C., and Ismail, M. I. S., 2016, "Analyzing the Effect of Nozzle Diameter in Fused Deposition Modeling for Extruding Polylactic Acid Using Open Source 3D Printing," *J. Teknol.*, **78**.
- [39] Pandey, A., and Pradhan, S. K., 2018, "Investigations into Complete Liquefier Dynamics and Optimization of Process Parameters for Fused Deposition Modeling," *Mater. Today Proc.*, **5**(5, Part 2), pp. 12940–12955.
- [40] Tlegenov, Y., Hong, G. S., and Lu, W. F., 2018, "Nozzle Condition Monitoring in 3D Printing," *Robot. Comput.-Integr. Manuf.*, **54**, pp. 45–55.
- [41] Dealy, J. M., and Wang, J., 2013, *Melt Rheology and Its Applications in the Plastics Industry*, Springer Netherlands.
- [42] J.M. Dealy, J. Wang "Melt Rheology and its Applications in the Plastics Industry (second ed.)," Springer, Dordrecht (2013).
- [43] Wagner, N. J., and Brady, J. F., "Shear Thickening in Colloidal Dispersions," p. 6.
- [44] Arrhenius, S., 1917, "The Viscosity of Solutions," *Biochem. J.*, **11**(2), pp. 112–133.
- [45] Barus, C., 1893, "Isothermals, Isopiestic and Isometrics Relative to Viscosity," *Am. J. Sci.*, **Series 3 Vol. 45**(266), pp. 87–96.
- [46] Dao, T. T., Ye, A. X., Shaito, A. A., Roye, N., & Hedman, K. (Outubro de 2009). "Capillary Rheometry: Analysis of Low-Viscosity Fluids, and Viscous Liquids and Melts at High Shear Rates," American Laboratory. Obtido de ATS RheoSystems.

- [47] Salas-Bringas, C., Lekang, O.-I., Rukke, E. O., and Schüller, R. B., “Development of a New Capillary Rheometer That Uses Direct Pressure Measurements in the Capillary,” p. 9.
- [48] Malvern Panalytical Rosand RH2000 Capillary Rheometer, www.malvernpanalytical.com/en/products/product-range/rosand-range/rosand-rh2000.
- [49] Van Puyvelde, P., Vananroye, A., Hanot, A.-S., Dees, M., Mangnus, M., and Hermans, N., 2013, “On the Pressure Dependency of the Bagley Correction,” *Int. Polym. Process.*, **28**, pp. 558–564.
- [50] U. Bröckel, W. Meier, G. Wagner “Product Design and Engineering: Formulation of Gels and Pastes,” John Wiley & Sons (2013)
- [51] Meyer, F., and Crawford, N., “Optimizing Process Conditions and Ensuring End Product Requirements of Plastics with Rheological Analysis,” p. 7.
- [52] Osswald, T. A., and Rudolph, N., 2015, *Polymer Rheology: Fundamentals and Applications*, Hanser Publications.
- [53] Grün, F., 1954, “Mathematical Structure of the Theories of Viscoelasticity. BERNHARD GROSS Hermann & Cie, Paris, 1953. 74 Pp., 600 Francs,” *J. Polym. Sci.*, **13**(69), pp. 319–319.
- [54] Meyer, F., “Performing Rheological Tests in Oscillation with the Thermo Scientific HAAKE Viscotester IQ Rheometer,” p. 6.
- [55] Collyer, A.A. and Clegg, D.W. (eds), “Rheological Measurement,” Elsevier, London, 1988 (647pp)
- [56] Cox, W., and Merz, E., 1959, “Rheology of Polymer Melts—A Correlation of Dynamic and Steady Flow Measurements,” *Int. Symp. Plast. Test. Stand.*
- [57] Barnes, H. A., Hutton, J. F., and Walters, K., 1989, *An Introduction to Rheology*, Elsevier.
- [58] C.W. Macosko *Rheology, principles, measurements and applications* VCH, NY (1994).
- [59] Milner, S. T., 1996, “Relating the Shear-thinning Curve to the Molecular Weight Distribution in Linear Polymer Melts,” *J. Rheol.*, **40**(2), pp. 303–315.

- [60] Al-Hadithi, T. S. R., Barnes, H. A., and Walters, K., 1992, “The Relationship between the Linear (Oscillatory) and Nonlinear (Steady-State) Flow Properties of a Series of Polymer and Colloidal Systems,” *Colloid Polym. Sci.*, **270**(1), pp. 40–46.
- [61] John M. Dealy, Daniel J. Read, Ronald G. Larson, “Structure and Rheology of Molten Polymers,” Hanser, 2018, ISBN 9781569906118.
- [62] Snijkers, F., and Vlassopoulos, D., 2014, “Appraisal of the Cox-Merz Rule for Well-Characterized Entangled Linear and Branched Polymers,” *Rheol. Acta*, **53**(12), pp. 935–946.
- [63] Aoki, Y., 1987, “Dynamic Viscoelastic Properties of ABS Polymers in the Molten State. 5. Effect of Grafting Degree,” *Macromolecules*, **20**(9), pp. 2208–2213.
- [64] Guo, R., Azaiez, J., and Bellehumeur, C., 2005, “Rheology of Fiber Filled Polymer Melts: Role of Fiber-Fiber Interactions and Polymer-Fiber Coupling,” *Polym. Eng. Sci.*, **45**(3), pp. 385–399.
- [65] N. Turner, B., Strong, R., and A. Gold, S., 2014, “A Review of Melt Extrusion Additive Manufacturing Processes: I. Process Design and Modeling,” *Rapid Prototyp. J.*, **20**(3), pp. 192–204.
- [66] Flores, J., “Stepper Motor Basics,” p. 44.
- [67] Hu, X., “An Introduction to Stepper Motors,” p. 7.
- [68] Thomas Annet, 2017, “Thermal analysis of a 3D printer Hot End,” <http://thomasannet.wixsite.com/portfolio/thermal-analysis-hotend>.
- [69] Jerez-Mesa, R., Gomez-Gras, G., Travieso-Rodriguez, J. A., and Garcia-Plana, V., 2017, “A Comparative Study of the Thermal Behavior of Three Different 3D Printer Liquefiers,” *Mechatronics*.
- [70] Dunn, B., and LLC, B. T. C., “Load Cells — Introduction and Applications — White Paper,” p. 11.
- [71] “Load Cell Amplifier and 24-Bit ADC Module - HX711,” Art Circuits [Online]. Available: <http://artofcircuits.com/product/load-cell-amplifier-and-24-bit-adc-module-hx711>. [Accessed: 01-Apr-2018].
- [72] “Arduino - Introduction”, <https://www.arduino.cc/en/Guide/Introduction>.
- [73] “Arduino - Software”, <https://www.arduino.cc/en/Main/Software>.
- [74] “Arduino Uno Rev3”, <https://store.arduino.cc/usa/arduino-uno-rev3>.

- [75] “Arduino Due”, <https://store.arduino.cc/usa/arduino-due>.
- [76] “Data Acquisition Fundamentals: Making Accurate Temperature Measurements with Thermocouples, Thermistors and RTD Sensors,” p. 28.
- [77] “NTC Thermistors, Application Notes,” p. 16.
- [78] Dust, T., and Yarlagadda, A., “PSoC® 3, PSoC 4, and PSoC 5LP - Temperature Measurement with a Thermistor,” (001), p. 19.
- [79] “NTC Thermistors for Temperature Measurement Glass-Encapsulated Sensors, Standard Type,” *Temp. Meas.*, p. 60.
- [80] Steinhart, J. S., and Hart, S. R., 1968, “Calibration Curves for Thermistors,” *Deep Sea Res. Oceanogr. Abstr.*, **15**(4), pp. 497–503.
- [81] “Vishay - Manufacturer of Discrete Semiconductors and Passive Components”, <https://www.vishay.com/>
- [82] “Home | Murata Manufacturing Co., Ltd.”, <https://www.murata.com/>.
- [83] MarlinFirmware, “Home,” Marlin Firmware, <http://marlinfw.org/>.
- [84] “Arduino Reference”
<https://www.arduino.cc/reference/en/language/variables/data-types/double/>.
- [85] “Arduino Reference”
<https://www.arduino.cc/reference/en/language/variables/data-types/float/>.
- [86] Lavenuta, G., “An Explanation of the Beta and Steinhart-Hart Equations For Resistance vs Temperature Relationship in NTC Thermistor Materials,” p. 9.
- [87] Beckwith, T. G., and Buck, N. L., 1969, *Mechanical Measurements [by] T.G. Beckwith [and] N. Lewis Buck*.
- [88] “Practical Temperature Measurements*,” p. 17.
- [89] Duff, M., and Towey, J., 2010, “Two Ways to Measure Temperature Using Thermocouples Feature Simplicity, Accuracy, and Flexibility,” p. 6.
- [90] Dorato, P., 2007, “Introduction to Feedback Control (Morris, K.; 2001) [Book Review],” *IEEE Control Syst.*, **27**(1), pp. 75–77.
- [91] Hagglund, T., 1995, *PID Controllers: Theory, Design, and Tuning*, ISA: The Instrumentation, Systems, and Automation Society, Research Triangle Park, N.C.

- [92] “Improving the Beginner’s PID – Introduction, Project Blog.”
- [93] Sun, J., 2012, “Pulse-Width Modulation,” *Dynamics and Control of Switched Electronic Systems*, F. Vasca, and L. Iannelli, eds., Springer London, London, pp. 25–61.
- [94] “Arduino - PWM”, <https://www.arduino.cc/en/Tutorial/PWM>.
- [95] Chapra, S. C., 2005, *Applied Numerical Methods: With MATLAB for Engineers and Scientists*, McGraw-Hill.
- [96] . M. Giron-Sierra. “Digital Signal Processing with Matlab Examples,” Vol. 1. Springer, 2017
- [97] Staff, C. C., 2016, “Analog Filter Essentials,” Circuit Cellar.
- [98] Coats, A. W., and Redfern, J. P., 1963, “Thermogravimetric Analysis. A Review,” *The Analyst*, **88**(1053), p. 906.
- [99] “Polymers,” NETZSCH Anal. Test, <https://www.netzsch-thermal-analysis.com/us/materials-applications/polymers/>.
- [100] Barton, J. M., 1985, “The Application of Differential Scanning Calorimetry (DSC) to the Study of Epoxy Resin Curing Reactions,” *Epoxy Resins and Composites I*, Springer, Berlin, Heidelberg, pp. 111–154.
- [101] Price, D. M., and Jarratt, M., 2002, “Thermal Conductivity of PTFE and PTFE Composites,” *Thermochim. Acta*, **392–393**, pp. 231–236.
- [102] McDonald, J., “Thermal Conductivities of Metals,” p. 1.
- [103] “3DXTech™ ABS Products - 3DXTech”, <https://www.3dxtech.com/brands/3DXTech%E2%84%A2-ABS.html>.
- [104] “TripTech 3D Printing Filament Products | TripTech Plastics.”
- [105] Raha, S., Williams, M. J., and Lamb, P., 1968, “Cone and Plate Rheometer for Polymer Melts,” *J. Phys. [E]*, **1**(11), p. 1113.
- [106] Bafna, S. S., “The Precision of Dynamic Oscillatory Measurements,” *Polym. Eng. Sci.*, **36**(1), pp. 90–97.
- [107] “3D Printing Temperatures & Printing Guidelines,” Filaments.ca , <https://filaments.ca/pages/temperature-guide>.

- [108] McIlroy, C., and Olmsted, P. D., 2017, “Deformation of an Amorphous Polymer during the Fused-Filament-Fabrication Method for Additive Manufacturing,” *J. Rheol.*, **61**(2), pp. 379–397.
- [109] Nicolae, C.-A., Grigorescu, M. A., and Gabor, R. A., 2008, “An Investigation of Thermal Degradation of Poly(Lactic Acid),” p. 4.
- [110] Jensen, W. B., 2003, “The Universal Gas Constant R,” *J. Chem. Educ.*, **80**(7), p. 731.
- [111] Yih-Shing, D., Ho, T.-C., Chen, J.-R., and Chen-Shan, K., 2010, “Study on Exothermic Oxidation of Acrylonitrile-Butadiene-Styrene (ABS) Resin Powder with Application to ABS Processing Safety,” *Polymers*, **2**.
- [112] Hopmann, C., and Michaeli, W., 2016, *Extrusion Dies for Plastics and Rubber: Design and Engineering Computations*, Carl Hanser Verlag GmbH & Co. KG, Munich ; Cincinnati.
- [113] Marquardt, D., 1963, “An Algorithm for Least-Squares Estimation of Nonlinear Parameters,” *J. Soc. Ind. Appl. Math.*, **11**(2), pp. 431–441.
- [114] Han, C. D., 2007, *Rheology and Processing of Polymeric Materials: Volume 1: Polymer Rheology*, Oxford University Press, USA.
- [115] “3D Printing Temperatures & Printing Guidelines,” Filaments.ca , <https://filaments.ca/pages/temperature-guide>.
- [116] Motel, A. T., “RHEOLOGICAL BEHAVIOR AND FIBER ORIENTATION IN SIMPLE FLOWS OF GLASS FIBER FILLED POLYPROPYLENE MELTS,” p. 486.
- [117] H.M. Laun, “Orientation effects and rheology of short glass fiber-reinforced thermoplastics,” *Coll. Polym. Sci.*, 262 (1984), pp. 257-269
- [118] A. Saadat, H. Nazockdast, F. Sepehr, M. Mehranpour, “Linear and nonlinear melt rheology and extrudate swell of acrylonitrile-butadiene-styrene and organoclay-filled acrylonitrile-butadiene- styrene nanocomposite,” *Polym Eng Sci*, 50 (2010), pp. 2340-2349
- [119] Saadat A, Nazockdast H, Sepehr F, Mehranpoor M: Viscoelastic modeling of extrudate swell of Acrylonitrile-Butadiene-Styrene/Clay nanocomposite, *Appl. Rheol.* 23 (2013) 12131
- [120] Dorgan, J. R., Lehermeier, H., and Mang, M., 2000, “Thermal and Rheological Properties of Commercial-Grade Poly(Lactic Acid)S,” *J. Polym. Environ.*, **8**(1), pp. 1–9.